NOTICE

The quality of this microform is heavily dependent upon the quality of the original thesis submitted for microfilming. Every effort has been made to ensure the highest quality of reproduction possible.

If pages are missing, contact the university which granted the degree.

Some pages may have indistinct print especially if the original pages were typed with a poor typewriter ribbon or if the university sent us an inferior photocopy.

Reproduction in full or in part of this microform is governed by the Canadian Copyright Act, R.S.C. 1970, c. C-30, and subsequent amendments.

AVIS

La qualité de cette microforme dépend grandement de la qualité de la thèse soumise au microfilmage. Nous avons tout fait pour assurer une qualité supérieure de reproduction.

S'il manque des pages, veuillez communiquer avec l'université qui a conféré le grade.

La qualité d'impression de certaines pages peut laisser à désirer, surtout si les pages originales ont été dactylographiées à l'aide d'un ruban usé ou si l'université nous a fait parvenir une photocopie de qualité inférieure.

La reproduction, même partielle, de cette microforme est soumise à la Loi canadienne sur le droit d'auteur, SRC 1970, c. C-30, et ses amendements subséquents.

Canada

ZEEMAN SPECTROSCOPY OF AN AXIAL DOUBLE ACCEPTOR BOUND EXCITON IN MOLECULAR BEAM EPITAXIAL GaAs

by

André Villemaire

B.Sc., Université de Montréal, 1987

THESIS SUBMITTED IN PARTIAL FULFILLMENT OF

THE REQUIREMENTS FOR THE DEGREE OF

DOCTOR OF PHILOSOPHY

in the Department

of

PHYSICS

SIMON FRASER UNIVERSITY

October 1991

ISBN 0-315-78211-0

APPROVAL

Name: André Villemaire

Degree: Ph.D. (Physics)

Title of Thesis: Zeeman Spectroscopy of an Axial Double Acceptor Bound Exciton in Molecular Beam Epitaxial GaAs

Examining Committee: Chairman: Dr. E.D. Crozier

Dr. M.L.W. Thewalt
Senior Supervisor

Dr. R.F. Frindt

Dr. M. Plischke

Dr. K.E. Rieckhoff

Dr. G.E. Stillman
External Examiner
University of Illinois at Urbana-Champaign
Urbana, Illinois

Date Approved: October 4 91

PARTIAL COPYRIGHT LICENSE

I hereby grant to Simon Fraser University the right to lend my thesis, project or extended essay (the title of which is shown below) to users of the Simon Fraser University Library, and to make partial or single copies only for such users or in response to a request from the library of any other university, or other educational institution, on its own behalf or for one of its users. I further agree that permission for multiple copying of this work for scholarly purposes may be granted by me or the Dean of Graduate Studies. It is understood that copying or publication of this work for financial gain shall not be allowed without my written permission.

Title of Thesis/Project/Extended Essay

Zeeman Spectroscopy of an axial Double Acceptor Bound Exciton in Molecular Beam epitaxial GaAs

Author:

(Signature)

ANDRÉ VILLEMAIRE

(Name)

October 9 91

(Date)

ABSTRACT

Molecular beam epitaxy is one of the primary techniques used for the growth of state-of-the-art gallium arsenide epilayers. The sharpness of the shallow donor and acceptor bound exciton recombination photoluminescence lines in such samples is indicative of low impurity content and good morphology. However, a number of extra photoluminescence lines are frequently observed in samples grown by this technique. These lines have been associated with defects induced by growth conditions.

In this work, we have investigated the photoluminescence signature of such a growth induced defect, the Y defect. A Fourier transform interferometer was used for polarization, resonant and Zeeman spectroscopy, while time-resolved photoluminescence was performed with the aid of a conventional dispersive spectrometer. The interferometric apparatus offered the necessary resolution and signal throughput capabilities for the detailed measurements reported here.

The Y defect is demonstrated to be an axial double acceptor aligned along the [110] direction in the GaAs lattice, perpendicular to the (001) growth direction. Selective excitation photoluminescence spectra reveal two-hole replicas consistent with the presence of 2 holes in the bare neutral acceptor complex. From the two-hole spectrum, the ionization energy from the neutral to the singly ionized state is determined to be almost equal to the effective mass value for single acceptors.

ACKNOWLEDGEMENTS

I would like to thank my supervisor, Dr. Mike Thewalt for his invaluable guidance and his close support throughout this work. Special thanks to all the members of the group for sharing their knowledge and experimental skills and for creating an exciting and enjoyable work environment.

I would like to express my gratitude to G.E. Stillman for supplying the crucial sample A. I also wish to thank G. Kirczenow for invaluable discussions on the analysis presented in this thesis.

Support from the Natural Science and Engineering Research Council of Canada and Simon Fraser University is gratefully acknowledged.

This work was brought to you by the letter Y and by the numbers 0, 1, 2, 3 and 4.

TABLE OF CONTENTS

TABLE OF CONTENTS (CONTINUED)

LIST OF TABLES

LIST OF FIGURES

LIST OF FIGURES (CONTINUED)

LIST OF ABBREVIATIONS

APD	Avalanche Photo-Diode
BE	Bound Exciton
CW	Continuous Wave
DAP	Donor-Acceptor Pair
DS	Dispersive Spectroscopy
EM	Effective Mass
EMA	Effective Mass Approximation
FE	Free Exciton
FM	Fold Mirror
FT	Fourier Transform
FTS	Fourier Transform Spectroscopy
FWHM	Full Width at Half Maximum
GID	Growth Induced Defect
HR	High Reflector
LEC	Liquid Encapsulated Czochralski
LPE	Liquid Phase Epitaxy
MBE	Molecular Beam Epitaxy
MOCVD	Metal Organic Chemical Vapor Deposition
OC	Output Coupler
PL	Photoluminescence
PLE	Photoluminescence Excitation
PMT	Photomultiplier Tube
RHEED	Reflection High Energy Electron Diffraction
SI	Semi-Insulating
UHV	Ultra High Vacuum
VPE	Vapor Phase Epitaxy
X	Free Exciton
(A^0, X)	Neutral Acceptor Bound Exciton
(D^0, A^0)	Donor-Acceptor Pair
(D^0, X)	Neutral Donor Bound Exciton
(D^+, X)	Ionized Donor Bound Exciton
(e, A^0)	Free Electron to Bound Hole
(e,h)	Free Electron to Free Hole

CHAPTER 1

INTRODUCTION

1.1 Defects in molecular beam epitaxial GaAs

The study of defects in semiconductors has occupied researchers since the birth of semiconductor science. This is not surprising if one considers that the most important and useful property of semiconductors is the ability to make substantial changes in the electrical conductivity and in other physical processes by the addition of impurities.

In a broad sense, the term defect refers to any deviation from the pure, perfectly ordered crystal. This can be manifested in a wide variety of ways. An *impurity* is a type of compositional defect where a foreign atom replaces a host atom (*substitutional*) or is incorporated between lattice sites (*interstitial*). These imperfections, along with other simple defects such as missing atoms (*vacancies*), are known as *point defects*. Except for interstitials, point defects preserve the full rotational symmetry of the zincblende crystal structure, like that of GaAs. More extended defects range from *complexes*, formed by the association of a few point defects to macroscopic *structural* defects such as dislocations and grain boundaries. In the case of complexes, some or most of the original symmetry is lost because of the spatial extent of the defect.

Complexes and structural defects are more prevalent in *bulk-grown*

crystals because of mechanical stresses caused by uneven cooling and the complex kinetics of crystallization. Other growth techniques developed more recently, labelled *epitaxial* (from the Greek epi-*upon* and taxis-*arrangement*), enable the fabrication of structurally nearly-perfect crystal layers with low concentrations of impurities. These techniques are characterized by controlled and progressive layer-by-layer growth onto a chosen substrate in such a way as to preserve the substrate crystalline order.

At the present, the favored bulk growth technique for GaAs is the Liquid Encapsulated Czochralski (LEC) method. In this technique, a cylindrical single crystal called a *boule*, typically 7.5 or 10 cm in diameter, is pulled from a near-stochiometric melt of gallium and arsenic that is encapsulated by a layer of non-reacting boric oxide to prevent arsenic evaporation. Considering the large number of wafers that can be cut from a boule grown in a few hours, the LEC method is much more economical than epitaxial methods where growth is typically performed on a small area and at rates of micrometers per minute.

The inherent advantage of epitaxial growth techniques over bulk growth methods is the ability to change the composition or doping of the grown structure within a few atomic distances while depositing the highest quality material. In the case of bulk grown material, circuits are fabricated by performing separate post-growth processing treatments such as impurity diffusion or ion implantation. These treatments need to be performed in a highly controlled manner and require extra wafer preparation steps. Although epitaxial methods use more sophisticated apparatus, they have the advantage of being able to achieve very

complicated heterostructures in one growth run.

Since the realization of two-dimensional electron gases at GaAs/$Al_xGa_{1-x}As$ interfaces [79T], epitaxial growth techniques have made possible the fabrication of exotic heterostructures such as quantum wires [82Da], quantum dots [90L], multidimensional superlattices [85C] as well as others [85C]. Such achievements suggest the possibility of exciting new semiconductor devices. These advances are welcomed, especially if we consider that the overwhelming majority of devices fabricated today are still based on the PN junction, which was discovered 40 years ago.

Three basic classes of epitaxial methods are used [87Sa] for the fabrication of GaAs crystals: *Liquid Phase Epitaxy* (LPE), *Vapor Phase Epitaxy* (VPE) and *Molecular Beam Epitaxy* (MBE). We will restrict our attention to the last two methods, as they achieve the best quality growth. MBE differs from VPE in that *elemental* species instead of *chemical compounds* are used for source material. In classic VPE, known as the chloride transport technique, $AsCl_3$ vapors react with metallic gallium to form a GaAs epilayer on a GaAs substrate. A relatively new version of VPE, *Metal Organic Chemical Vapor Deposition* (MOCVD), is now replacing the chloride transport technique because of its simplicity, ease of control and other advantages [87Sa]. In a typical MOCVD reactor, a gallium metal-organic compound (trimethylgallium or triethylgallium) reacts with arsine (AsH_3) to form GaAs. In contrast, MBE is a sophisticated co-evaporation technique of elemental Ga and As performed in Ultra High Vacuum (UHV).

Very high purity GaAs layers with impurity concentrations less than

10^{14} cm^{-3} have been achieved by both MOCVD and MBE. A common benefit of these techniques is the observed smoothing of the surface of the epilayer during growth. Structural defects present in the substrate are prevented from being transferred to the epilayer by growing a buffer layer and atomically flat layers can be achieved. Both MBE and MOCVD are actively being used in current research efforts. MOCVD is somewhat simpler and less expensive than MBE. On the other hand, more abrupt interfaces can be grown with MBE. Moreover, working in a UHV environment enables the use of *in-situ* monitoring devices. A Reflection High Energy Electron Diffraction (RHEED) set-up, an Auger spectrometer, a mass spectrometer and ion gauges are usually incorporated [85D] in the MBE reactor to monitor and control the molecular and atomic beams as well as the epitaxial layers. Having briefly contrasted a few of the epitaxial growth methods currently used to fabricate GaAs crystals, we will now center our attention on MBE, the method used to grow most of the samples studied in this work.

The structural quality of the current state-of-the-art epilayer grown by MBE is very close to perfection. Point defects and small complexes are nevertheless always present to some extent. Undoped MBE-grown GaAs layers are usually p-type, mainly because of the presence of carbon incorporated as an acceptor, C_{As} (carbon on an arsenic lattice site). The carbon originates from residual UHV gases such as CO_2, CO and CH_4. Other contaminants present in the Ga and As sources can also increase the epilayer impurity concentration. Once identified, these types of unintentional impurities can usually be eliminated by performing adequate purifying processes on the source materials.

Contamination attributed to other parts of the reactor, for instance an effusion cell, can also be remedied by suitable choices of replacement for these parts. *Growth Induced Defects* (GID), on the other hand, are considerably more difficult to control. While they may depend on the presence of certain contaminants, their formation is principally controlled by the growth conditions.

In MBE GaAs, the most intensely studied GID are the so-called KP-lines, named after their discoverers, Künzel and Ploog [80K]. In their studies, they used photoluminescence (PL), an impurity-specific characterization technique that will be described in detail later in this work. By noting that the KP-related PL lines disappeared when As_2 molecules were used instead of As_4 as the As source, they attributed the observed lines to GID. After sustained research for the past 10 years, the KP-related PL signatures have been attributed to bound excitons on axial double acceptors, but the chemical identity of these acceptors is still unknown [88S,90C].

In fact, compared to point defects, very little is known about complexes in semiconductors. Current models give a satisfactory account only for substitutional impurities that lead to simple levels in the band gap. Also, PL features induced by simple substitutional impurities can generally be correlated to a specific contaminant by experiments where the doping level is intentionally varied. During the formation of GID however, several parameters are varied simultaneously and uncontrollably, and very incomplete conclusions are reached even from careful studies.

Another GID that illustrates our poor understanding of complexes is

EL2, the double donor level lying at the middle of the gap which is responsible for the semi-insulating properties of LEC grown GaAs crystals [88B,88K]. The vast amount of research done on this technologically important defect in the past decade has not succeeded in conclusively determining its exact chemical nature. The debate is now focused on two models, one suggesting it is the simple arsenic antisite As_{Ga} (an arsenic atom substituted on a gallium site), the other claiming the presence of an additional arsenic interstitial (As_i). This persistent uncertainty underlines the problems encountered during the investigation of defects more complicated than simple substitutionals. The study of such defects is complicated by the great variety of possible defect configurations (especially in a compound semiconductor like GaAs) and the interactions between them. Despite these difficulties, the growing importance of compound semiconductor devices underscores the necessity to investigate and identify defects, particularly in light of their often strong effects on device performance [73M].

In this work, we have investigated a GID, hereafter referred to as the Y defect following Skolnick *et al.* [85Sa], by means of its PL signature. This defect is found in undoped MBE GaAs layers grown under high As/Ga flux ratios. Similar samples grown with lower source flux ratios were found to be free of this defect, clearly placing it in the growth induced defect category. In order to interpret the results from our detailed spectroscopic investigations, we will now introduce topics pertaining to electronic impurity levels. We will also review the properties of excitons as well as their interaction with light.

1.2 Electronic states and impurity levels in semiconductors

The problem of modeling the behavior of the electrons in a semiconductor is a difficult one. It is after all, a many-body problem of a formidable assembly ($\sim 10^{24}$ per cm^3) of interacting objects whose de Broglie wavelength is comparable to that of the lattice potential. This last feature makes a quantum mechanical treatment of the problem necessary. Despite all these complications, impressive results can be obtained by exploiting the simple periodicity and symmetry properties of the crystal structure, those embodied in the *Bravais lattice.*

The proper Hamiltonian for the system should contain potential terms not only describing electron-nuclei interaction but also electron-electron interactions. A common simplification is to find an effective one-electron potential $U(\mathbf{r})$ representing both types of interactions. While finding an appropriate form for this effective potential is an important problem, useful information can be obtained using the periodicity properties of the lattice alone. This is encompassed in Bloch's theorem. It states that the eigenstate Ψ of the one-electron (of mass m_e^*) Hamiltonian

$$H = -\frac{\hbar^2\nabla^2}{2m_e^*} + U(\mathbf{r}) \qquad (1.1),$$

where $U(\mathbf{r}) = U(\mathbf{r}+\mathbf{R})$ for all vectors $\mathbf{R}$ joining the origin to an atom in

the Bravais lattice, can be chosen to have the form of a plane wave modulated by a function with the periodicity of the Bravais lattice:

$$\Psi_{nk}(r) = u_{nk}(r)\, e^{ik\cdot r} \qquad (1.2),$$

where $u_{nk}(r+R) = u_{nk}(r)$ for all **R** of the Bravais lattice. The so-called band index n is necessary because there are many independent eigenstates for a given wavevector **k**. This can be seen in Fig. 1.1. Fig. 1.1 schematically illustrates the energy dispersion curve of a pure GaAs crystal for small electron wavevector along two crystallographic directions, [111] and [100]. At **k**=0, many energies are possible, those at the band edges are labelled Γ_6 and Γ_8.

GaAs is a direct gap semiconductor, that is both the conduction and the valence band edges are located at **k**=0. The processes studied in this work involve thermalized carriers, i.e. electrons and holes that have reached their respective band edges. It will therefore be sufficient to center our attention around the center of the Brillouin zone as shown in Fig. 1.1. In particular, the curvature radii at Γ_6 and Γ_8 are taken as the effective electron and hole masses for states relatively close to the band extrema.

The valence band as depicted in Fig. 1.1, represents the states forming the bonds between adjacent As and Ga atoms. Each atom in the lattice, be it As or Ga, is sharing electrons with its four tetragonally coordinated Ga or As neighbors in the form of four sp^3 hybridized bonds, as in the CH_4 molecule. Strong spin-orbit interaction lifts the six fold degeneracy of these states. This results in two levels, one J=3/2

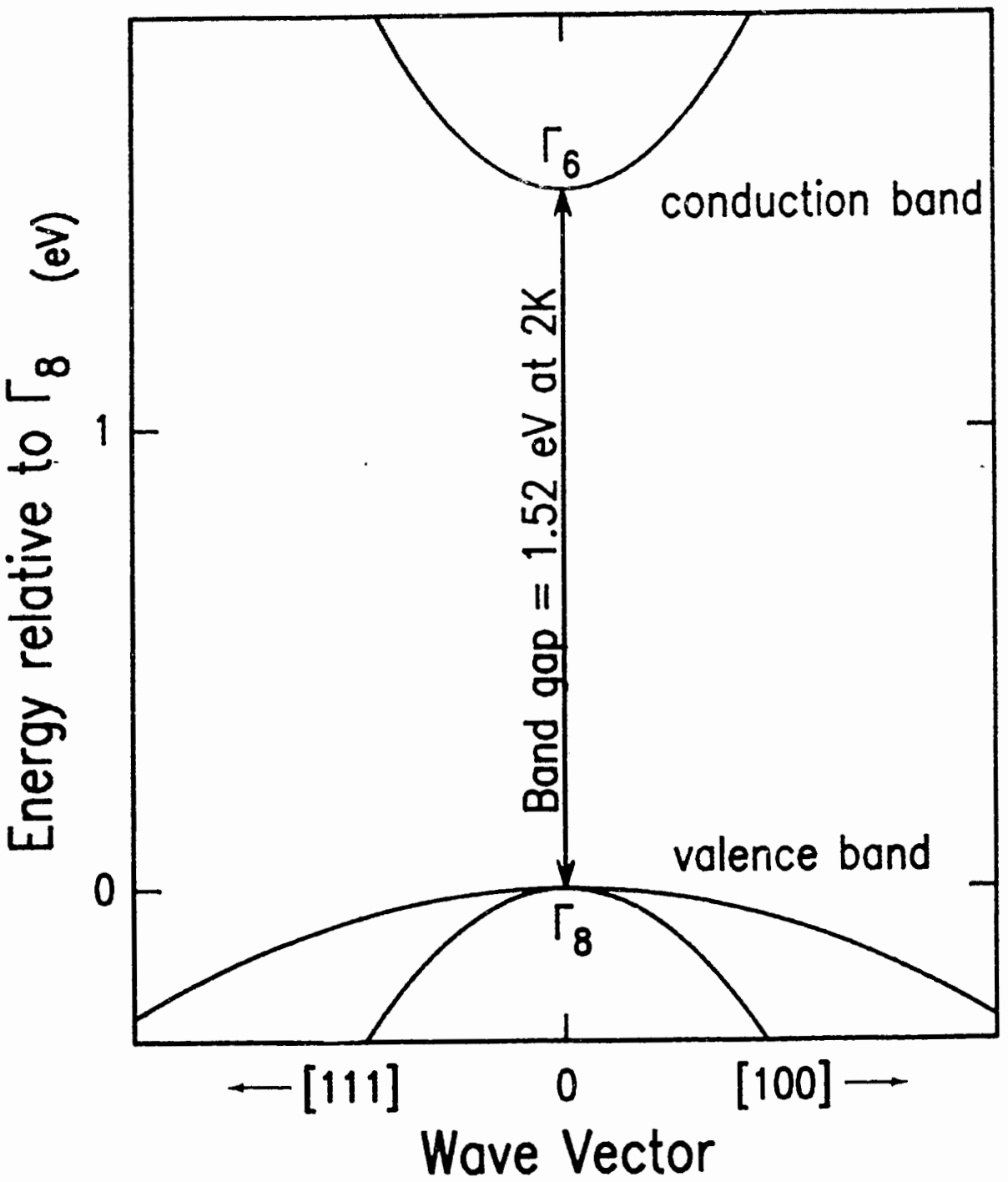

Figure 1.1

Detail of a schematic energy dispersion diagram in GaAs for small **k** vectors. Only energies close to the band-gap region are shown. The anisotropy of the valence band has been neglected. The two-fold minimum of the conduction band is labelled Γ_6 while the four-fold valence band maximum is labelled Γ_8.

fourfold degenerate level labelled Γ_8 in Fig. 1 and another J=1/2 twofold degenerate labelled Γ_7. This last one is also known as the split-off band and is found at lower energies than Γ_8 (not visible in Fig. 1.1). The conduction band is, on the other hand, formed of overlapping 5s (l=0) orbitals and therefore preserves a spin-like J=1/2 character. The two-fold degenerate conduction band edge at k=0 is labelled Γ_6. Free electrons and holes which have thermalized to the conduction and valence band edges therefore occupy the Γ_6 and Γ_8 levels, respectively.

The labels Γ_6, Γ_7 and Γ_8 are derived from group theory, a topic that needs to be discussed briefly. Technically speaking, Γ_6, Γ_7 and Γ_8 are three *representations* of T_d. T_d is the point group of GaAs, i.e. the group of all the rotations which leaves the GaAs crystal invariant. If a GaAs crystal is deformed, some symmetries are lost and the point group of the perturbed crystal is reduced to a subset of T_d. For the purposes of semiconductor physics, a representation is usually considered as a set of unitary matrices, one for each element of the point group, which acts on a particular set of degenerate eigenfunctions. The representation Γ_8 for example, acts on the subspace spanned by the four degenerate J=3/2 states from the valence band edge. A particular Γ_8 matrix associated with a symmetry rotation describes how these degenerate states transform into each other under the application of such a operation. Group theory analysis is useful for this work since it allows predictions of number and degeneracy of states based on simple considerations. In particular, it is possible to predict the number of levels obtained from the coupling of particles as well as the

splitting of levels caused by a of reduction of symmetry. Group theory cannot, however, predict level ordering nor can it evaluate magnitude of splitting. The use of group theory will be illustrated in subsequent chapters.

At zero Kelvin, the valence band of a pure semiconductor is completely filled and its conduction band is completely empty. Consider the excitation of an electron from the top of the valence band (highest energy occupied state) to the bottom of conduction band (lowest energy unoccupied state). This transition, called *band-to-band,* requires a quantum of energy equal to the energy of the gap. The excited electron wavefunction is described by equation 1.2 and is therefore completely delocalized; a plane wave exhibits an equal probability amplitude throughout space. The empty state left behind in the valence band, described as a hole, has a valence band wavefunction also of the form of equation 1.2 and is thus completely delocalized as well. The free electron and hole can however lower their energy by interacting via the the Coulomb potential to form a free exciton (FE). The attractive potential has the form

$$U^C(r) = - \frac{e^2}{4\pi\varepsilon r} \qquad (1.3),$$

where $\varepsilon = \varepsilon_r \varepsilon_0$, ε_0 is the permittivity of vacuum and ε_r=12.49 [90Sa] is the dielectric constant of GaAs. For this potential to be defined the electronic particles (electron and hole) need to be somewhat localized. This can be achieved by considering the electron and hole wavefunctions

as linear combinations of eigenfunctions taken from their respective bands :

$$\psi_e(r_e) = \sum_k A_k \, u_{ck}(r_e) \, e^{ik\cdot r_e} \qquad (1.4a),$$

$$\psi_h(r_h) = \sum_l B_l \, u_{vl}(r_e) \, e^{il\cdot r_h} \qquad (1.4b),$$

where A_k (B_l) are the expansion coefficients of the Fourier sum leading to an electron (hole) wavepacket. Granted that the particles are not too localized, the sum can be restricted to a range of **k** values close to the band extrema. In this case, we can assume that the periodic functions $u_{nk}(r)$ do not vary appreciably over the sums and can be factored out. The approximate wavefunctions can then be written as

$$\psi_e(r_e) \cong u_{ck_0}(r_e) \sum_k A_k \, e^{ik\cdot r_e} \qquad (1.5a),$$

$$\psi_h(r_h) \cong u_{vl_0}(r_e) \sum_l B_l \, e^{il\cdot r_h} \qquad (1.5b),$$

where k_0 and l_0 are the band extrema wavevectors. In GaAs $k_0=l_0=0$ and the functions $u_{ck_0}(r_e)$ and $u_{vl_0}(r_h)$ correspond to those at Γ_6 and Γ_8, respectively. The wavefunctions can therefore be visualized as having the symmetry of the respective band edges but being modulated in space by an envelop function. For an exciton, the distance r in equation 1.3 is then the separation of the center of these envelop functions.

The electron and the hole in the exciton form a system analogous to the hydrogen atom. By considering i) the host lattice as a uniform background of dielectric constant ε and ii) the electron and the hole as point charges of mass m_e^* (effective mass of an electron at Γ_6) and m_h^* (effective mass of a hole at Γ_8) respectively it becomes a simple matter to solve the problem exactly. As for the case of hydrogen, the problem separates into two parts, 1) the free motion of the exciton as if it were a free particle of mass $M = m_e^* + m_h^*$ located at its center of mass and 2) the relative motion of the electron and hole considered as the orbiting motion of an independent particle of reduced mass $\mu = ((m_e^*)^{-1}+(m_h^*)^{-1})^{-1}$ in a Coulomb field. The wavefunction of the free exciton satisfies a Hamiltonian of the form:

$$H_{FE} = H_M + H_\mu \qquad (1.6).$$

$$\text{where } H_M = \frac{P^2}{2M} \quad \text{and} \quad H_\mu = \frac{p^2}{2\mu} - \frac{e^2}{\varepsilon r}$$

In complete analogy with hydrogenic systems, the solution for H_μ can be written as

$$E_{FE}^n = -\frac{e^4 \mu}{2\hbar^2 \varepsilon^2 n^2} \qquad (\text{for } n = 1,2,3\ldots) \qquad (1.7).$$

The ionization energy (n = 1 in 1.7) of the excitonic system is about 4 meV in GaAs. At temperatures lower than ~4 meV/k (~50K), where k is the Boltzmann constant, the free electron and hole will therefore

spontaneously form excitons. These excitons are free to move as a whole provided that the translational group velocity of the electron and of the hole are identical.

In crystals containing impurities or defects, there exist other mechanisms whereby electronic wavefunctions are localized. One of the simplest examples is the well known donor or acceptor impurity levels which are usually found lying somewhere in the energy gap. Consider the case of an isolated Ge impurity atom replacing a Ga atom in an otherwise perfect crystal. A germanium atom has one extra electron as well as one extra proton as compared to a gallium atom. All valence states being occupied, the extra electron will occupy a bound state around the positively charged Ge ion core rather than a state from the conduction band. The bound state is more energetically favorable than a free state by an amount roughly equal to the Coulomb energy. To be precise, the singly ionized impurity potential can be written as

$$U(\mathbf{r}) = -\frac{e^2}{4\pi\varepsilon r} + V_c(\mathbf{r}) \qquad (1.8),$$

where $V_c(\mathbf{r})$, the *Central Cell Potential*, represents the species-dependent correction to the Coulomb interaction. The central cell potential includes the effects which arise from differences in the impurity and the host core potentials as well as effects from associated strain fields and charge redistributions. The divergence of $U(\mathbf{r})$ from the simple Coulombic form is largest close to the impurity core since $V_c(\mathbf{r})$ is a rapidly decreasing function of $|\mathbf{r}|$. The first approximation to equation 1.8, the *Effective Mass Approximation* (EMA) [55K], consists

in taking $V_c(\mathbf{r})$ equal to zero.

In GaAs the electron effective mass exhibits a nearly isotropic and nearly parabolic dependence upon $\mathbf{k}$. Thus for an electron bound to a donor, EMA results in a simple hydrogenic energy spectrum

$$E^n_{Donor} = - \frac{e^4 m^*_e}{2\hbar^2 \varepsilon^2 n^2} \qquad (\text{for } n = 1,2,3\ldots) \qquad (1.9),$$

as for the case of the excitonic system, with a Bohr radius of

$$a_{Donor} = - \frac{\hbar^2}{2m^*_e E^{n=1}_{Donor}} \qquad (1.10),$$

where m^*_e=0.0665 m_0 [69Sa] and m_0 is the electron rest mass.

The EMA yields exceedingly good ionization energies for substitutional donors in GaAs [71Sa]. For example, the ground state-to-ionization EM energy is 5.715 meV [71Sa] as compared to experimental values of 5.752 to 5.913 meV [89S]. Substitutional donor wavefunctions are all very extended ($a_{Donor} \cong$ 100 Å or about 18 lattice spacings) owing to the small electron effective mass in GaAs. It is therefore not surprising to observe a high insensitivity to the chemical nature of the attractive core since the electron overlap with it is so small.

For acceptors, EMA calculations are complicated by the anisotropy and the degeneracy of the valence band. Various methods to account for these features have been developed, and accurate acceptor EMA ionization

energy and excited state energies have been reported [73B, 78L, 90Sa]. Because of their relatively large effective masses, the measured ionization energies of the substitutional acceptors are appreciably larger than those of donors. For reasons mentioned before, strong localization leads to some spread in the observed acceptor ionization energies. For shallow acceptors in GaAs, EMA gives an ionization energy of 26.0 meV [90Sa], while ionization energies for C, Zn, Si and Ge acceptors were measured to be 26.0, 30.7, 34.5 and 40.4 meV respectively [83K, 85R]. Characterization of acceptors in GaAs is consequently a much easier task than that of donors since optical assaying methods usually rely on differences in impurity level energies.

Excitons travelling in imperfect crystals can lower their energy by binding onto defects, thus forming bound excitons (BE). This exciton binding energy is usually referred to as *localization energy* E_{loc} to avoid confusion with the total exciton binding energy or with the ionization energy of the impurity. In this thesis we will abide by this terminology. Excitons can, under some circumstances, bind to ionized as well as neutral impurities and impurity complexes. Whereas neutral donors and acceptors should in theory always bind excitons, it was shown [64H] for ionized impurities that stability is only possible for a certain range of effective mass ratios $\sigma = m_e^*/m_h^*$. The critical point of stability for acceptors is the multiplicative inverse of that for donors. In GaAs σ doesn't allow ionized acceptor BE, but allows ionized donor BE [71Sb], a feature that is believed to have been observed [74H].

Binding mechanisms for excitons must obviously be more complicated than the simple Coulomb interaction, since the exciton is neutral. For

neutral impurity BE the analogy with the hydrogen molecule has been made [58L]. Exciton binding can sometimes be qualitatively understood in terms of simple Coulomb and exchange interaction but to get the complete picture, detailed perturbation or variational calculations are necessary. These topics extend beyond the scope of this work - for reviews see references 75B, 81L and 81R.

When an exciton is bound to a center that already contains bound charges, a neutral donor for instance, the concept of the exciton somewhat loses its meaning. Due to the indistinguishability of electronic particles, it is meaningless to differentiate between the charges that were present before the arrival of the exciton and those of the exciton. Instead, it is more proper to visualize the assembly of charges as an electronic complex with its components filling available states in accordance with the Pauli exclusion principle. The levels of such complexes are well defined and can be calculated from the Hamiltonian containing terms for the interactions between bound particles and with the binding center potential. The localization energy therefore remains perfectly well defined, being the difference between the FE recombination energy and the recombination energy of *one hole* and *one electron* from the bound complex. The term *bound exciton* continues to be used in the literature for simplicity and will also be used in this work.

There exists a linear relation, first recognized in Si by Haynes [60H], between the exciton localization energy (E_{loc}) and the impurity ionization energy (E_{ion}), namely

$$E_{loc} = aE_{ion} + b \qquad (1.11).$$

This relation is known as Haynes' rule. Equation 1.11 holds to some extent in various semiconductors, but with a different set of constant a and b in each case [79D]. Relation 1.11 is illustrated in Fig. 3.8 for the case of shallow acceptors in GaAs [73W, 91B], as well as for the KP acceptors [88Ca]. Differences in the shallow donor BE localization energies are too small to be measured under normal conditions, which prevents a similar relation to be tested for shallow donors.

1.3 Photoluminescence processes in semiconductors

Most of our knowledge of FE and BE has been obtained using optical spectroscopic methods. Impurity levels can also be studied by optical means although purely electrical measurements, such as Hall effect [79A] and deep level transient spectroscopy [79J], are also extensively used. Optical spectroscopy is, however, more direct and more informative, being capable of distinguishing between effects due to slightly different centers, which are often masked in electrical methods.

The most common optical methods are absorption and photoluminescence spectroscopy. These two techniques can yield similar information, but being somewhat different in nature they can often complement each other. Absorption measurements monitor the amount of

light absorbed at a given energy during its passage through a sample. The knowledge of the oscillator strength of the process involved allows the calculation of the concentration of absorbing centers. PL spectroscopy, on the other hand, involves the detection of the light emitted following excitation to a non-equilibrium state by absorption of energy in the form of photons.

The study of thin semiconductor layers is usually difficult with absorption spectroscopy since the substrate material used for epitaxial depositions is usually fabricated by bulk growth techniques. The relatively high impurity and defect content of such substrates causes overwhelmingly strong absorption that can mask any absorption signal from the layer under study. This situation is worsened by the fact that the epitaxial layers are typically two to three orders of magnitude thinner than the substrate on which they are grown. It is of course possible to polish or etch away the substrate but such delicate operations were not attempted in this study.

This study made exclusive use of PL measurements. With a suitable choice of excitation wavelength, it is possible to generate PL emission from only a thin surface layer. This makes PL an ideal tool for the investigation of different kinds of layers grown by epitaxial techniques.

PL transitions observed in semiconductors are summarized in Fig. 1.2. In its simplest form, PL spectroscopy is performed by generating free electrons and holes with light of energy greater than the band gap of the semiconductor studied. This process is labelled (e,h) on the left hand side of Fig. 1.2 where intrinsic, or non-impurity

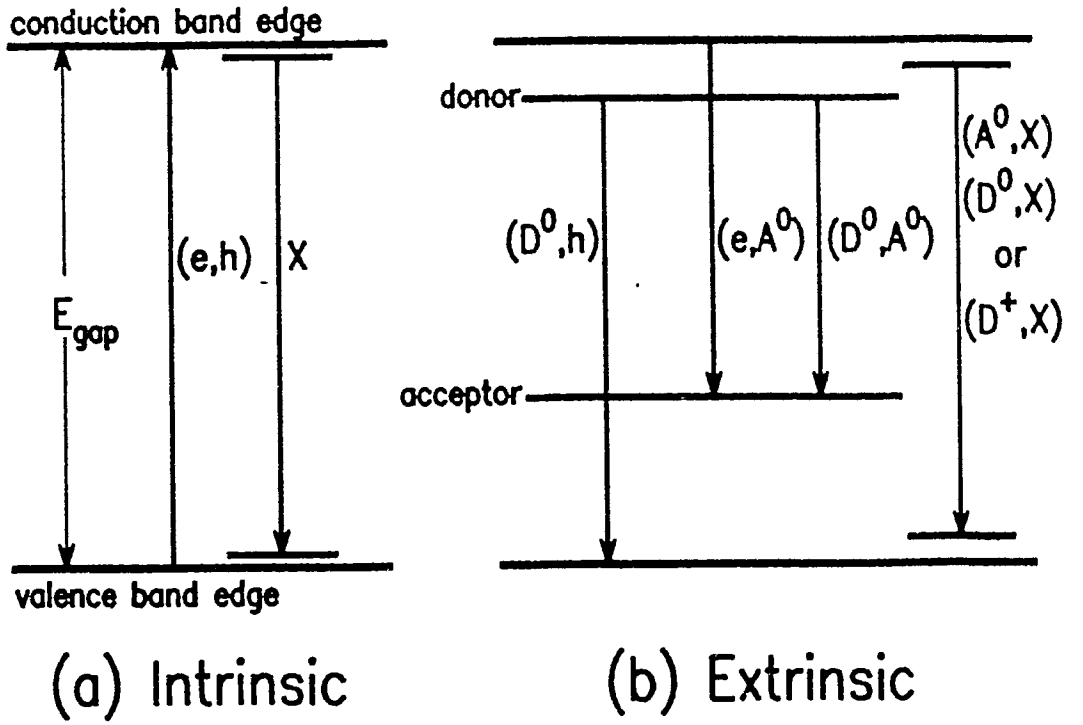

Figure 1.2

Principal transitions in direct-gap semiconductors. For intrinsic materials (a), we show the band-to-band transition (e,h) as an absorption process corresponding to photo-excitation and the free-exciton (or polariton) recombination luminescence transition X. For extrinsic materials (b), we show additionnal impurity-related luminescence transitions. Free-to-bound transitions, (e,A^0) and (D^0,h), involve the recombination of a free particle with one bound to an acceptor or a donor. Donor-acceptor-pair (D^0,A^0) transitions occur when an electron from a neutral donor recombines with a hole from a neutral acceptor. Recombination of excitons bound to impurities is also an important luminescence phenomenon. Excitons can bind to neutral acceptor (A^0,X), neutral donors (D^0,X) as well as ionized donors (D^+,X).

related processes are displayed. These free charges can get trapped at ionized impurities, recombine with free particles of opposite sign or, at sufficiently low temperature, form FE as described earlier. A FE has a finite lifetime and before interacting with anything else can, in principle, decay and transfer its energy to a photon.

FE recombination (X in Fig. 1.2(a)) features are commonly observed in GaAs PL spectra. The lineshape of such processes, however, is different from what would be expected for the signature of a free particle. Because of the necessity to conserve crystal momentum, only electron-hole pairs with very small momentum (equal to the momentum of a photon corresponding to the FE energy) can decay and generate a photon. The observed lineshape does not display the Boltzmann tail characteristic of a gas of free particles. Instead, the FE lineshape normally displays a notched profile [86Sa]. The reason for this arises from an added complication to the FE picture. In direct gap semiconductors, such as GaAs, the FE mode couples very strongly with light of the same wavevector. The resulting mixed state, called a polariton, has been the subject of considerable research [59T, 73H, 75W, 86Sa]. The shape and intensity of the polariton PL is a complicated function of the excitation density, impurity concentration and surface quality [86Sa]. For the purposes of this work it is sufficient to note that the spectral energy of the notch is a suitable approximation for the energy of a FE having zero kinetic energy. At liquid helium temperatures (1.6-4.2 K), these zero kinetic energy FE-polariton recombination photons appear at a spectral energy of

$$h\nu^{FE} = E_{gap} - E_{FE} = 1515.2 \quad meV \qquad (1.12),$$

where E_{gap} = 1519.2 meV is the GaAs band gap [72S] and E^{FE} was given by equation 1.7 with n=1.

The impurity-related PL processes are displayed in Fig. 1.2(b). (A^0,X), (D^0,X) and (D^+,X) denote neutral acceptor, neutral donor and ionized donor bound excitons, respectively. Excitons bound to impurities also have a finite lifetime and will recombine by emitting photons of energy

$$h\nu^{BE} = E_{gap} - E_{FE} - E_{loc} \qquad (1.13),$$

where E_{loc} is the impurity-specific localization energy.

Experimentally, BE recombination lines are very narrow provided that the crystal is pure enough. In LEC-grown GaAs, the (A^0,X), (D^0,X) and (D^+,X) transitions are broadened by the presence of local random perturbations in the form of electric fields from ionized impurities and of strains introduced by various defects. Epitaxially grown GaAs is on the other hand much purer, and very narrow linewidths, believed to be limited by the BE lifetimes, have been reported [90B].

Other impurity-related PL processes are displayed in Fig. 1.2(b). Donor-acceptor pair (DAP) recombination (labelled (D°,A°)) involves both a donor and an acceptor impurity. For pairs of reasonably large separation, an electron bound to a donor recombining with a hole bound

to an acceptor gives rise to radiation of energy given approximately by

$$h\nu^{DAP} = E_{gap} - (E_A + E_D) + \frac{e^2}{\varepsilon r} \qquad (1.14),$$

where E_A and E_D are the acceptor and donor ionization energies and r is the donor-acceptor pair separation [63H]. The Coulomb term ($e^2/\varepsilon r$ in equation 1.14) arises because the donor and acceptor, initially neutral, are left ionized after recombination. This inter-impurity interaction disperses the luminescence corresponding to pairs with different separations, resulting in a broad spectral lineshape. Finally we have the free-to-bound (FB) transitions (labelled (D°,h) and (e,A°) in Fig. 1(b)) in which a free particle recombines with one of opposite charge bound to an impurity. In this case the emission lineshape is broad due the kinetic energy of the free particle involved.

Since inter-particle interactions are poorly represented on the band energy diagram of Fig 1.2, a more appropriate and more detailed excitonic energy diagram is presented in Fig 1.3. To simplify the notation, we focus our attention on a neutral single acceptor as the exciton binding center. The initial states of the illustrated transitions contain one exciton and one hole while the final states contain only one hole. The main BE transitions occur between the ground or excited state(s) of the BE complex and the ground state of the acceptor. Other transitions, whereby the acceptor is left in one of its excited states are also possible. These transitions are called two-hole replicas since both the hole taking part in the recombination and the

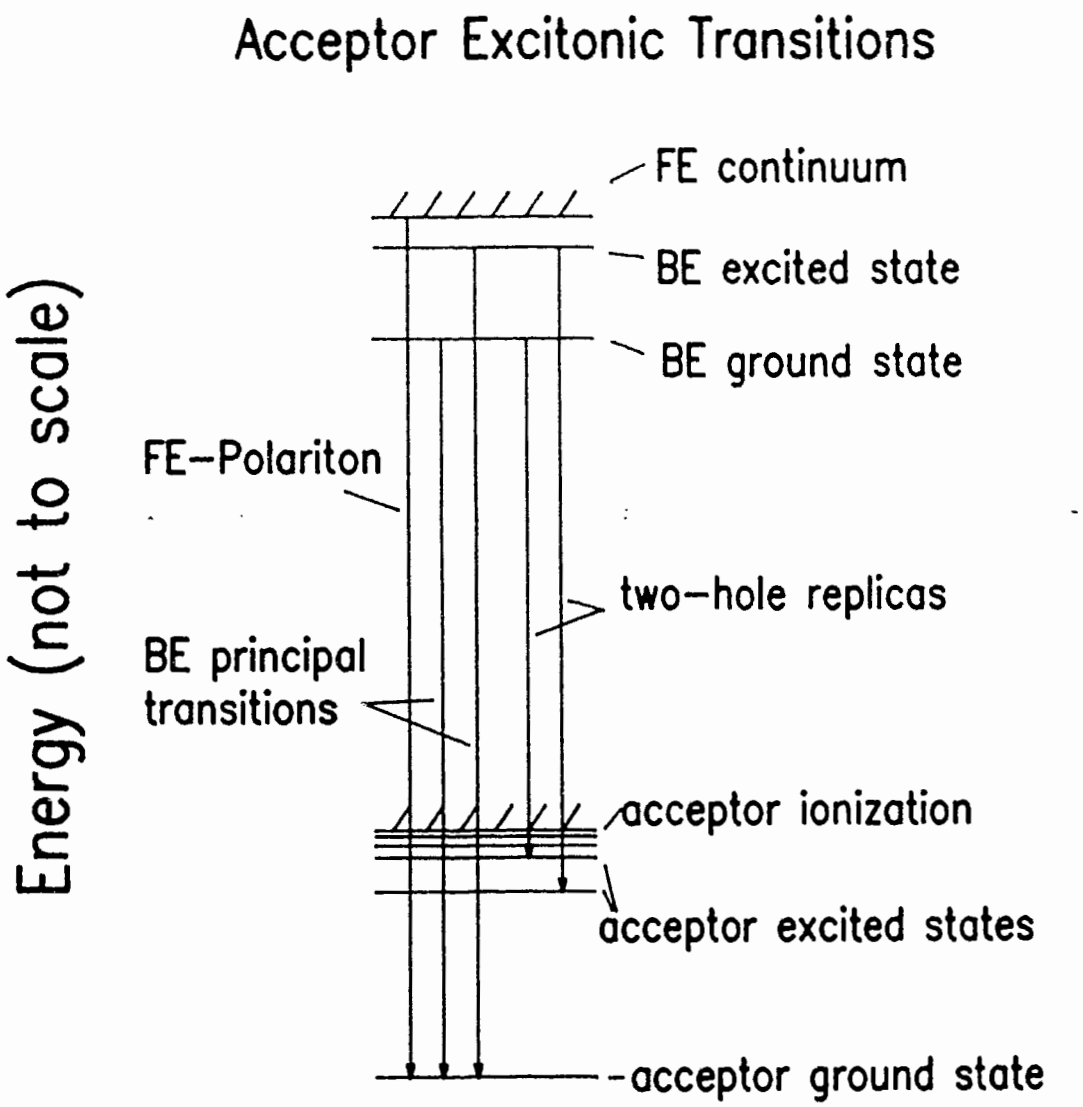

Figure 1.3

Schematic diagram of the important acceptor bound exciton PL transitions. Initial states correspond to free or bound exciton levels. Final states are the ground and excited neutral acceptor states. Transitions whose final states are the acceptor excited states are referred to as two-hole replicas, otherwise they are called principal transitions.

hole remaining afterwards undergo a transition. The counterparts of two-hole replicas for donor BE recombination are called two-electron replicas. These replicas all have linewidths comparable to the principal BE lines and therefore constitute an ideal tool for the study of impurity energy spectra. Absorption spectroscopy in the mid to far-infrared can also measure intra-impurity transitions, although selection rules may often allow the investigation of a different subset of states. For electric dipole transitions, absorption occurs between states of opposite parity (e.g. 1s $\rightarrow$ 2p) while for two-hole or two-electron replicas, more complicated rules apply. For instance, *ns*, *np* and *nd* two-electron replicas have been observed for shallow donors in GaAs [91B] whereas only ns two-hole replicas are usually reported [85R].

CHAPTER 2

EXPERIMENTAL METHODS

This chapter describes the practical aspects of the experimental techniques utilized in this work. It covers the sample experimental conditions and preparation, the sources used to generate the PL as well as the detectors and spectrometers used to analyze it. Greater attention is devoted to non-conventional aspects of the PL techniques, such as Fourier Transform Spectroscopy (FTS). More detailed descriptions of conventional PL techniques can be found in references 86Sb and 88Cb.

2.1 Samples

Four samples, referred to as sample A through D, were used for the experiments presented in this thesis. Samples A and B were used specifically to study the Y defect, while C and D served as reference samples. Sample A was fabricated using MBE at the Center for Compound Semiconductor Microelectronics (University of Illinois). It is a 10 μm epilayer grown at 590 $^{\circ}$C on a (001) oriented LEC GaAs substrate using As_2. This sample has been used in earlier work [90Sb] and thus is well characterized by independent measurements. The total acceptor concentration was measured to be 7.3×10^{14} cm^{-3}, the compensation ratio N_D/N_A = 0.27 and the liquid nitrogen temperature mobility μ_{77}= 7800 $cm^2/$ V s [90Sb]. Sample B was also fabricated using MBE but

at AT&T Bell Laboratories (Murray Hill, New Jersey) [85Sa]. This sample has a thickness of 6 μm and was grown at 630 °C on a (001) oriented LEC GaAs using As_4. The residual acceptor concentration in Sample B is approximately 10^{14} cm^{-3} [85Sa]. Sample C was also grown at AT&T Bell Labs under similar conditions as Sample B. Sample D is an ultra pure 6 μm GaAs n-type epilayer grown by MOCVD in the laboratories of American Cyanamid Company (Stamford, Connecticut). This sample was grown at 600 °C on a (001) oriented LEC GaAs substrate using tertiarybutylarsine and triethylgallium in a pressure ratio of about 30 to 1. For Sample D, the net donor concentration is ~2 x 10^{14} cm^{-3} and the liquid nitrogen temperature mobility is 120000 cm^2/ V s.

From our studies, the Y-defect appears to be found exclusively in MBE material. In fact, most MBE samples examined in our laboratory showed the presence of the Y line, although usually to a much lesser extent than sample A. The growth parameters used to obtain the high Y-defect concentration found in sample A are discussed in reference 90Sb and in section 5.2.

During the experiments, samples were held at low temperatures by immersion in liquid He in cryostats with optical access. The helium was kept below the lambda transition point by lowering the He vapor pressure below 38.5 mm Hg with the aid of mechanical pumps. Below λ, the liquid helium becomes superfluid and the boiling ceases. This reduces the amount of scattered light which translates into less noise in the monitored signal. The samples were mounted behind glass plates in a strain free manner to avoid any broadening of the PL lines.

PL experiments with magnetic field perturbations were performed in a special cryostat with a bottom optical access sample chamber located

in the vertical bore of a superconducting magnet. The superconducting NbTi/Nb_3Sn solenoid, when cooled to liquid helium temperatures, could provide fields of up to 12 T. A gear-wheel assembly was used to study the anisotropy of the Zeeman data under rotation in various crystallographic planes.

2.2 Spectrometers and Detectors

Two different spectrometers were used to analyze the PL. Most of the spectra were collected using a Bomem DA3.02 Fourier transform interferometer with a cooled RCA C30872 Si avalanche photodiode detector. Time-resolved and excitation spectroscopy was performed using a double 3/4 m grating spectrometer and a Varian VPM159A3 photomultiplier tube operated in the photon-counting mode.

The interferometer is schematically illustrated in Fig. 2.1. Its design is based on the well-known Michelson interferometer. The PL emitted by the sample is collimated and directed towards a quartz beamsplitter by an off-axis paraboloidal mirror. The light is divided by the beamsplitter into transmitted and reflected parts, which then travel along arms equipped with flat mirrors. The light recombines upon return after the introduction of a path difference as defined by the position of the scanning mirror. The resulting interference signal is focused onto the detector, digitized by a high-quality analog-to-digital converter and, stored as a function of path difference. The interferometer incorporates a single-mode HeNe laser to ensure that the interferogram is digitized at equal intervals of path difference. A

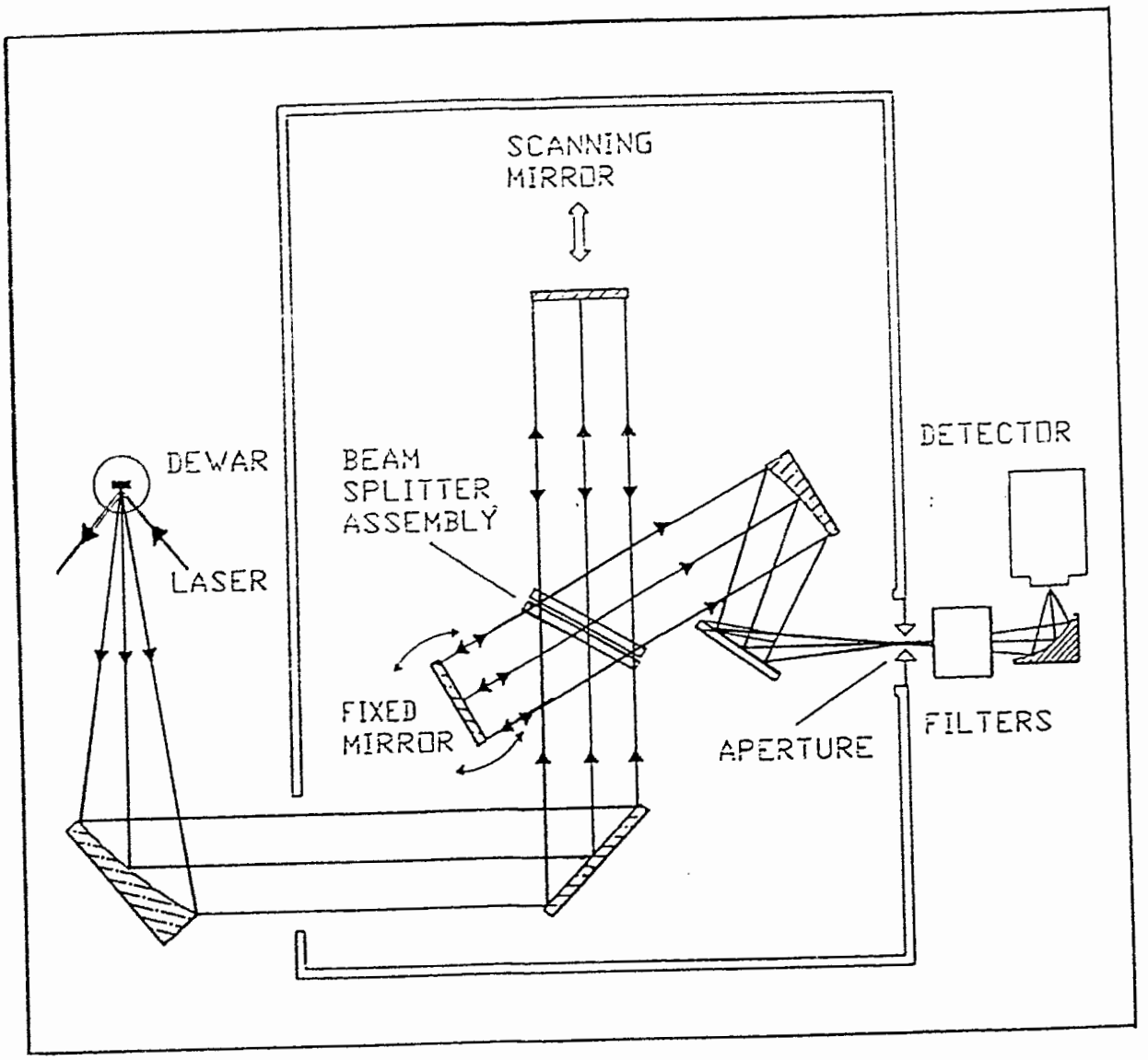

Figure 2.1

Schematic diagram of the interferometer used in this work. This apparatus is based on a classic Michelson interferometer with the improvement of dynamic alignment as explained in the text. The four collimated beams incident on the beamsplitter are the photoluminescence arm (bottom), the "fixed mirror" arm (left), the scanning mirror arm (top) and the detector arm (right). The orientation of the "fixed mirror" is dynamically changed in order to keep the interferometer aligned. A filter box mounted in the detector arm path enables the use of optical filters for light rejection.

Fourier transform performed on the interferogram enables the spectral information to be recovered. The time needed to perform mathematical manipulations on the interferogram is kept to a minimum by the use of a dedicated vector processing board where the numerical filtering and phase corrections are performed while the interferogram is being collected. The HeNe laser is also used to dynamically correct for the optical alignment of the apparatus. This is done by tilting the fixed mirror using transducers which are actuated by a servo loop receiving phase information of the HeNe interferogram sampled at three separate positions. The dynamic alignment is a crucial feature since any deviation from optical alignment results in degradation of the resolution and accuracy.

Fourier transform spectroscopy (FTS) has several advantages over conventional dispersive spectroscopy (DS) which make it a superior spectroscopic method for most applications. The throughput advantage, in particular, states that for a given spectral resolution, the ratio of the throughput of a Fourier transform (FT) interferometer over that of a grating spectrometer is typically much greater than one, especially for high resolution . The reader is referred to Bell [72B] for details. For this work, it was estimated experimentally that the signal to noise ratio of spectra collected with the grating spectrometer was approximately two orders of magnitude smaller than that collected with the FT interferometer. This high throughput characteristic of FTS made possible the study of the influence of many parameters (magnetic field strength, sample orientation in the field, polarization and combinations of such) on the PL with good resolution (about $0.25cm^{-1}$ or 0.03meV).

The major difference between Fourier transform interferometers and

conventional dispersive spectrometers is that unlike dispersive spectrometers, interferometers have no intrinsic light rejection capability. All the light fed into the interferometer impinges on the detector at all times, unless an additional optical rejection filter is used. This confers to Fourier transform spectroscopy its major advantage, called the Multiplex advantage [72B], but also its principal weaknesses. With DS only a fraction 1/N, where N is the number of analyzed spectral elements, of the light is detected at any moment. In theory, this results in a $\sqrt{N}$ advantage in using FTS instead of DS. This multiplex advantage, however, may be canceled by a $\sqrt{N}$ disadvantage if the noise from the light signal is more important than the detector noise. The situation is even worse in the presence of flicker noise (noise proportional to the signal level), in which case FTS, in fact, has a net disadvantage of $\sqrt{N}$ [90T].

The lack of rejection imposes certain limitations to FTS. First, resonant spectroscopy performed on FT interferometers necessitates some kind of external optical rejection device. This is because one is usually interested in weak features located in a spectral range very close to the laser excitation energy. Without any optical filters, the detectors are saturated by laser light. A filterbox was installed between the interferometer and the detector as shown in Fig. 2.1. Two narrow passband interference filters, one 1 nm-wide centered at 820 nm and another 10 nm-wide centered at 832 nm were used. Each of these filters could be tilt-tuned to higher energy with the aid of a holder mounted on a turntable inside the filterbox. In some cases, the passband of the 820 nm-filter was tuned to lower energy by elevating its temperature.

Another limitation associated with the lack of light rejection of FTS is in performing ultra fast (~ps) time-resolved spectroscopy. The temporal dimension of the interferogram is already utilized; it is a measure of the path difference. DS, on the other hand, is well suited for these kind of measurements. This is described in the following section.

2.3 Excitation Sources

Any light of energy larger than the band gap of a semiconductor usually suffices to excite ordinary PL. Laser light, however, has several advantages over conventional lamps. The high degree of spatial collimation allows lasers to be placed far from the studied sample. Parallel beams can also be focused into smaller spots than extended sources. This is beneficial when working with epitaxial samples which are typically of reduced size (area ~ 20 mm^2). Perhaps the most significant advantage of a laser is utilized in performing resonant excitation. Tunable lasers deliver more power in a much narrower spectral range than can be attained with filtered broadband sources.

During this work, we made exclusive use of a Titanium Sapphire (Al_2O_3:Ti) tunable laser for PL excitation. Al_2O_3:Ti is an ideal lasing material for PL studies in GaAs. The lasing species, Ti^{3+} ions dispersed in a sapphire matrix, exhibit absorption bands in the green and the blue (400-500 nm) and fluorescence at wavelengths in the range 650 to 1100 nm. The actual tuning range is determined by the mirror coatings, the tuning element losses and other factors.

A schematic diagram of the continuous wave (CW) Al_2O_3:Ti laser system is shown in Fig. 2.2. The lasing mode is contained inside the folded cavity determined by the high reflector mirror (HR), the two fold mirrors (FM) and the output coupler (OC). The mirrors allowed tuning from 700 nm to 850 nm. The pumping of the Al_2O_3:Ti laser was provided by a CW Ar ion laser operating at 514.5 nm. Approximately 10 W of Ar laser light is deposited inside the Al_2O_3:Ti crystal in a beam collinear with the infrared lasing mode by guiding the pump beam through one of the fold mirrors. The coating on these mirrors is reflective in the infrared but transparent in the green.

The tuning of the laser is achieved with a quartz three-plate birefringent filter placed inside the laser cavity. Each plate causes the linear polarization of the incident laser light to become elliptical, dependant on both the wavelength and the angle between the optical axis of the plate and the electric field of the laser light. Only a narrow range of wavelengths experience a dephasing of a multiple of 2π in each of the three plates and return to linear polarization. Wavelengths that remain elliptically polarized suffer additional loses on all the Brewster angled surfaces and are prevented from reaching lasing threshold. The laser is tuned to different wavelengths by rotating the filter with respect to the electric field of the laser light. The use of three plates of different thickness enables one to make narrow filters (~40 GHz), with orders well separated so that only one order of the filter supports lasing at a time. Narrower linewidths (<9 GHz) and finer tuning could be achieved by placing an additional etalon (not shown in Fig. 2.2) inside the laser cavity.

As seen in Fig. 2.2, a fraction of the output laser beam is fed

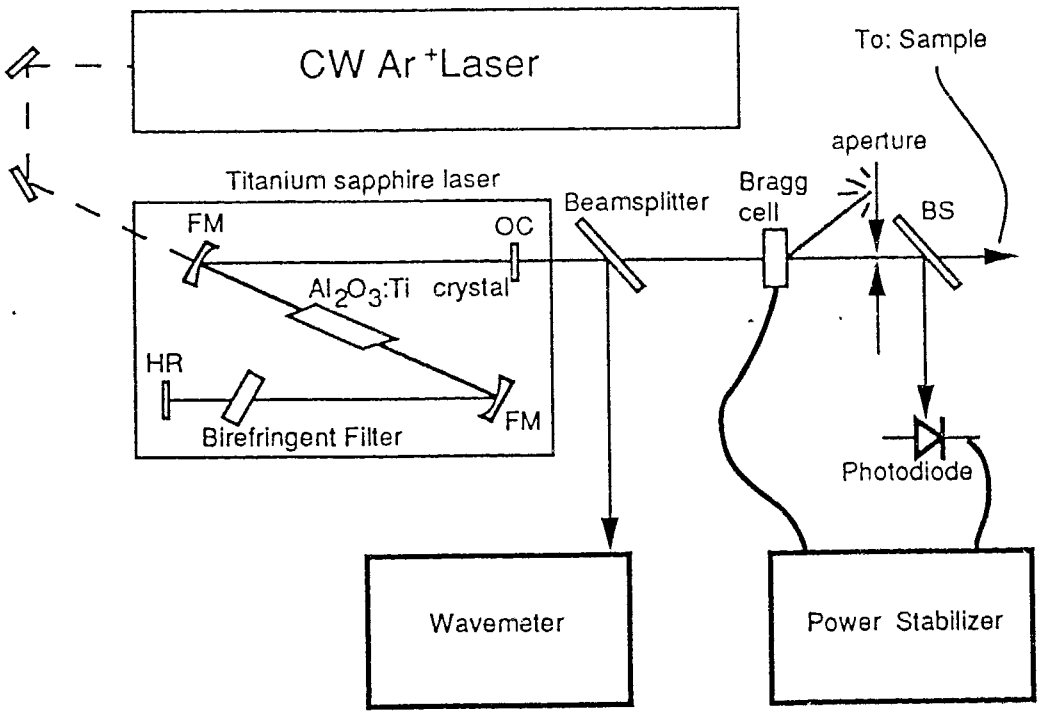

Figure 2.2

Schematic diagram of the Titanium-Sapphire Continuous Wave (CW) laser used in this work. The excitation source is a CW argon-ion laser supplying about 15 W of green light. The Al_2O_3:Ti laser output has typical power of about 1 W and can be tuned from 700 to 850 nm with the aid of the birefringent filter. The diagram shows schematically the folded Al_2O_3:Ti laser cavity defined by the high reflector (HR), the two fold mirrors (FM) and the output coupler (OC). Before reaching the sample, the output IR beam passes through a beamsplitter (BS) to feed some light into the wavemeter and through the power stabilization stage. The wavemeter and power stabilizer are described in the text.

into a wavemeter by using a simple glass beamsplitter. The wavemeter uses an interferometric principle to determine the wavelength of light with great accuracy (one part in 10^6). The beam is expanded and allowed to reflect off a Fizeau wedge onto a linear photodiode array. The interferometric pattern caused by the slightly oblique glass plates of the wedge is recorded, analyzed by a micro-computer and translated into a wavelength measurement.

In Fig. 2.2 we also show an apparatus used to stabilize the output beam power. The beam is first passed through an acousto-optic modulator where a refractive-index grating is established by a piezoelectric transducer driven by radio-frequency power. Diffracted beams are blocked by an aperture and the intensity of the remainder of the beam is monitored with a photodiode via a glass beamsplitter. A servo-loop adjusts the RF power so as to keep constant the monitored light intensity. By sacrificing a little laser power in this manner, it is possible to reduce laser intensity fluctuations. The importance of noise-free excitation was underscored in section 2.2 in our discussion of flicker noise.

The measure of PL decay curves necessitates laser pulses shorter than the decay constants of the studied transitions. The generation of picosecond pulses has been covered in detail in previous theses [86Sb, 88Cb] and will only be discussed briefly here. Modulating the laser gain at the frequency of a cavity round-trip ν_0 generates pulses at a repetition frequency ν_0 and of pulsewidth inversely proportional to the bandwidth of the optical system. A derivation of this principle can be found in reference 75Y. For this work, the gain modulation was achieved with a prismatic acousto-optic modulator contained in a unit

called a modelocker. A schematic diagram of the experimental set-up is shown in Fig. 2.3. An important alteration is made to the CW set-up (Fig. 2.2). The HR end-mirror is removed and replaced by the modelocker unit placed outside of the Al_2O_3:Ti enclosure. Inside the prism, a standing wave is driven at $\nu_0/2$ in order to modulate the index of refraction at the round trip frequency. Because of the wavelength selectivity of the prism-mirror set, the laser modes experience the required gain modulation, and modelocking occurs. The laser cavity was adjusted for a round-trip frequency of 80 MHz. The resulting output beam is a train of pulses separated by 12 ns intervals. The width of the pulses were approximately 100 ps but could be reduced to about 25 ps by removing two out of the three plates of the birefringent filter to increase the bandwidth. The width of the pulses was measured with an autocorrelator as described in reference 86Sb.

To measure the PL decay curves, we used a technique borrowed from nuclear physics called delayed coincidence photon counting [86Sb]. In this method, individual PL photons are detected and correlated in time with the exciting pulses. An avalanche photodiode sampling the exciting laser beam, and a photomultiplier collecting part of the dispersed luminescence provide start and stop pulses for a time-to-amplitude converter. The delay between the two pulses is converted to a voltage amplitude which is then analyzed by a pulse height analyzer [86Sb].

2.4 Photoluminescence Excitation

Photoluminescence excitation (PLE) is a useful method to reveal the

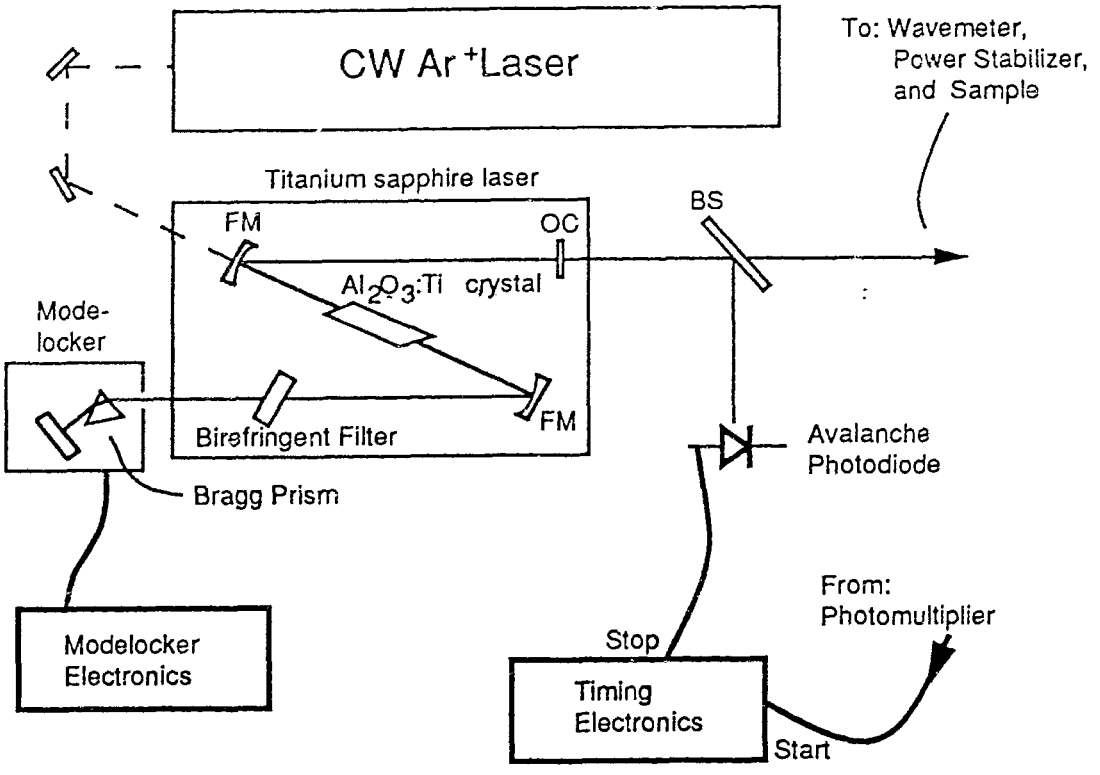

Figure 2.3

Schematic diagram of the modelocked Titanium-Sapphire laser system used in this work. The excitation source is the same as the one used for the CW Al_2O_3:Ti laser. In this case however, the Al_2O_3:Ti laser cavity is modified by removing the high reflector end mirrors and replacing it by a module called a modelocker. The modelocker generates laser pulses whose frequency corresponds to a cavity round trip. A reflection off a beamsplitter onto an avalanche photodiode supplies a Stop pulse for the timing electronics. Before reaching the sample, the output beam passes through the wavemeter and power stabilization stages described in Fig. 2.2.

excitation channels of a particular PL transition. Traditionally PLE is performed with a dispersive spectrometer. For example, a grating spectrometer is adjusted to an energy corresponding to a particular PL transition and the signal at the detector is recorded as a function of excitation energy by tuning the exciting laser in a range higher than the transition energy. A spectrum collected in this fashion in displayed in Fig. 3.2(d). PLE can also be performed with Fourier transform spectroscopy although it is not as straightforward as with dispersive apparatus [90T].

The reduced collection time of the Fourier transform interferometer has enabled us to use a different method than conventional FT PLE in order to get the PLE spectra presented in Fig. 4.9. A series of 60 ordinary FT PL spectra in the range 12186 to 12204 cm^{-1} were collected for excitation going from 12215 to 12227 cm^{-1} in steps of 0.2 cm^{-1}. The PLE spectra were constructed from this data by reading the intensities of the Y-related two-hole replicas as a function of excitation energy. Collecting and constructing a PLE spectrum in this manner is somewhat tedious, but it has the advantage of allowing the construction of a PLE spectrum for any feature in the collection passband from the same data set.

CHAPTER 3

AXIAL DOUBLE ACCEPTOR PHOTOLUMINESCENCE IN ZERO MAGNETIC FIELD

3.1 Introduction

In the course of the past few decades as GaAs crystal purity advanced, individual optical processes became resolvable and spectroscopists were able to study and explain more aspects of the PL spectra. Advances were usually achieved through comparisons with known PL processes in other semiconductors and, by studying the PL as a function of various parameters such as temperature, excitation power density, externally applied stress or magnetic fields. Interesting examples of pioneering PL research in GaAs such as donor-acceptor pair processes [71L], and acceptor BE [69Sb, W72a, 73H] can be found in the literature. Although a few controversies are still active a very coherent and complete picture of the near gap PL processes in GaAs has been established [79D]. The observation of new spectral features usually fuels intense research which attempts to keep our understanding of PL phenomena complete.

The motivation for these PL investigations is deeper than the mere desire to fill spectroscopic catalogues. Since PL directly probes impurities and defects and their electronic states, it constitutes one of the most relevant characterization and analysis techniques. The sensitivity of PL is comparable or better than the most powerful standard analysis techniques including secondary ion mass spectroscopy and atomic emission or absorption spectroscopy [76H]. In contrast to PL

these later techniques often provide inconclusive information since they detect the presence of impurities whether they cause an electronic state or not. PL is also a more direct, comparatively simple and non-destructive technique.

This work is concerned primarily with the so-called Y growth induced defect. We will start by noting that until this study, next to nothing was known about it. The principal Y-related BE transition, called Y_1 in this work, was first reported by Contour and co-workers [83C] in a MBE sample which also exhibited the characteristic KP emission. These authors noted the similarity of this line with one, previously seen by Reynolds *et al.* [80R] in a sample grown by VPE. We will demonstrate later that this assignment was erroneous. Skolnick *et al.* [85Sa] later reported that the line seen by Contour *et al.* was polarized and named it Y, but didn't comment on its nature. Recently, Szafranek *et al.* [90Sb] pointed out the correlation of the free-to-bound (e,A^0) transition of another growth induced defect-acceptor labelled A with the well known g-line often associated with the KP series [90C], as well as with Y (which they called P_0). The g-line is commonly seen at the high energy end of the KP series at 1511.1 meV but is due to excitons bound to centers distinct from those responsible for the KP transitions [90C]. The *g*-line has been observed in the absence of the KP series in samples grown by epitaxial techniques other than MBE [80K]. Szafranek *et al.* [90Sb] also reported that the the presence of the A acceptor has a profound effect on the low-temperature luminescence properties of the material, in that it appears to quench the donor BE line. This anomalous behavior has important implications for characterization techniques using PL since they are usually based on the

relative intensities of (D^0,X) and (A^0,X) [90Sc]. In samples containing the (D^0,X) quenching defect, donor concentration assessments using such methods would result in underestimated values. A discussion of this problem will follow in section 3.4.

In this chapter, the zero-magnetic field results on the Y-related BE PL are presented. First, spectra collected with non-resonant excitation are presented, followed by those obtained with resonant excitation. The lifetime of the principal BE transition is then obtained from transient PL measurements. Finally the information is summarized and possible models are examined.

3.2 Transitions with non-resonant excitation

Fig. 3.1 displays a wide range PL spectrum for sample A. The PL was excited with above gap photons at 720 nm. The spectrum shows strong emission from the KP lines as well as from the g-line. Other excitonic luminescence includes that of the polariton X and of the carbon acceptor-bound exciton (A_C^0,X). No donor-bound exciton (D^0,X) is visible in this spectrum , even though the sample is known [90Sb] to contain shallow donors. This is attributed to the presence of donor-quenching defects as discussed in the introduction. More important for this study, however, are the two features labelled Y_1 and $Y_1^\bullet$ located between (A_C^0,X) and X, and lying at energies of 12209.6 cm^{-1}(1513.80 meV) and 12215.6 cm^{-1}(1514.54 meV) respectively. Sample A exhibited much stronger Y related PL features than any other samples studied in our laboratory. Only the Y_1 feature has been previously reported in the

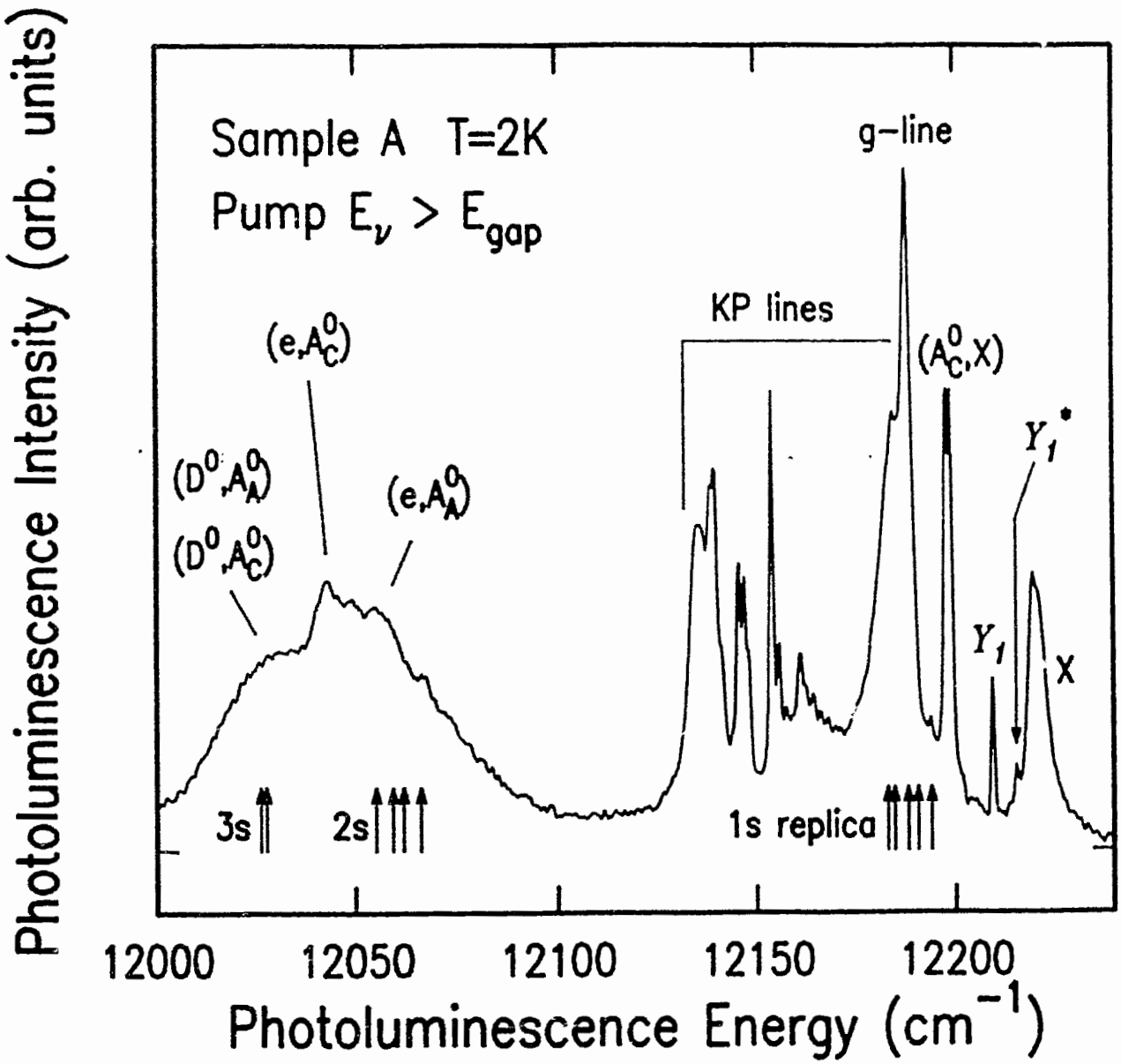

Figure 3.1

Wide range PL spectrum pumped with above gap excitation (720 nm) for sample A. Y_1 is shown along with Y_1^*, another Y-related BE recombination line, between the carbon acceptor BE (A_C^0,X) and the polariton X. Other excitonic PL includes strong KP lines and g-line but no donor BE are visible. The presence of carbon as well as the A acceptor is detected in the broad donor-acceptor pair / free-electron- to-bound hole bands. The arrows at the bottom of the figure locate the Y-related two-hole replicas studied later in this work. In all figures the tic marks at the vertical axes locate the PL zero intensity.

literature [83C]. The presence of the A acceptor is detected in the broader DAP (D^0, A^0_A) band as well as free electron-to-bound hole (e, A^0_A) band around 12050 cm^{-1} (1494 meV) [90Sb]. Note that in this sample, carbon is the major contributor to the (D^0, A^0) and (e, A^0) bands. The arrows at the bottom of the figure indicate the spectral positions of the Y-related two-hole replicas which are presented in the next section.

Fig. 3.2 focuses on the near-gap region around 12200-12230 cm^{-1} (1512.5-1516.3 meV) where Y_1 and Y_1^* are found. Fig. 3.2(c) shows a highly resolved portion of Fig. 3.1 from a spectrum taken under the same conditions. On this scale, the weak donor related (D^0,X), (D^+,X) and (D^0,h) features are visible. The lineshape of the polariton X clearly shows the characteristic notch referred to in chapter 1. The two strong peaks around 12198 cm^{-1} (1512.4 meV) and the smaller one at higher energy have been labelled as (A^0_C,X). The multiplicity of the observed feature has been explained as a consequence of the bound particle interactions in the field of the acceptor [87Sb]. A short account of how these interactions are taken into consideration will be presented here.

In the carbon acceptor BE initial state, there is one electron and two holes localized in the Coulomb field of the acceptor. The coupling of the two identical j = 3/2 holes yields one J = 0 singlet and one J = 2 quintuplet. The J = 1 triplet and J = 3 septuplet are excluded by the requirement that the resultant states must be antisymmetric. To account for the observed structure of the (A^0,X) PL, an additional interaction causing some splitting in the quintuplet has to be considered. Originally, this interaction was proposed to be the electron-hole exchange [74Wa]. Using a j-j coupling of the electron and

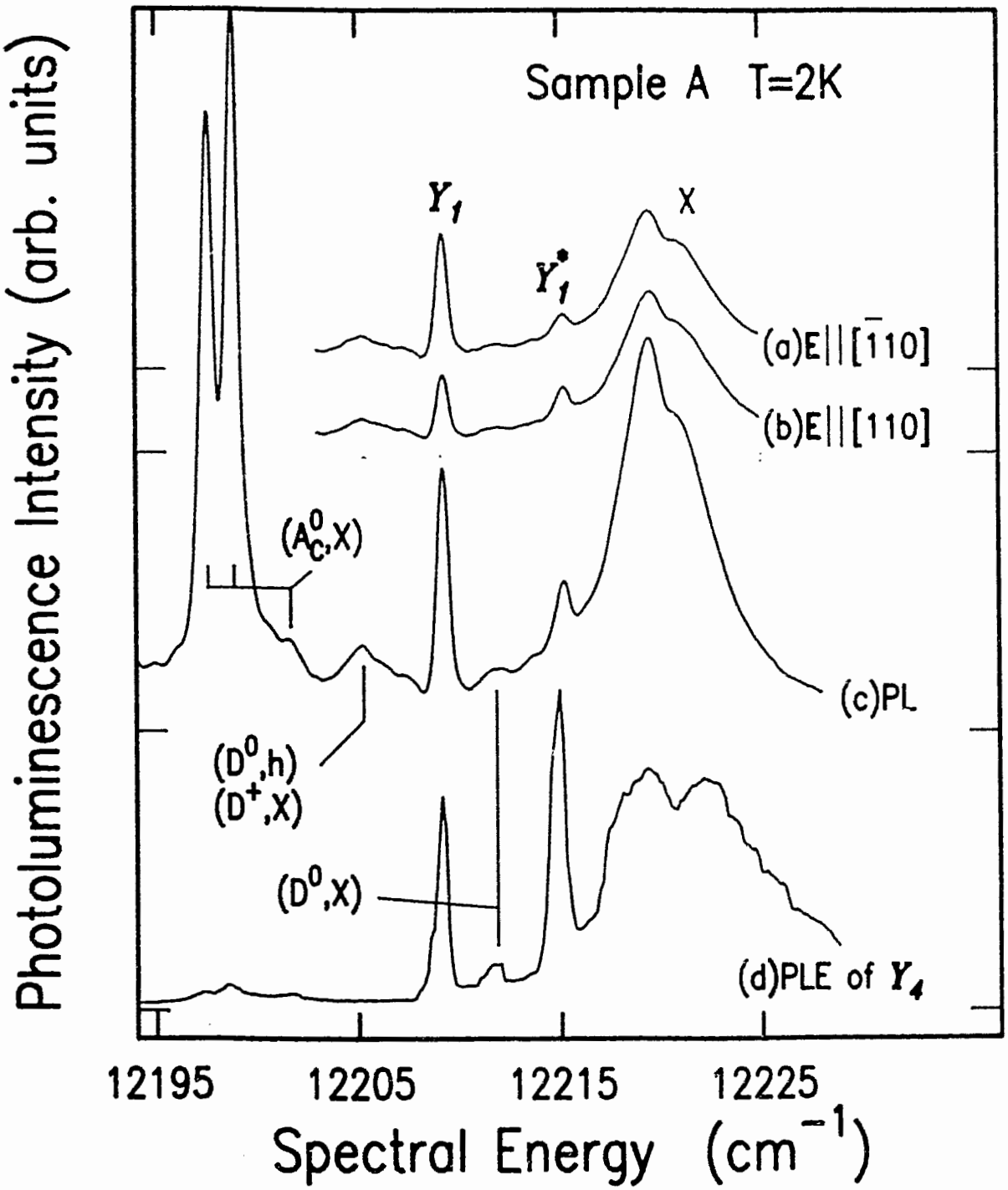

Figure. 3.2

Unpolarized (c) and linearly polarized (a) and (b) near gap PL spectra showing Y_1 and Y_1^*. Y_1 is 35% polarized along [$\bar{1}$10] while Y_1^* is 15% polarized along [110]. (d) shows a photoluminescence excitation spectrum where the detection energy was set on Y_4, a two-hole replica of Y_1. The enhancement observed at Y_1 and Y_1^* indicates that these transitions are related.

the holes scheme, White *et al.* [74Wa] labelled the three (A^0,X) lines as $J = 5/2$, $J = 3/2$ and $J = 1/2$ in order of increasing energy. Other authors later proposed the additional interaction to be the cubic field of the crystal instead of the electron-hole interaction [84M]. The cubic crystal field illustrates the fact that the $u_{nk}(r)$ Bloch parts of the electronic wavefunctions in equation 1.2 don't have the full spherical symmetry as is considered in a pure j-j scheme but are instead modulated by the T_d crystal field. This interaction also leads to a splitting of the $J = 2$ level, resulting in three lines for (A^0,X). In this case the labels used , $\Gamma_8, \Gamma_{7,8}$ and Γ_6 in order of decreasing energy, are representations of T_d associated with the corresponding states.

It is impossible to decide which of the two scenarios is valid simply on the grounds of the observed structure of (A^0,X). The conflict can be resolved by studying the behavior of these levels under external perturbations. Theoretical fits of the (A^0,X) transitions under uniaxial stress in GaAs [87Sb] clearly favor the crystal field scheme over the j-j coupling scheme. Difficulties in fitting the magnetic field splitting of these transitions using j-j coupling theory [74W, 75S] also indicate that the crystal field scenario is a more plausible explanation. This example illustrates the strength of spectroscopic methods used in conjunction with externally applied perturbations. A similar analysis will be used to explain the Y-related PL results. We now return to the presentation of the Y data.

The full width at half maximum of the Y_1 and Y_1^* transitions in Fig. 3.2 is about 40 μeV, or four times less than kT for T = 2K. This indicates that the transitions involve no free particles but, rather

localized ones. The lineshapes of Y_1 and Y_1^* are similar to that of (A_C^0, X) and quite different from that of the free-electron-to-bound-hole (e, A^0) band seen in Fig. 3.1. Y_1 and Y_1^* are suggested to be transitions from the ground state and excited state of a BE, respectively, to the ground state of the neutral impurity. These types of transitions are referred to as principal BE transitions and are depicted in Fig. 1.3.

A simple and direct verification of the relation between Y_1 and Y_1^* is presented in the excitation spectrum of Fig. 3.2(d). The transition monitored is Y_4, a two-hole replica of Y_1. Y_4 will be presented in the next section. Aside from the notched polariton X, the dominant excitation channels in that region correspond to the lines Y_1 and Y_1^*, supporting the suggested relation between Y_1 and Y_1^*. In Fig. 3.2(d), data from the Y_1^* peak correspond to the following multistep process: 1) Photons are absorbed at Y_1^*, resonantly populating the excited BE level, 2) The system relaxes to the BE ground state and 3) A Y_4 two-hole transition occurs and is detected at the corresponding energy.

Perhaps the most striking feature of the Y-related PL lines is that they are polarized. Linearly polarized PL emissions for these lines are shown in Fig. 3.2(a) and Fig. 3.2(b). The crystallographic convention chosen here is based on that defined by Skolnick [85Sa] for reporting the polarization of the KP lines. According to this convention, Y_1 was found to be 35% polarized along $[\bar{1}10]$ and Y_1^* was 15% polarized along [110]. This implies that the local symmetry of the center binding the exciton is lower than T_d, the full symmetry of the GaAs lattice. The defect involved is therefore not a point defect but a complex of some sort, the simplest possibility being a set of two point defects aligned along a particular direction.

Fig. 3.3 illustrate the dependence of the near-gap PL from sample A on excitation wavelength. Note that the (A_C^0,X) transitions have been scaled down by a factor of about 1.5 on all spectra. A surprising enhancement of the donor related PL features is observed by using longer wavelength excitation. Absolute PL intensity of all features is seen to increase but more dramatically for $(D^0,h)/(D^+,X)$ and (D^0,X). This overall increase is associated with using more penetrating, longer wavelength light. It can be understood as resulting from a more extended excited volume which decreases the importance of competitive recombination processes occurring at the surface [74H, 90Z]. We suggest that there exists a large concentration of defects close to the surface of the GaAs layer that are robbing excitons bound to impurities and therefore quenching their PL intensity. Considering the greater spatial extent of a (D^0,X) as compared to that of a (A^0,X), it is natural to assume that the (D^0,X) would be perturbed more drastically than (A^0,X). This competing center does not seem to be Y since the Y_1 and Y_1^* BE lines are not enhanced by using shorter wavelength excitation. For the purpose of this study, we simply note that in order to simplify the detection of the Y signatures, shorter excitation wavelength is preferable, since it reduces spectral interference from donor-related features.

No drastic changes are expected for a change of excitation wavelength in the spectral range above the band gap energy. Spectacular alterations to the PL spectra are predicted, however, if the excitation energy is set in resonance with BE features. This is the topic of the next section.

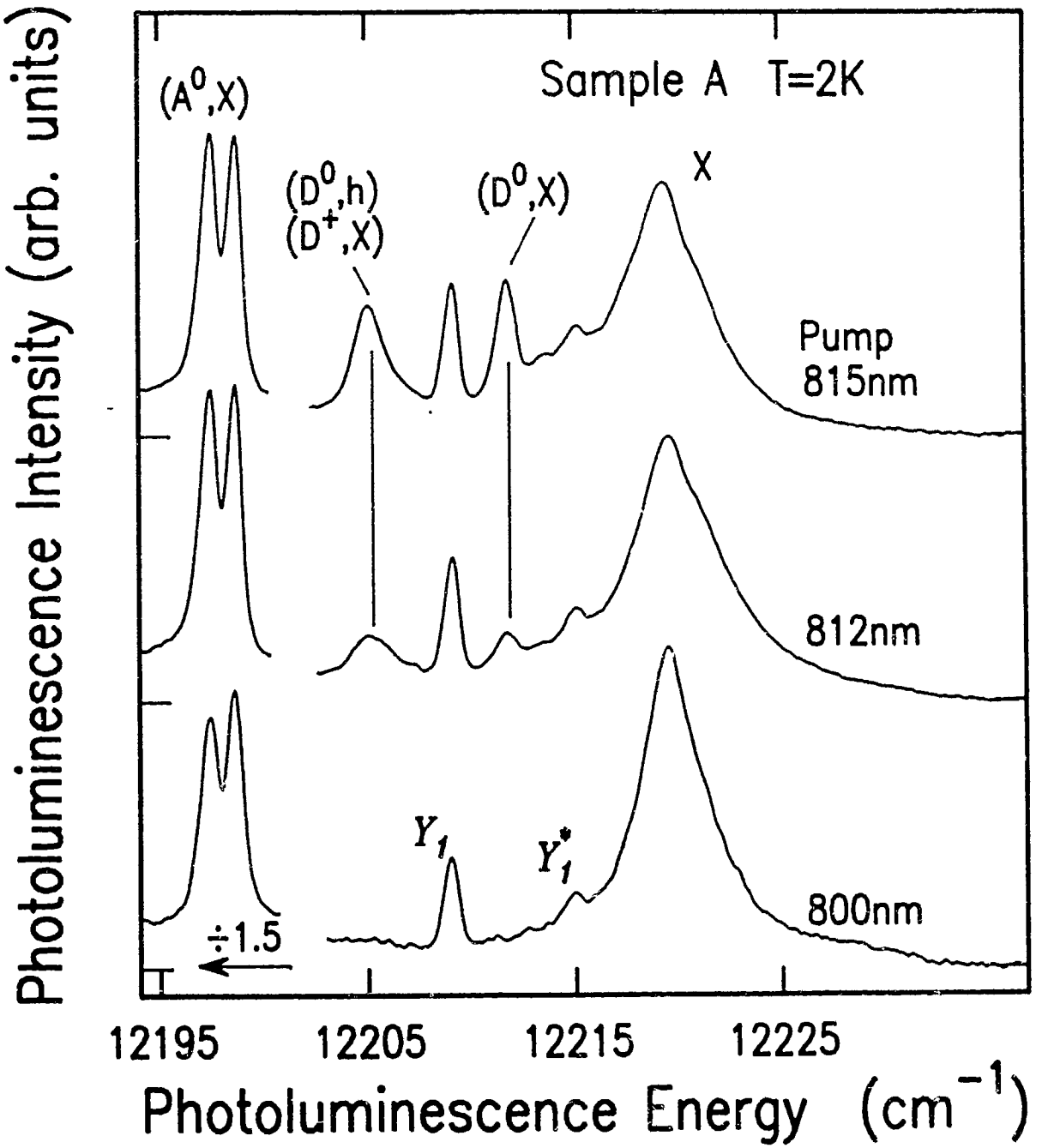

Figure 3.3

Influence of the excitation wavelength on the near-gap PL of sample A. The same spectral range as shown in Fig. 3.2(c) is displayed for excitation at 815 nm, 812 nm and 800 nm. The (A_C^0,X) has been scaled down by a factor of 1.5. The enhancement of the donor related PL features associated with longer wavelength is attributed to the presence of competing centers near the surface of the sample.

3.3 Transitions with resonant excitation

Resonant excitation is a very powerful method for the study of weak replicas in direct gap semiconductors. When the laser excitation is set in resonance with a particular principal BE state, excitons bound to the corresponding centers are selectively created in great number. This enhances the related BE features, in particular the two-particle replicas.

Two-particle replicas in the vicinity of the g-line, obtained using unpolarized resonant excitation set on Y_1 and Y_1^*, appear in Fig. 3.4(a) and Fig. 3.4(b) respectively. The resuts are shown for sample B, although very similar selectively excited two-hole replicas were also observed in sample A (not shown). In both cases, a narrow passband filter (1nm wide) centered around 12187 cm^{-1} was used to prevent the laser light from saturating the detector. In Fig. 3.4, three replicas Y_2, Y_3 and Y_4 can be seen by pumping Y_1 while two additional replicas Y_2^* and Y_3^* appear when pumping Y_1^*. The presence of Y_2 and Y_3 in Fig. 3.4(b) indicates that the excited level of the BE complex relaxes quickly to the ground level. The transition energies of Y_1 and Y_1^* as well as the others detected in this study are reported in Table 3.1.

Fig. 3.5 is a schematic energy diagram similar to that presented in Fig. 1.3. It summarizes all the Y-related BE transitions seen in this work. Energy separations within the brackets on the left side represent the splitting of the initial and final states. These separations are drawn to the scale indicated, but the various brackets have been brought closer together to allow a greater magnification of small details. The

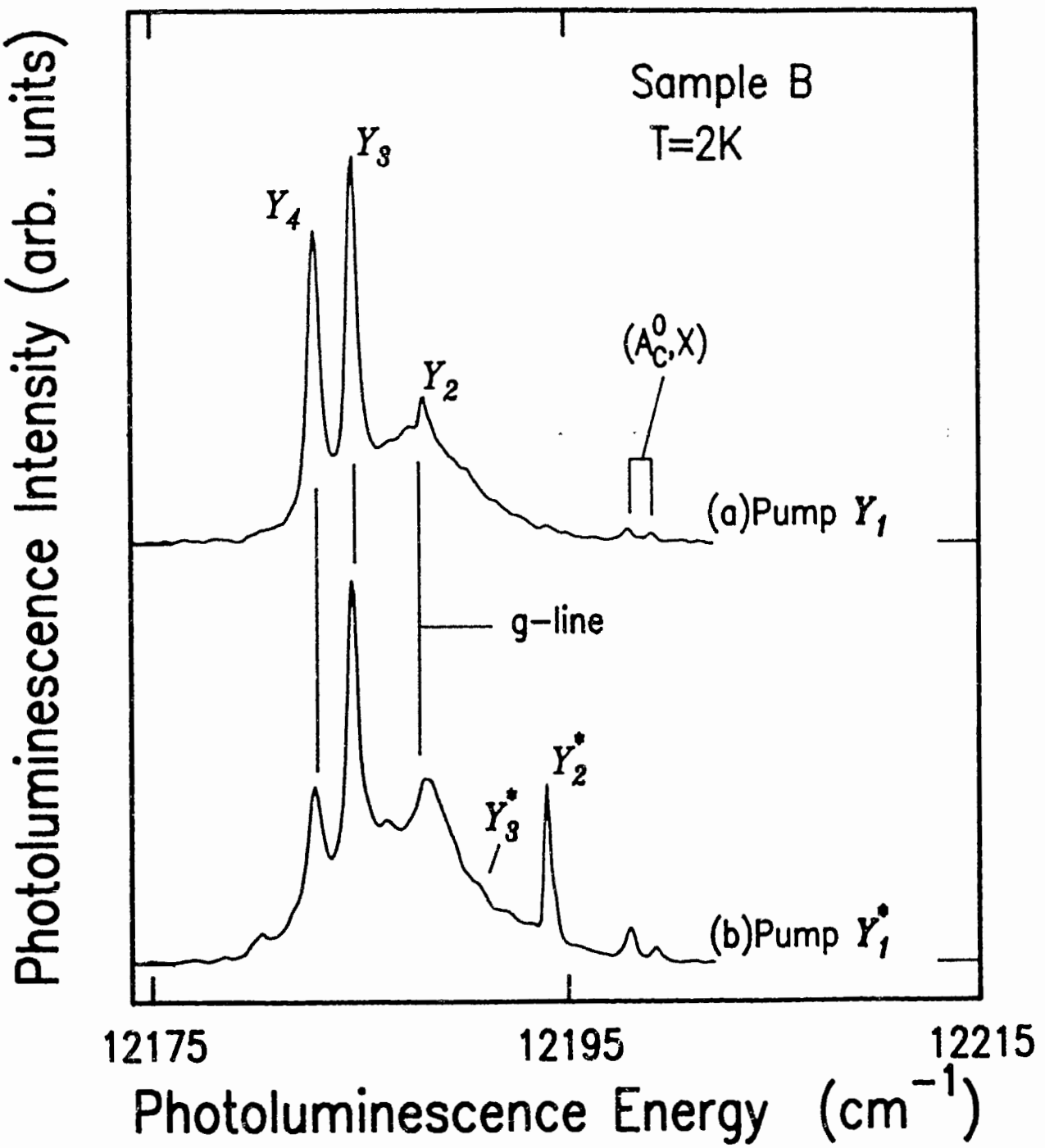

Figure 3.4

Photoluminescence spectra for sample B in the vicinity of the g-line with unpolarized excitation set on (a) Y_1 and (b) Y_1^*. A narrow passband filter (1 nm) centered around 12187 cm^{-1} is used to reject the laser light. Three Y_1 1s two-hole replicas (Y_2,Y_3 and Y_4) appear in (a) while two (Y_2^* and Y_3^*) are detected for excitation at Y_1^*.

Table 3.1 Spectral positions of the Y-related bound exciton recombination lines in GaAs. The transitions are arranged in two column according to their initial state. In the first column we list the transitions with initial state in the ground state of the bound exciton, in the middle column those with initial state in the excited bound exciton state. The last column indicates the energy separations between the first and second columns.

line	spectral energy (cm^{-1})	(meV)	line	spectral energy (cm^{-1})	(meV)	separation (cm^{-1})	(meV)
Y_1	12209.6	1513.80	Y_1^*	12215.6	1514.54	6.0	0.74
Y_2	12188.1	1511.13	Y_2^*	12194.0	1511.86	5.9	0.73
Y_3	12184.7	1510.71	Y_3^*	12190.6	1511.44	5.9	0.73
Y_4	12182.9	1510.49	Y_4^*	not seen		--	--
Y_0^{2s}	12060.4	1495.30	Y_0^{*2s}	12066.3	1496.03	5.9	0.73
Y_1^{2s}	12059.5	1495.19	Y_1^{*2s}	not seen		--	--
Y_2^{2s}	12056.1	1494.77	Y_2^{*2s}	12062.0	1495.50	5.9	0.73
Y_3^{2s}	12055.5	1494.69	Y_3^{*2s}	not seen		--	--
Y_4^{2s}	12055.2	1494.65	Y_4^{*2s}	not seen		--	--
Y_1^{3s}	12027.9	1491.27	Y_1^{*3s}	not seen		--	--
Y_{3+4}^{3s}	12026.4	1491.08	Y_{3+4}^{*3s}	not seen		--	--

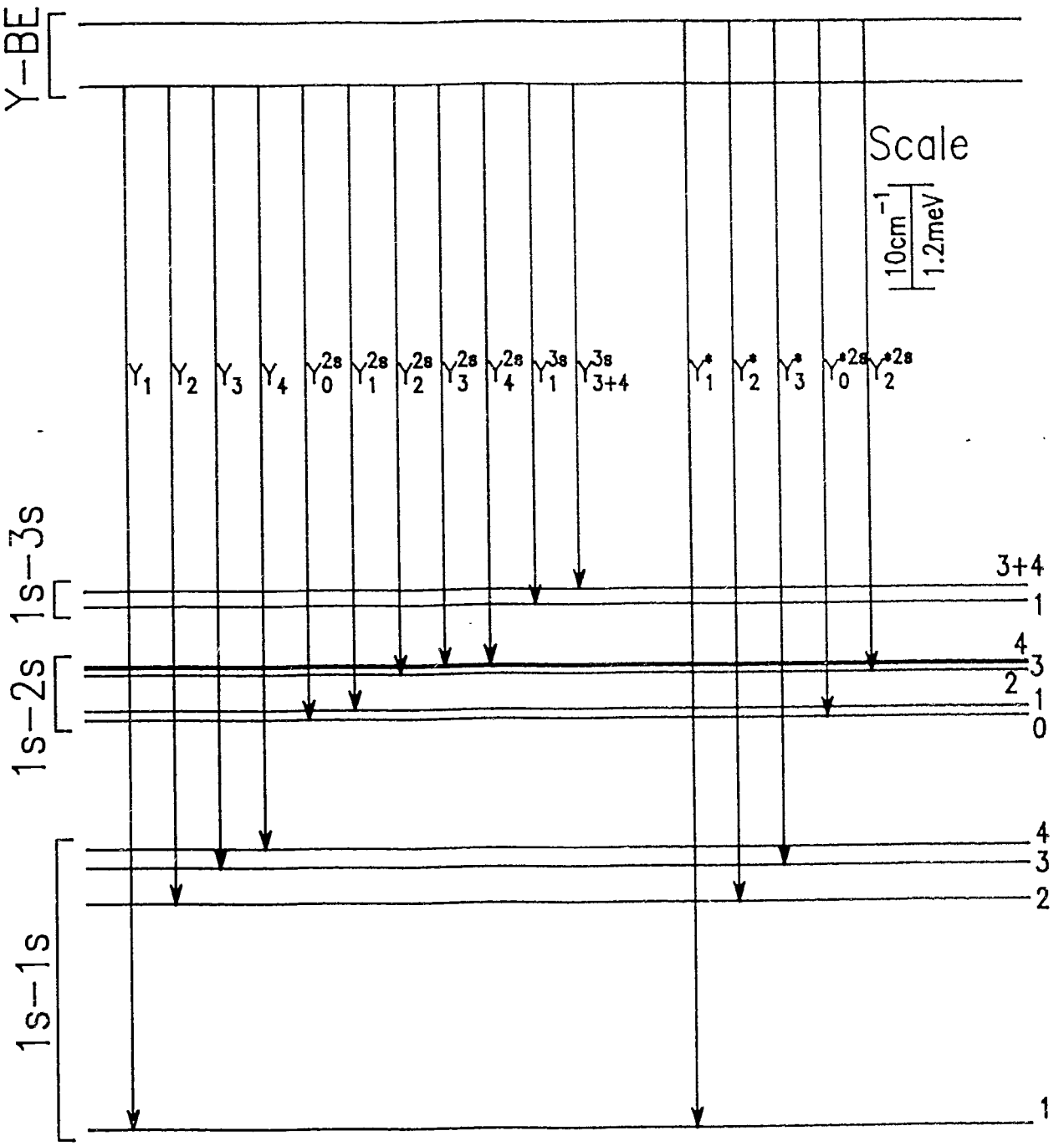

Figure 3.5

Summary of all the Y-related BE PL transitions seen in this work along with the labelling scheme used. The exact spectral energies of the transitions can be found in Table 3.1. Inside the level brackets on the left, the energies are drawn to scale. The two initial state level represent BE states while the many final state levels are various neutral double acceptor states.

nature of the splittings will be discussed later. The two transitions seen in non-resonant PL spectra, Y_1 and Y_1^* in Fig. 3.1, are transitions to the ground state of the bare complex from the ground state and the excited state of the BE, respectively. The five replicas seen in Fig. 3.4 are also indicated in Fig. 3.5.

The observation of two-particle transitions allows a few important conclusions to be drawn. First, it clearly demonstrates that the bare Y-center contains charged particles of its own. It is therefore a donor or an acceptor but certainly not an isoelectronic center. Second, the spectral energies of the replicas indicate that the complex is, in fact, a double acceptor. This statement necessitates further justification which can be provided by the observation of more replicas than the ones shown in Fig. 3.4. At this point, we will assume that our identifications of the binding center is correct. The labelling scheme will be presented next, after which justification for the proposed identity of the Y center will be provided.

Unlike the case of a single acceptor BE where each of the 2s, 3s, etc. levels is a single level, the observed 1s-1s, 1s-2s and 1s-3s (one hole in the 1s and one hole in the 3s orbital state) levels in the case of the Y system exhibit some resolvable structure. The structure of the 1s-*n*s levels is illustrated in Fig. 3.5. We find four levels in the 1s-1s bracket, five in the 1s-2s bracket and two in the 1s-3s bracket. The observed structure arises from the interactions between the two holes in the field of the defect. A detailed model accounting for this will be presented in section 3.5.

The labels used to identify each of the Y-BE transitions contain a number of indices. For the transitions that have their final state in

the 1s-1s set, we use the following convention. A subscript on the right hand side of the transition label Y designates the final state of the transition; 1 for ground state and i+1 for the i^{th} excited final state. The presence of a superscript star indicates that the initial state was the excited state of the BE complex. Its absence indicates that the transition originated from the BE ground state. Transitions with final states in the 1s-2s or the 1s-3s set are described by similar labels except that an additional 2s or 3s right hand side superscript are used.

2s and 3s two-hole replicas obtained in sample B using the same resonant excitation conditions as in Fig. 3.4 are displayed in Fig. 3.6. The Y replica as well as non-resonant carbon acceptor BE replicas appear superposed on the DAP and the (e,A^0) emission bands. Sample B exhibited smaller $(D^0,A^0)/(e,A^0)$ bands than sample A and was therefore more appropriate for the study of these low-energy Y replicas. Fig. 3.6(a) shows three Y_1-related 2s replicas, Y_{3+4}^{2s} at 12055.3 cm^{-1} (1494.67 meV), Y_2^{2s} at 12059.5 cm^{-1} (1595.19 meV) and Y_0^{2s} at 12060.4 cm^{-1} (1495.30 meV). In the 2s replicas, since the two holes are in different orbital states, we expected to observe symmetric as well as antisymmetric coupled hole states. The final state of the Y_0^{2s} transition was not visible in the 1s manifold and is thus believed to belong to the symmetric subset of states generated by the coupling of two inequivalent holes. Y_{3+4}^{2s} contains the overlapping 2s replicas from the second and third excited final states in agreement with the strong Y_3 and Y_4 replicas of Fig. 3.4. This will be verified in a subsequent figure where Y_3^{2s} and Y_4^{2s} are better resolved. Similar but weaker 3s replicas are also visible around 12027 cm^{-1} (1491.16 meV). Fig. 3.6(b) shows additional

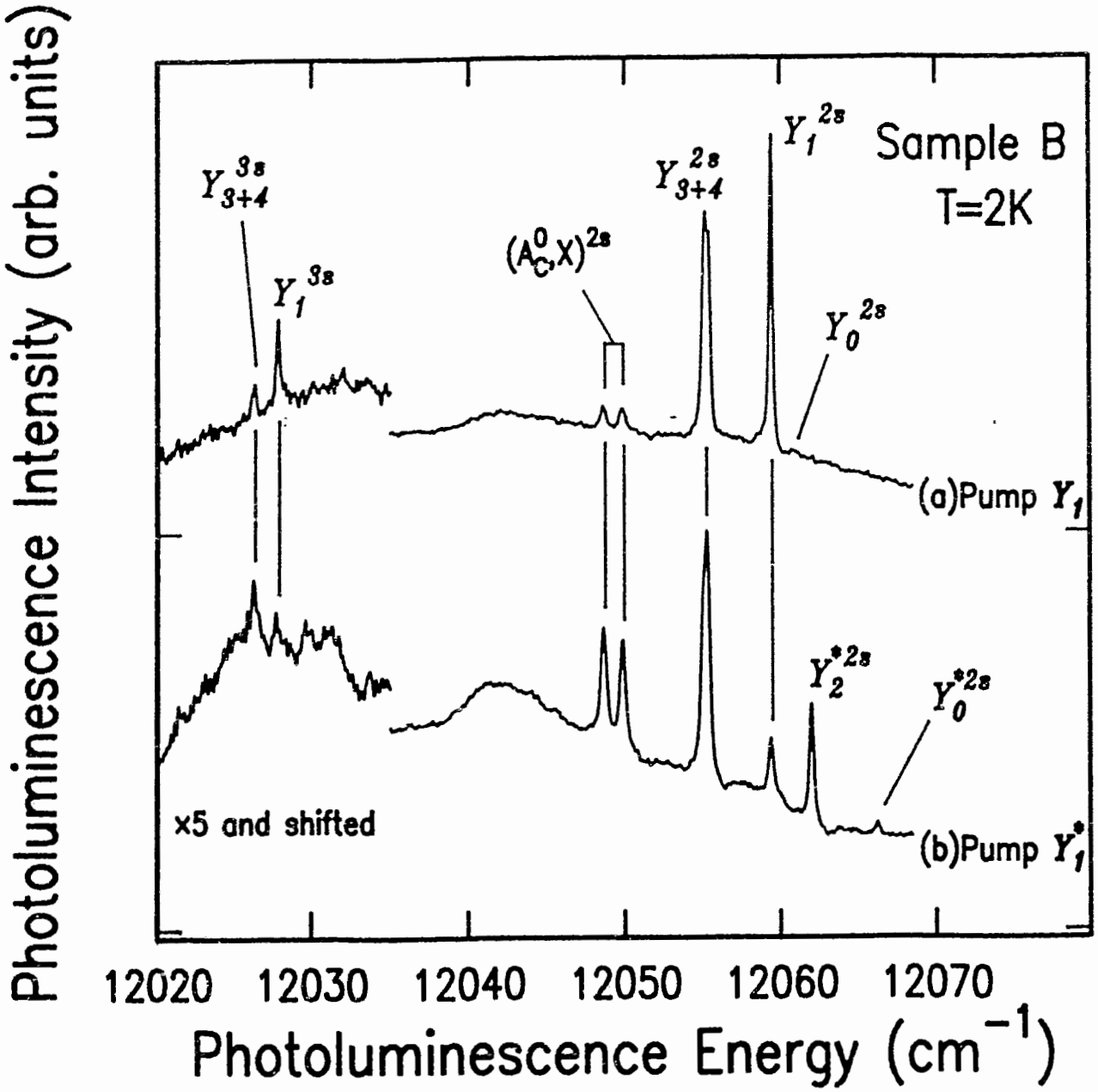

Figure 3.6

PL spectra for sample B in the vicinity of the donor-acceptor pair / free-to-bound bands with unpolarized excitation set on (a) Y_1 and (b) Y_1^*. The transitions Y_0^{2s}, Y_1^{2s}, Y_{3+4}^{2s}, Y_0^{3s} and Y_{3+4}^{3s} are two-hole replicas associated with Y_1. The replica Y_2^{*2s} and Y_0^{*2s} detected for excitation on Y_1^* indicate that the excited initial state BE transitions mainly couple with final states to which the ground BE initial state does not couple strongly.

2s replicas (Y_2^{*2s} and Y_0^{*2s}) for the excitation set on Y_1^*. As was the case for the 1s replicas, coupling to a particular level in the 2s final state seems to be dependent on the BE initial state. Here the ground state couples well to 1, 3 and 4 whereas the excited BE state couples mainly to 0 and 2.

Many spectroscopic observations support the suggested level assignments that were presented in Fig. 3.5. First, the energy differences between the various Y-Y^* spectral pairs is a constant (see Table I) confirming that the transitions in the pairs share one state. In fact this 6 cm^{-1} (0.7 meV) separation needs to be in the initial state of the BE transitions to explain the observed replica spectrum. Had it not been in the initial state, it would have been impossible to observe two sets of 2s replicas separated by this energy. The grouping of 2 hole replicas under a particular 1s-*n*s label relies on the following observations: 1) the energy where each group appears in close analogy to the excited state spectra of known acceptors [75A] and 2) the strong similarity of the structure within each group. This similarity is further examined in Fig. 3.7.

Fig. 3.7 displays on the same graph the polarization study of the 1s and 2s replicas (with the exception of the weak Y_0^{*2s}) in sample B. Two labels were used for each set of two spectra. The label on the right hand side indicates the polarization of the excitation and the level that was pumped. The label between the two spectra describes the polarization of the PL collected. π-polarized excitation or collection was obtained by passing the corresponding beam through a linear polarizer oriented parallel to [110]. For σ-polarization, the polarizer was set parallel to [$\bar{1}$10]. On all spectra, Y_4^{2s}, Y_3^{2s} and Y_2^{2s} (Y_2^{2s} is

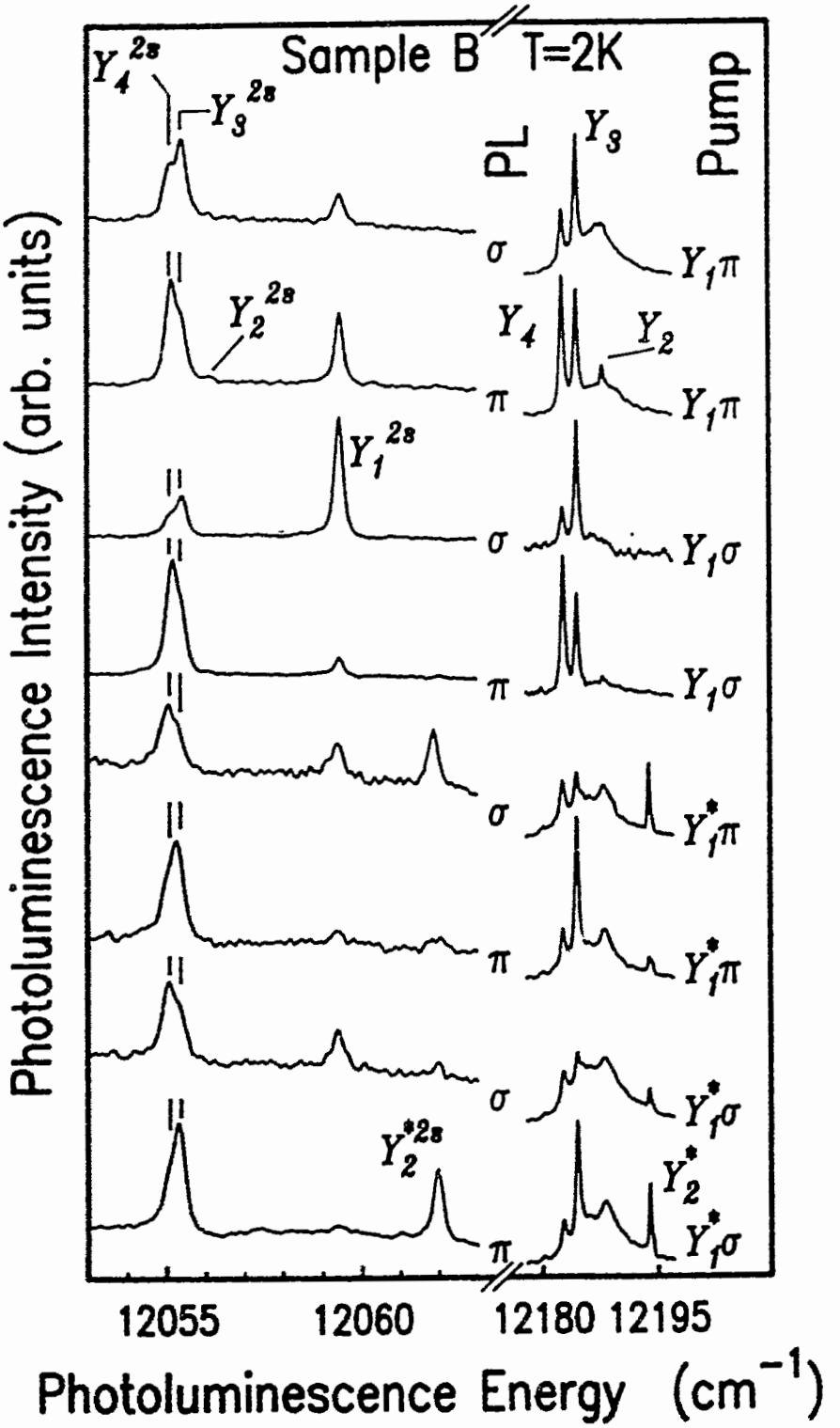

Figure 3.7

Comparison of the linearly polarized 2s and 1s two-hole replica PL for different linearly polarized excitation at Y_1 and Y_1^*. Labels appear on the right for excitation polarization and between the two spectra of a set for emission polarization. π refers to polarization parallel to [110] while σ refers to $[\bar{1}10]$. The correlation observed between the 1s and 2s replica groups is commented in the text.

visible for the first time in the second spectrum from the top) show a clear correlation with their 1s replicas. Y_2^{*2s} also correlates well with $Y_2^{\bullet}$ on the lower four spectra of Fig. 3.7. Similar correlation between Y_{3+4}^{2s} and Y_{3+4}^{3s} and between Y_0^{2s} and Y_0^{3s} is noted on the two spectra presented in Fig. 3.6.

We will now examine more closely the possible assignment for the nature of the Y-defect. First we show that it is not likely to be a donor. As mentioned in chapter I, donor ionization energies are around 6 meV whereas the measured 1s-3s separation alone for Y is more than 20 meV. A more compelling indication of the hole-like character of the Y-complex is the structure found within the *ns* multiplets. The coupling of two twofold degenerate $j = 1/2$ electrons yields only one antisymmetric state, the $J = 0$ singlet. On the other hand, two $j = 3/2$ holes yields two antisymmetric set of states, one $J = 0$ singlet and one $J = 2$ quintuplet. This last $J = 2$ level can split in up to five levels if interactions such as the cubic crystal field or the defect axial field are considered. An example of the effect of the cubic crystal field on a $J = 2$ level was presented earlier for the case of the single shallow acceptor BE [84M]. As we will see later, a coupled 3 or 4 holes system is unsuited to explain the data.

Having confidence in the interpretation of the data, it is now possible to estimate the ionization energy of the first hole of the Y double acceptor. High lying excited states such as 3s are associated with extended wavefunctions and therefore probe the central cell potential weakly. Ionization energies for such states are therefore well modeled by the effective mass theory. Using the Y_{3+4}^{3s}-Y_1^{3s} middle point to Y_1 energy separation and the Effective Mass (EM) 3s ionization

energy [90Sa], we calculated the binding energy to be 214 ± 2 cm^{-1} (26.5 ± 0.2 meV), close to the EM ionization energy of 210 cm^{-1} (26.0 meV) [82L]. The binding energy of Y is significantly different from the value reported for the A acceptor (24.8 ± 0.2 meV) [90Sa], indicating that the A and Y defects are not the same. The prototypical EM acceptor in GaAs is the substitutional C_{As} with an ionization energy of 26.0 meV [90Sa], nearly identical to that of Y. This situation makes far-infrared absorption an inappropriate technique to study Y in MBE samples since the signal from Y would be superposed on the large contribution from the ever-present carbon acceptor.

Although the Y neutral complex binds a hole with nearly the same energy as carbon, the exciton localization energy of the Y_1 BE ground state is only half that of (A_C^0, X). This observed discrepancy merely underscores the differences between a simple substitutional single acceptor such as C_{As}, and a considerably more complicated system with coupled holes in a symmetry reduced environment. A comparison of the Y system with the KP lines is more appropriate, since both systems are believed to be due to bound excitons associated with axial double acceptors. The different KP lines are thought to be due to complexes with the constituents at varying spatial separations, resulting in the number of observed transitions [88S, 90C]. Charbonneau *et al.* [88Ca] measured the binding energy of 30 individual KP acceptors, thus enabling a linear relation to be established between the acceptor binding energy and the localization energy. Extending this relationship to shallower binding energies reveals an excellent agreement between Y and the KP family as seen in Fig. 3.8. Using a Y_1 localization energy of 1.4 meV, the binding energy prediction of 26.4 meV is in excellent agreement with

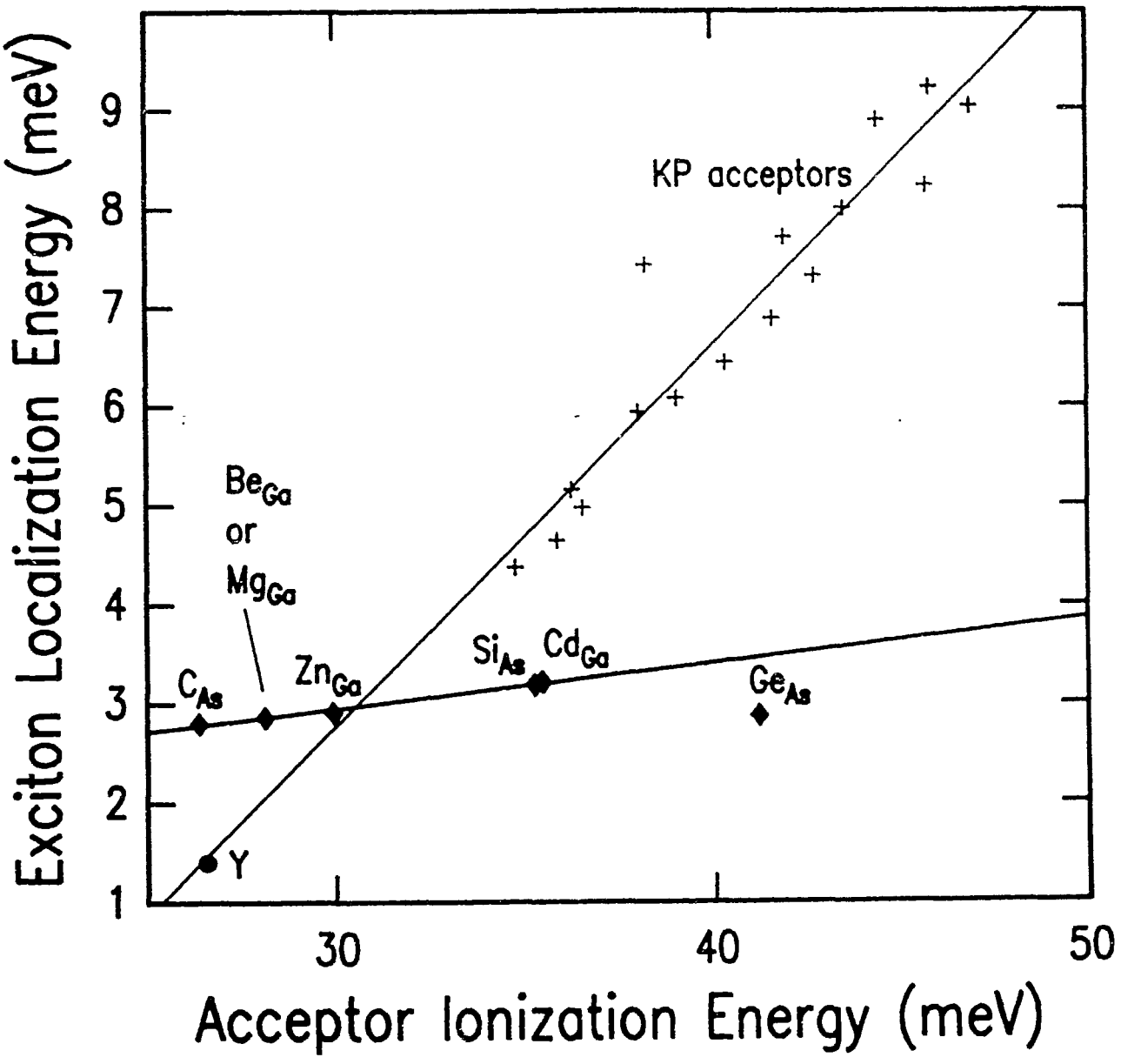

Figure 3.8

Exciton localization energy versus acceptor ionization energy for the KP-acceptors, the Y-acceptor and most substitutional (single) acceptors found in GaAs. A relation of Haynes' type is verified both for the single acceptors (excluding Ge_{As}) with a=0.046 and b=1.57 and for the KP double acceptors with a=0.38 and b=-8.8. The Y-acceptor, which was not included in the least square fit used for the KP-acceptors, falls very close to Haynes' relation found for those defects. This support our assignment of Y as a double acceptor. The data was obtained from 88Ca for the KP-lines and from 73W and 91B for the substitutional acceptors.

the value obtained in this work. We do not suggest the Y complex to be part of the KP family but merely of similar nature. For comparison, in Fig. 3.8 we also plotted Haynes' relation for simple substitutional acceptors in GaAs. The data shown on Fig. 3.8 for these acceptors was taken from reference 73W and 91B.

3.4 Transient photoluminescence

The spontaneous rate for a transition from initial state i to final state f is related to the absorption rate by the equation [82Db]:

$$A_{fi} = B_{if} \frac{\hbar\omega_0^3}{\pi^2 c^3} \qquad (3.1),$$

where B_{if} and A_{fi} are Einstein's absorption and spontaneous emission coefficients, $\omega_0 = 1/\hbar(E_f - E_i)$ and $E_f - E_i$ is the energy difference between the final and initial state of the absorption process. B_{if} can be obtained from the semiclassical radiation theory in the dipole approximation [68S]:

$$B_{if} = \frac{2\pi^2 e^2}{3\hbar m_e^* \omega_0} f_{if} \qquad (3.2),$$

where m_e^* is the electron effective mass and e is the charge of the electron. f_{if} is the transition oscillator strength given by

$$f_{if} = \frac{2m_e^* \omega_0}{\hbar} |\langle \psi_f | r | \psi_i \rangle|^2 \qquad (3.3),$$

where $|\psi_i\rangle$ and $|\psi_f\rangle$ are the initial and final states of the absorption transition and r is the position operator.

The oscillator strength f_{if} is a measure of the overlap between the wavefunctions of the initial and final states. It is a crucial parameter relating an observed absorption intensity in a sample to the number of centers causing the absorption. Unfortunately, for reasons explained earlier, our samples were not suited for absorption measurements. However there exist a different method to evaluate f_{if} using equation 3.1 and 3.2. From these relations, the spontaneous emission rate

$$A_{if} = \frac{2\omega_0^2 e^2}{3m_e^* c^3} f_{if} \qquad (3.4)$$

is the inverse of the radiative lifetime of the transition. Expressed in terms of more convenient quantities, the radiative lifetime can be written as

$$\tau_{rad} = \frac{4.5\lambda^2}{n\, f_{if}} \qquad (3.5),$$

where λ is the wavelength of the transition i → f in cm and n = 3.54 [90Sa] is the refractive index of GaAs. By performing time-resolved PL measurements it may therefore be possible to evaluate the oscillator strength.

Experimentally, the measurement of τ_{rad} is not always direct. The observed lifetime of a PL transition is given by

$$\frac{1}{\tau_{obs}} = \frac{1}{\tau_{rad}} + \frac{1}{\tau_{nonrad}} + \frac{1}{\tau_{others}} \qquad (3.6),$$

where τ_{nonrad} is the rate associated with non-radiative recombinations and τ_{others} represents other radiative channels that do not lead to an emission at $\hbar\omega_0$. τ_{nonrad} includes contributions from Auger recombinations which occur in BE systems that contain one (or more) additional charges. The BE recombination energy, instead of being transferred to a photon, is imparted to the remaining charge which get injected deep in the valence or conduction band, whereafter it thermalizes by emitting phonons. Osbourn and Smith [79O] calculated the Auger as well as the radiative lifetimes for single shallow acceptor in GaAs. For an effective mass acceptor, the Auger rate is about five orders of magnitude lower than the radiative rate and can thus be completely ignored. Y being a double acceptor, it may have a greater Auger rate than that reported for a single shallow acceptor. Nevertheless it is still expected to be much smaller than the radiative rate and will not be considered here. In indirect g p semiconductors however, the radiative lifetimes are typically much longer and Auger decay is usually found to dominate BE recombination processes [66N]. Other type of non-radiative processes may exist in semiconductors. We will consider an example of such a process in our analysis of the Y transient data.

Two-hole (or two-electron) processes represented by τ_{others} may

also reduce the observed lifetimes by depopulating the BE levels and emitting photons at lower energy than the energy monitored. This effect can be evaluated directly by comparing the principal BE transition intensities with that of the two-hole replica originating from the same levels. Fig. 3.1 reveals that, for Y_1 these secondary channels are comparatively weak and will thus be taken as negligible.

The customary method to measure lifetimes is to use above gap pulsed excitation and to observe decay curves by setting the spectrometer on the transition of interest. This situation gives rise to delayed creation of BE population since the generated free excitons first have to diffuse from where they are created and then get trapped at the binding centers. Also non-exponential decays are often observed due to slower alternate feeding channels, presumably in the form of detrapping from other exciton binding centers. These two effects lead to a more complicated decay curve, where a decay time and possibly more than one trapping time must be considered.

It is possible, however, to simplify luminescence decay measurements by resonantly exciting the transition for which the lifetime is sought and collecting the decay curve at the energy of one of its replica. Since the ratio of recombination probability of a principal transition over that of one of its replica is a constant determined by the respective oscillator strengths, the observed decay curves display a lifetime identical to that of the principal transition.

Decay curves obtained in that manner for BE transitions in sample B are displayed on a semi-log graph in Fig. 3.9. We show the decay curves of (a) $(A_C^0,X)^{2s}$, (b) Y_3, (c) Y_4 and (d) $(D^0,X)^{2p-}$ for pulsed excitation set on (A_C^0,X), Y_1, Y_1 and (D^0,X), respectively. The lines represent

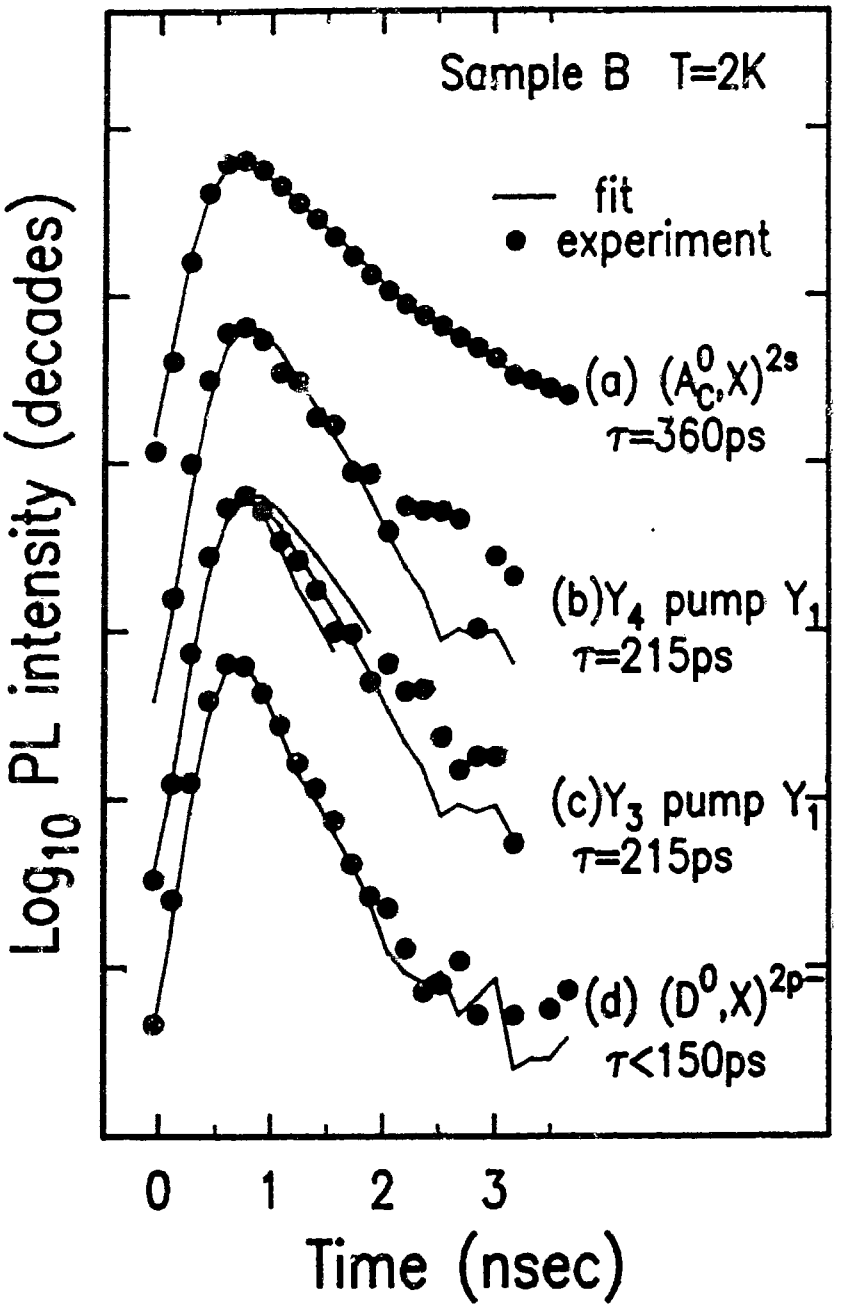

Figure 3.9

PL decay measurements of various replicas obtained with resonant excitation. In (a) the decay of $(A^0,X)^{2s}$ for pulsed excitation adjusted on (A^0,X) is fitted with a lifetime of 360 ± 20 ps. Both the decay of Y_3 (c) and Y_4 (b) for excitation on Y_1 are fitted with a decay constant of 215 ± 50 ps. The uncertainty for this lifetime is based on a visual comparison of the experimental data with decay curves for τ = 100 and 300 ps as displayed in curve (c). The lifetime of the $2p_-$ two-electron replica of (D^0,X) at 150 ps is an upper limit since it was found to be shorter than the value our deconvolution procedure allowed.

fits to the experimental results (dots). The fits are convolutions of the instrumental response curve determined experimentally with exponentially decaying functions parameterized by the fitting parameter τ. The instrumental response is measured by monitoring directly the decay of scattered laser light. In this experiment, the instrumental response displayed a decay curve nearly identical to that of Fig. 3.9(d). In principle, the deconvolution method enables the measure of lifetimes shorter than the instrumental response. When the measured lifetime is too short however, only an upper limit can be determined. This is the case in Fig. 3.9(d) where the decay of $(D^0,X)^{2p}$ was found to be very similar to the instrumental response of ~300 ps. In the sample studied, the lifetime of (D^0,X) is therefore determined to be less than 150 ps, this number representing the point after which the fit did not change appreciably. With resonant excitation on Y_1, the replicas Y_3 and Y_4 were found to decay with a similar lifetime of 215 ± 50 ps. The large uncertainty on this value arises from the noise in the measured decay curves. The margin of confidence was estimated by comparing the data with theoretical fits for 100 ps and 300 ps as shown in Fig. 3.9(c). (A^0,X) was found to decay more slowly, with a lifetime of 360 ± 20 ps.

The trend observed in the lifetimes as a function of exciton localization energy is in agreement with the predictions of Rashba and Gurgenishvili [62R,75R]. They reported that the radiative recombination rate of a bound exciton was proportional to the volume of the region occupied by its wavefunction, or equivalently, proportional to the localization energy to the power -3/2. This rule applied to acceptors can be understood qualitatively by using the following argument. As the

defect or impurity potential becomes increasingly more attractive to the holes, the hole wavefunctions get more localized and therefore the electron-hole overlap decreases along with the radiative transition rate. A similar argument holds for donors.

The three BE lifetimes measured in sample B are displayed on the bottom of Fig. 3.10 as a function of exciton localization energy to the power 3/2. The data was displayed in that manner to illustrate the general agreement with the theory of Rashba and Gurgenishvili. The lifetimes of the carbon acceptor BE as well as some of the KP acceptor measured in another MBE sample, called sample C, also appear on top of the figure. The lifetimes measured in sample C are consistent with the proposed power law. In our sample, however, BE lines seem to decay much faster than the trend observed for sample C. In particular the lifetime of the carbon acceptor bound exciton in our sample was only about a *third* of that observed in sample C. This consistent reduction in decay time for our sample can be connected with the previously mentioned hypothesis of BE "robbing" centers. According to equation 3.8, the observed lifetime of a BE system can be less than its true radiative lifetime if alternate deexcitation channels are present. We therefore suggest that the presence of centers which can de-excite shallow BE, eg: deeper centers to which the excitation may tunnel, contributes in reducing the lifetime of the observed transitions.

3.5 Proposed model

The model proposed to account for the properties of the Y-related

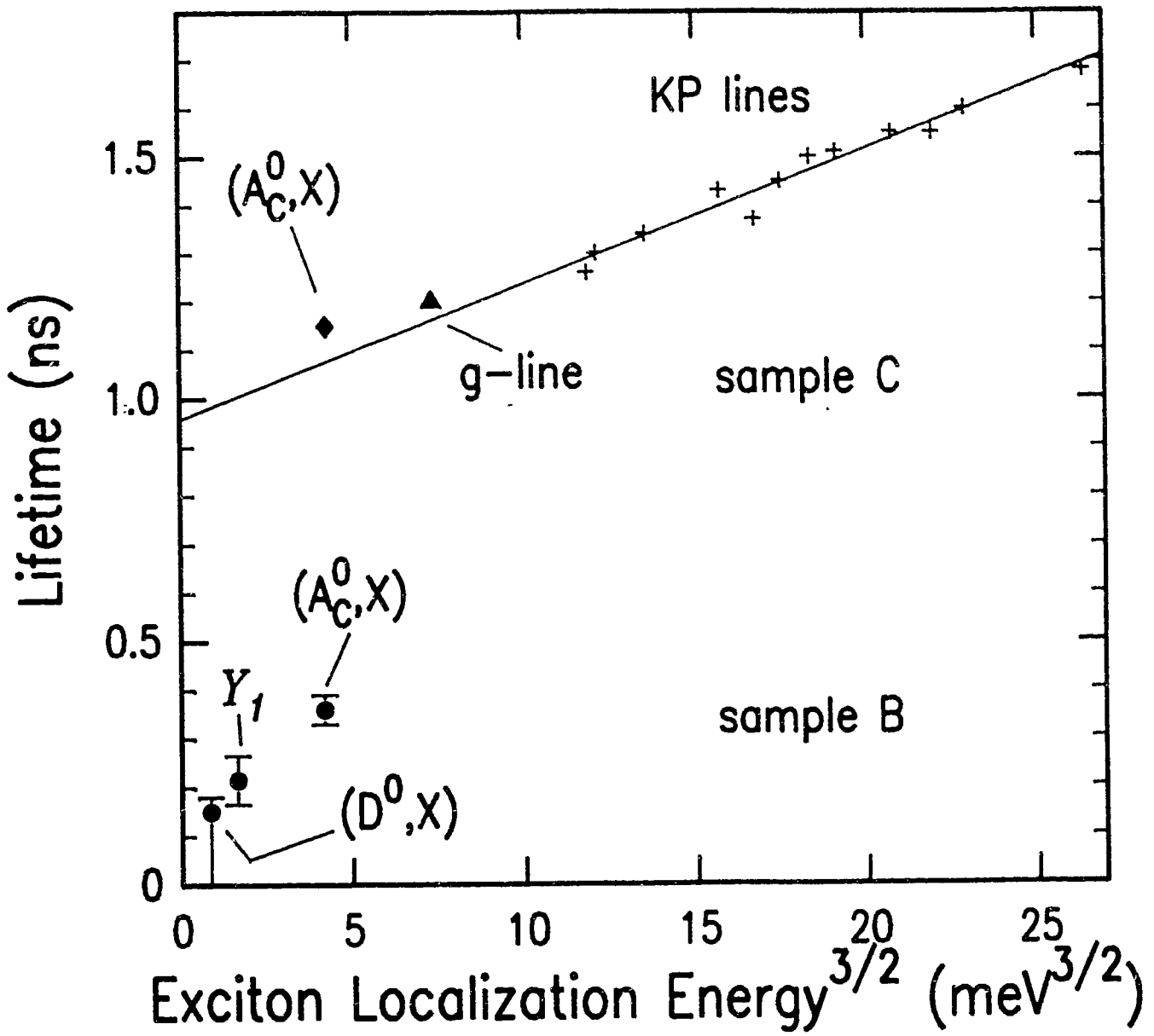

Figure 3.10

BE lifetimes versus localization energy to the power 3/2 for (A_C^0,X), (D^0,X) and Y_1 in sample B as well as for (A_C^0,X), the g-line and the KP-lines in sample C. The transitions in sample C appear on a straight line thus verifying the theory of Rashba and Gurgenishvili [62R, 75R]. The lifetimes observed in sample B, however, are consistently shorter than those in C. In this case it is suggested that the measured time constants include a non-radiative term due to capture from the BE onto deeper centers.

BE transitions observed so far is that of an axial double acceptor. It was shown that this model could explain 1) the presence of polarized PL emission, 2) the structure found in the two-hole replicas and 3) the overall energy spacing of the replica spectrum. In this section we will present further details of such a model, such as the structure of the BE initial state.

We present in Fig. 3.11 an energy diagram similar to the experimental transition diagram shown in Fig. 3.5, that includes interactions giving rise to the experimentally observed levels. Here again the two upper levels represent the two Y-BE states and the four lower levels represent the neutral Y double acceptor (only the 1s-1s set is shown).

According to the proposed model, the initial BE states of the Y PL transitions involve three holes and one electron. Group theory tells us that the antisymmetric subset of the coupled three hole states $\{\Gamma_8 \times \Gamma_8 \times \Gamma_8\} = \Gamma_8$ behaves like a single Γ_8 hole. This can be understood in terms of the filling of a fourfold $j = 3/2$ level. When three of the four available states are filled, two holes are paired off in the $m_j^h = \pm 3/2$ or the $m_j^h = \pm 1/2$ states and the system behaves like the remaining unpaired hole.

The degeneracy of a fourfold degenerate Γ_8 level can be reduced by the presence of a symmetry-reducing perturbation. For example, it is known that a perturbation along one of the [110] directions reduces the T_d symmetry to C_{2v} and lifts the degeneracy of the Γ_8 into a $m_j^h = \pm 1/2$ and a $m_j^h = \pm 3/2$ level. In group theory one writes: $\Gamma_8 \rightarrow 2\Gamma_5$ when $T_d \rightarrow C_{2v}$ [72R]. Group theory supplies no information about level ordering so the labels for the projection of three hole total angular

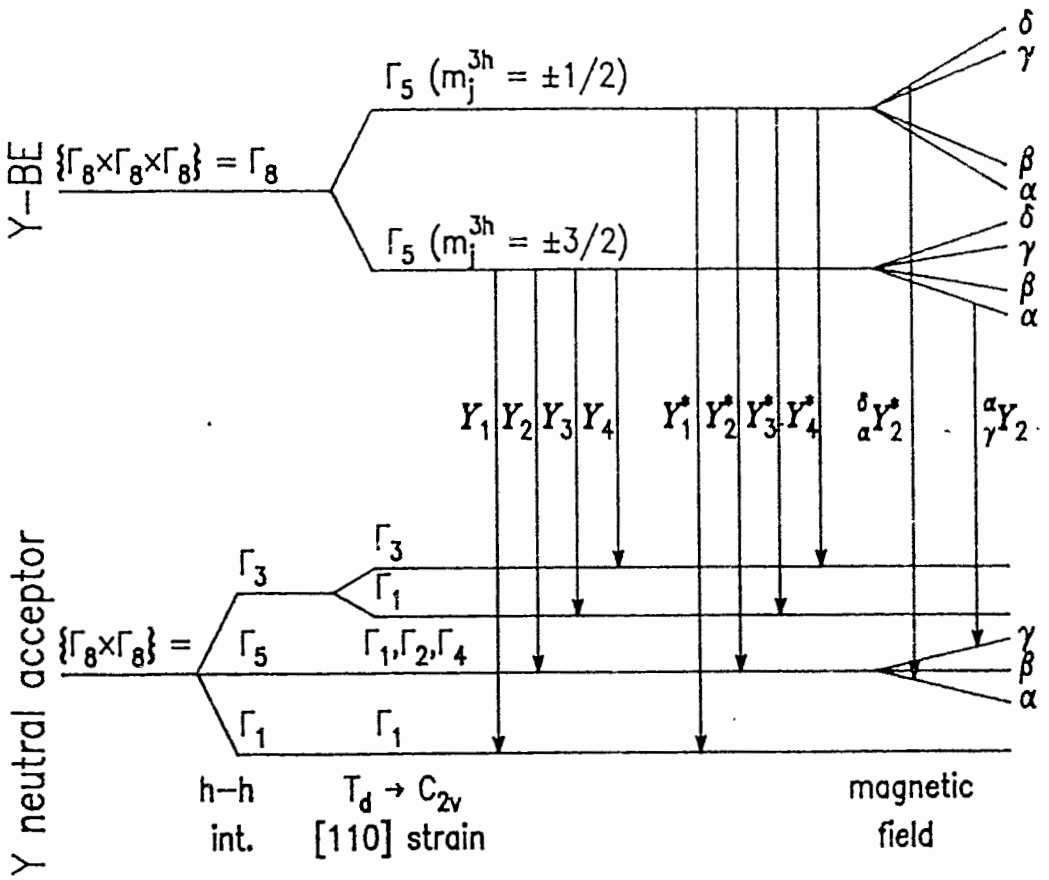

Figure 3.11

Energy level diagram for Y_1, Y_1^* as well as the Y-related 1s two-hole transitions. In zero magnetic field, the initial state containing 3 holes and 1 electron is split into two levels by the axial field of the defect. The electron-hole interaction is assumed to be negligible. The final state has four levels resulting from hole-hole interaction in the [110] axial defect field, with the first excited level accidentally triply degenerate to within our experimental resolution. A magnetic field can lift this non-essential degeneracy as well as the fourfold degeneracy of each of the two initial state levels. The labelling scheme for the transitions is indicated.

momentum m_j^{3h} in Fig. 3.11 are given assuming the presence of a compressive-type field. The effect of a compressive (tensile) force on the valence band brings the $m_j^h = \pm 3/2$ level below (above) the $m_j^h = \pm 1/2$ level [67B]. For three holes in a compressive-type field, the ground state corresponds to the $m_j^{3h} = \pm 3/2$ three-hole state with 2 holes paired off in the $m_j^h = \pm 1/2$ state and one in the $m_j^h = \pm 3/2$.

At this point, other choices of defect orientation are possible and no definite choice will be assumed. Theoretical derivations for defects along [111] and [001] also lead to two initial states. In fact, a defect along [111] could exhibit similar [110] and [$\bar{1}$10] polarization characteristics and thus cannot be ruled out on the grounds of polarization alone.

The model for the BE levels is completed by taking into account the remaining $j = 1/2$ electron. Here, as for the case of the single substitutional acceptor bound exciton, the electron-hole interaction is presumed too small to produce any further observable splitting. The degeneracy of the BE levels are then simply multiplied by two to account for electron spin without further changes to the level configuration. According to all the above considerations we have two fourfold degenerate (two possible hole values for m_j^{3h} and two possible electron values for m_j^e) initial levels available for BE transitions.

The final states of the Y-BE transitions, the neutral double acceptor states, show a great deal of similarity with the much studied single acceptor BE initial states. The (A^0,X) initial states contain 2 holes and one electron, but this electron is thought to have no detectable effect on the levels [87Sb]. The discussion on (A^0,X) in section 3.2 is therefore relevant for this work. As mentioned before,

the hole-hole interaction in the cubic field of the lattice leads to 3 antisymmetrized levels: Γ_1(non-degenerate), Γ_5(threefold degenerate) and Γ_3(twofold degenerate). The ordering shown in Fig. 3.11 is the reversed of that determined for (A^0,X) [87Sb]. The actual ordering depends on the detailed interactions of the two hole wavefunctions. It has been suggested [74M] that for shallow acceptors [72Wa, 74W] Γ_1 is placed a higher energy than Γ_5 and Γ_3, while for deeper centers this order is reversed. In the case of the KP double acceptors [88S] and of a double acceptor in GaSb [78N], Γ_1 has been assigned to lower energy than Γ_5 and Γ_3, as is also proposed here for the Y-defect. Some of these final state levels can split under the influence of the local axial field of the defect. In Fig. 3.11, the effect of a [110] axial field is illustrated [73K]: $\Gamma_3 \rightarrow \Gamma_1+\Gamma_3$, $\Gamma_5 \rightarrow \Gamma_1+\Gamma_2+\Gamma_4$ and $\Gamma_1 \rightarrow \Gamma_1$ when $T_d \rightarrow C_{2v}$. In order to agree with the observed four level structure, the splitting of $\Gamma_5(T_d)$ was assumed to be too small to be resolvable. Note also that the ordering of the $\Gamma_1(C_{2v})$ and $\Gamma_3(C_{2v})$ levels originating from $\Gamma_3(T_d)$ shown in Fig. 3.11 is an arbitrary choice. This level assignment will be referred to as scenario [110]a. Another assignment for a [110] axial defect which also yields four levels could have been made, namely the threefold $\Gamma_3(T_d)$ remaining unresolved and one of the three $\Gamma_5(T_d)$ states splitting off the two others (scenario [110]b). These two possible scenarios are schematically represented in Fig. 3.12 along with those related with other possibilities of defect orientations. The right hand side of each scenario illustrates the complete splitting of the levels assuming that an additional perturbation lifting all degeneracies is applied.

Since models with the three different defect orientations can

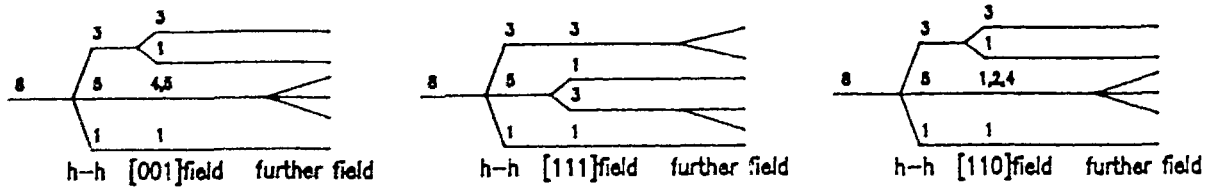

scenario [001]a scenario [111] scenario [110]a

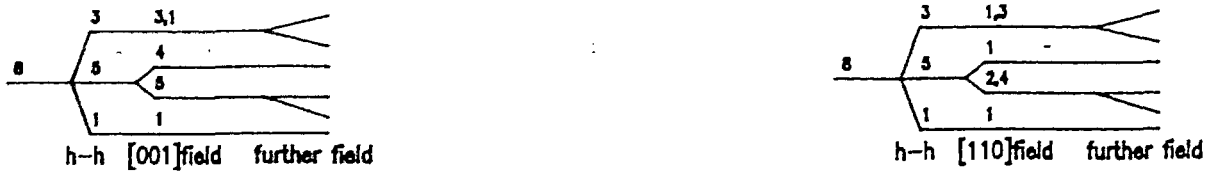

scenario [001]b scenario [110]b

[001] FIELD
$T_d \rightarrow D_{2d}$
$\Gamma_3 \rightarrow \Gamma_1 + \Gamma_3$
$\Gamma_5 \rightarrow \Gamma_4 + \Gamma_5$
$\Gamma_1 \rightarrow \Gamma_1$

[111] FIELD
$T_d \rightarrow C_{3v}$
$\Gamma_3 \rightarrow \Gamma_3$
$\Gamma_5 \rightarrow \Gamma_1 + \Gamma_3$
$\Gamma_1 \rightarrow \Gamma_1$

[110] FIELD
$T_d \rightarrow C_{2v}$
$\Gamma_3 \rightarrow \Gamma_1 + \Gamma_3$
$\Gamma_5 \rightarrow \Gamma_1 + \Gamma_2 + \Gamma_4$
$\Gamma_1 \rightarrow \Gamma_1$

Figure 3.12

Possible scenarios for the energy level diagram considering axial fields along the three main crystallographic directions. All scenario display four levels in zero magnetic field and six levels if all degeneracies are removed. Ordering of the levels is not considered here. The mapping of the representations under axial breaking of T_d symmetry is indicated at the bottom of the figure.

account for the four final levels as well as the two initial levels, we have to consider the set of data presented so far as insufficient for a complete determination of the defect geometry. Only orientation along [001] can be ruled out since it would have yielded no polarization difference for the [110] and [$\bar{1}$10] directions.

Regardless of the scenario chosen, the Y_1 and $Y_1^{\bullet}$ principal BE lines are assigned to transitions from the strain split BE initial levels to the $J = 0$ Γ_1 singlet state. Depending on the sign of the strain, Y_1 and $Y_1^{\bullet}$ each will be assigned to one of the two set of BE states, $m_j^{3h} = \pm 1/2$, $m_j^e = \pm 1/2$ or $m_j^{3h} = \pm 3/2$, $m_j^e = \pm 1/2$. We will leave the definite assignment of levels to particular transitions, until later, but will nevertheless calculate the polarization of levels. We will refer to the $m_j^{3h} = \pm 3/2$, $m_j^e = \pm 1/2$ BE states as $|g\rangle_l$ for $l = 1, 2, 3$ and 4 :

$$
\begin{array}{lll}
|g\rangle_l & |m_j^{3h}, m_j^e\rangle \text{ basis} & |J, M_J\rangle \text{ basis} \\
|g\rangle_1 & = |\tfrac{3}{2}, \tfrac{1}{2}\rangle & = |2, 2\rangle \\
|g\rangle_2 & = |\tfrac{3}{2}, -\tfrac{1}{2}\rangle & = \tfrac{1}{2}|2, 1\rangle + \tfrac{\sqrt{3}}{2}|1, 1\rangle \\
|g\rangle_3 & = |-\tfrac{3}{2}, \tfrac{1}{2}\rangle & = \tfrac{1}{2}|2, -1\rangle - \tfrac{\sqrt{3}}{2}|1, -1\rangle \\
|g\rangle_4 & = |-\tfrac{3}{2}, -\tfrac{1}{2}\rangle & = |2, -2\rangle
\end{array}
\qquad (3.7)
$$

and the $m_j^{3h} = \pm 1/2$, $m_j^e = \pm 1/2$ BE states as $|e\rangle_l$ for $l = 1, 2, 3$ and 4 :

$$
\begin{array}{lll}
|e\rangle_i & |m_j^{3h}, m_j^e\rangle \text{ basis} & |J, M_J\rangle \text{ basis} \\
|e\rangle_1 = |\tfrac{1}{2}, \tfrac{1}{2}\rangle & & = \frac{\sqrt{3}}{2}|2,1\rangle - \frac{1}{2}|1,1\rangle \\
|e\rangle_2 = |\tfrac{1}{2}, -\tfrac{1}{2}\rangle & & = \frac{1}{\sqrt{2}}\left[|2,0\rangle + |1,0\rangle\right] \\
|e\rangle_3 = |-\tfrac{1}{2}, \tfrac{1}{2}\rangle & & = \frac{1}{\sqrt{2}}\left[|2,0\rangle - |1,0\rangle\right] \\
|e\rangle_4 = |-\tfrac{1}{2}, -\tfrac{1}{2}\rangle & & = \frac{\sqrt{3}}{2}|2,-1\rangle + \frac{1}{2}|1,-1\rangle
\end{array}
\qquad (3.9)
$$

The $|g\rangle_i$ and $|e\rangle_i$ are expressed in terms of two different bases. The $|m_j^{3h}, m_j^e\rangle$ basis is the basis of individual projections of angular momentum for the three hole state and for the electron state. The $|J, M_J\rangle$ basis refers to J and M_J, the total angular momentum for the coupled system of electrons and holes and its projection on the axis of quantization. The coefficients used to expand the eigenvectors of the $|m_j^{3h}, m_j^e\rangle$ basis in terms of the $|J, M_J\rangle$ eigenvectors are the Clebsh-Gordan coefficients [73C]. For both bases the axis of quantization is the, as yet undetermined, axis of the defect. The $|J, M_J\rangle$ basis is most useful in calculating transition strengths. According to equation 3.3, the strength of a transition in the dipole approximation is given by

$$
f_{if}^m \sim |\langle \psi_f | r_m | \psi_i \rangle|^2 \qquad (3.9),
$$

where the index m refers to the circular components of the electric dipole operator e x r. r_m is equal to $1/\sqrt{2}(x-iy)$, z and $1/\sqrt{2}(x+iy)$ for m = -1, 0 and 1 respectively. According to the Wigner-Eckart theorem [73C], when $|\psi_i\rangle$ and $|\psi_f\rangle$ are expressed in the form $|J_i, M_{Ji}\rangle$ and $|J_f, M_{Jf}\rangle$ then

$$\langle \psi_f | r_m | \psi_i \rangle = (J_i 1\ M_{Ji} m \mid J_f M_{Jf})\ D(J_i, J_f) \qquad (3.10),$$

where $(j_2 j_3 m_2 m_3 | j_1 m_1)$ are the Clebsh-Gordan coefficients and $D(J_i, J_f)$ are factors independent of M_{Ji} and M_{Jf}. Using the relation 3.10 we can calculate the dipolar matrix element between the eight initial states and the Γ_1 final state for the three different operators. Z corresponds to transitions with the electric field polarized along the defect axis, which are referred to as π transitions. Transitions corresponding to $1/\sqrt{2}(x-iy)$ or $1/\sqrt{2}(x+iy)$ are circularly polarized in a plane perpendicular to the defect axis and are labelled σ. The non-zero matrix elements are :

$$\begin{aligned}
\langle 0,0|r_{-1}|g\rangle_2 &= \left(\frac{1}{\sqrt{3}}\right)\left(\frac{\sqrt{3}}{2}\right) \quad D(0,1) \\
\langle 0,0|r_{1}|g\rangle_3 &= \left(\frac{1}{\sqrt{3}}\right)\left(-\frac{\sqrt{3}}{2}\right) \quad D(0,1) \\
\langle 0,0|r_{-1}|e\rangle_1 &= \left(\frac{1}{\sqrt{3}}\right)\left(-\frac{1}{2}\right) \quad D(0,1) \\
\langle 0,0|r_{0}|e\rangle_2 &= \left(-\frac{1}{\sqrt{3}}\right)\left(\frac{1}{\sqrt{2}}\right) \quad D(0,1) \\
\langle 0,0|r_{0}|e\rangle_3 &= \left(-\frac{1}{\sqrt{3}}\right)\left(-\frac{1}{\sqrt{2}}\right) \quad D(0,1) \\
\langle 0,0|r_{1}|e\rangle_4 &= \left(\frac{1}{\sqrt{3}}\right)\left(\frac{1}{2}\right) \quad D(0,1)
\end{aligned} \qquad (3.11)$$

and are all proportional to D(0,1). In 3.11, the first brackets on the right hand side are the appropriate Clebsch-Gordan coefficients resulting from using equation 3.10.

The electric dipole operator expressed in the basis of its circular components (r_{-1}, r_0, r_1) is well suited for circular polarizations. In this work, however, we measured linearly polarized light, presumably

parallel and perpendicular to the defect axis. A change of basis to the linear components of the electric dipole operator e(x,y,z) is therefore required. Light polarized parallel to z is obtained using the r_0 circular component while for the perpendicular contribution, $x = 1/\sqrt{2}(r_1+r_{-1})$ is used. Using 3.11, we calculate the transitions from the $|g\rangle$ level to be 100% σ-polarized and the transitions from the $|e\rangle$ level to be partially polarized with a π to σ ratio of 4 to 1. According to these results, Y_1 could be a σ-transition originating from the $|g\rangle$ level for defect along [110] or a π-transition originating from the $|e\rangle$ level for defect along $[\bar{1}10]$. The predictions for the polarization of the transitions from the $|e\rangle$ and $|g\rangle$ levels being of opposite type, the polarization of Y_1^* is automatically accounted for with the remaining transitions. While both alternatives are possible, the first case seems to agree better with the observed degree of polarization for Y_1 and Y_1^*.

The information gained from the Y-related PL is explained by an axial double acceptor model. The orientation of the defect in the crystal, however, remains to be determined. In the next chapter, we will attempt to answer this question while verifying the claims made here.

CHAPTER 4

AXIAL DOUBLE ACCEPTOR PHOTOLUMINESCENCE IN A MAGNETIC FIELD

4.1 Introduction

As described in the previous chapter, the PL studies presented to this point do not allow us to draw any definite conclusions concerning the orientation of the defect in the lattice. One way of solving this problem is to study the PL emission while subjecting the sample to external perturbations. The role of these perturbations is to further reduce the symmetry of the environment in which the BE undergo the PL transitions, thus removing some symmetry-induced degeneracies. The lifting of degeneracies allows us to verify the hypotheses on level multiplicity which were made in section 3.5. Furthermore, quantitative models accounting for the perturbations can provide an even more rigorous verification of the nature of the levels involved. In the previously cited example of the acceptor bound exciton, clear progress was made by comparing the best fit to data obtained under uniaxial stress for the proposed models [87Sb]. The crystal field scenario was the favored model since it yielded a much better agreement to the data than the electron-hole interaction scheme.

In our study of the Y-defect, we perturbed the sample with an external magnetic field in order to find the defect orientation in the lattice. Zeeman spectroscopy (spectroscopy in the presence of a magnetic field) is easier to perform than piezospectroscopy (spectroscopy in the presence of mechanical stresses) since no special

sample preparation is required. The application of good uniaxial stress necessitates very carefully prepared samples, one for each stress direction chosen, whereas with Zeeman spectroscopy the same sample can be used for determining the effect of the field along the many crystal directions. In this study, this was done with the aid of the gear and wheel assembly described in Chapter 2. A further advantage of Zeeman spectroscopy is that it can split states which remain degenerate under arbitrary stresses, e.g. $|J,+M_J>$ and $|J,-M_J>$.

The magnetic field interacts with the magnetic moments of the electronic charges, namely the orbital angular momentum L and the spin S. In solid state physics one makes frequent use of the concept of "effective spin", $\tilde{S}$, which is a fictitious angular momentum such that the degeneracy of a group of levels associated with $\tilde{S}$ is set equal to $(2\tilde{S}+1)$. For example the fourfold degeneracy of the valence band extremum was attributed to the effective hole spin of 3/2. In that case, the effective spin was simply the total angular momentum resulting from adding vectorially the orbital momentum to the 1/2 spin. A Hamiltonian representing the Zeeman interaction can be written in the form

$$\mathcal{H}^{Zeeman} = \mu_B(\mathbf{H}\cdot\mathbf{g}\cdot\tilde{\mathbf{S}}) \qquad (4.1),$$

where μ_B is the electron Bohr magneton and H is the magnetic field. g multiplied by $-e/(2m_e^{\bullet}c)$ is the gyromagnetic ratio, the proportionality factor between the angular momentum of a system and its magnetic dipole moment. For an atom in vacuum, g is a scalar quantity. For electrons in solids, on the other hand, g has to be considered as a tensor since

such media lack full rotational symmetry. This takes into account the fact that even for a point defect, the Zeeman interaction may depend on the angle that **H** makes with the crystal axes.

For convenience, the effect of the magnetic field on a transition can be separated in two parts, the Zeeman splitting and a shift of the lines [76S]. The Zeeman effect only considers the interaction of the the magnetic field with the angular momenta of the charges involved. It is responsible, for instance, for the energy separation between 1/2 and -1/2 spin states in a magnetic field. For a BE transition, the shift is due to the shifting of the band edges, as well as the diamagnetic shift of the BE itself. In this work, all shifts were ignored by aligning the energy scales of the spectra to clearly show the Zeeman splitting.

In this chapter, the results of the Y-related BE transitions in the presence of a magnetic field are presented. First the spectra collected with non-resonant excitation will be shown and compared to theoretical fits. Next the Hamiltonian used to generate these fits will be presented. Finally we will show the results obtained with resonant excitation.

4.2 Transitions with non-resonant excitation

The effect of a magnetic field on the principal transition Y_1 has been measured in this work. The paramagnetic effects for **B** applied parallel to [001] in sample A are illustrated in Fig. 4.1. PL spectra obtained using above band gap excitation at 5 different fields for the sample A are shifted in order to align the center of the split multiline

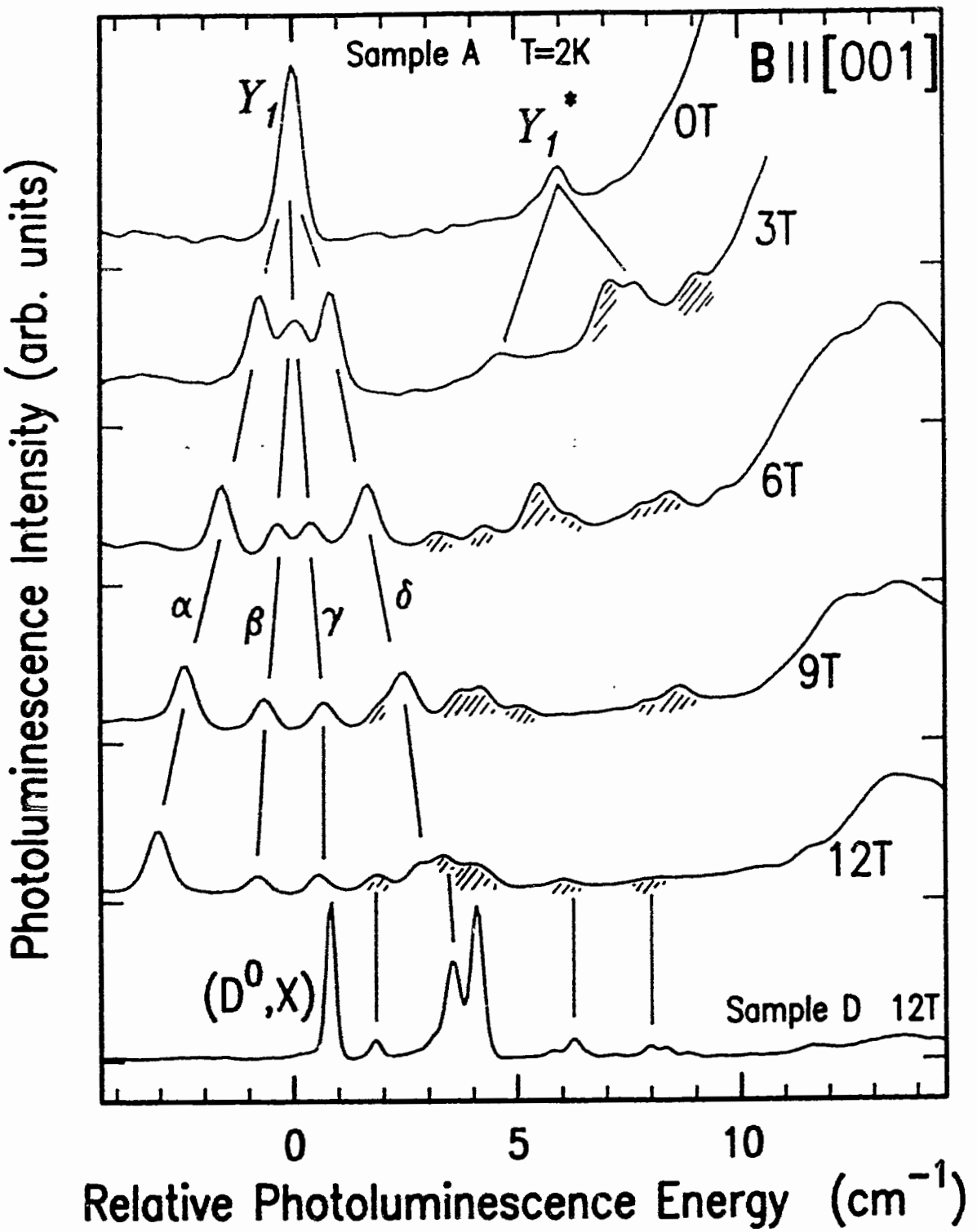

Figure 4.1

PL spectra at five different fields applied parallel to B ‖ [001] for sample A and at 12 T for sample D (bottom). Sample D does not contain the Y defect but is shown here as a reference for (D^0,X) transitions. The (D^0,X) are shaded in the spectra of sample A. Y_1 is seen to split into four components while the behavior of Y_1^* is more uncertain.

Y_1 structure. The shifts used are 6.2 cm^{-1} for 3 T, 19.0 cm^{-1} for 6 T, 34.5 cm^{-1} for 9 T and 51.3 cm^{-1} for 12 T. The actual spectral energies of the highest Y_1 component ($^{\delta}Y_1$) as a function of magnetic field are reported in Table 4.1.

The spectrum at the bottom of the figure was collected at 12 T for sample D. Sample D does not contain the Y defect; it is a very high-purity epilayer grown by MOCVD. All the important features seen on this last spectrum are associated with donor BE and serve as a reference in order to identify (D^0,X) related transitions in the 12 T spectrum from sample A. At the other fields, the spectral features that could be identified as (D^0,X) transitions were also shaded in. Surprisingly, an enhancement of the (D^0,X) features was observed with increasing magnetic field. At zero field, (D^0,X) features were not resolved above the noise level. At 6 T, however, their total integrated intensity was comparable to that of Y_1. Another intriguing observation is the relative intensities of the different Zeeman split (D^0,X) features in our sample as compared to those observed in the MOCVD sample. In particular, it is not clear why the strong lowest energy (D^0,X) feature of the last spectrum is not seen in the Y sample.

The Y_1 line is seen to split into four components $^{\alpha}Y_1$, $^{\beta}Y_1$, $^{\gamma}Y_1$ and $^{\delta}Y_1$, as predicted by the model constructed in chapter 3. We used additional Greek symbols on the left hand side of the Y labels to distinguish between the various magnetic field split states. Superscripts pertain to initial states while subscripts pertain to final states (subscripts are needed for the Y_2 transitions only). Signs of thermalization between the various Y_1 components were only visible at the highest field where the weak $^{\delta}Y_1$ transition is seen to be much

Table 4.1 Spectral positions of a few important Y-related BE transitions for two field orientations. The spectral positions of most Y-related BE transitions as a function of magnetic field can be derived using the information presented here plus that extracted from Figs. 4.2, 4.3, 4.6 and 4.8.

Magnetic field (Tesla)	B ∥ [001]	B ∥ [$\bar{1}$10]	
	δ_{Y_1} (cm^{-1})	δ_{Y_1} (cm^{-1})	$\delta_{Y_1^{2s}}$ (cm^{-1})†
0	12209.6	12209.6	12059.5
1	12210.5	12210.4	12060.2
2	12213.0	12212.4	12062.5
3	12216.4	12216.1	- -
4	12220.5	12219.9	12069.7
5	12225.0	12224.2	- -
6	12230.0	12228.9	12079.0
7	12235.3	12233.9	12083.8
8	12240.8	12239.2	12089.4
9	12246.4	12244.6	12094.9
10	12252.1	12250.2	12100.8
11	12257.8	12256.2	- -
12	12263.5	12261.7	12112.7

†The "- -" indicates transitions that were not observed in this work.

smaller than $^{\alpha}Y_1$.

The splitting of Y_1^* is much more difficult to discern than that of Y_1. Only at low field is it possible to find spectral features above the Y_1 quadruplet that are not due to (D^0,X) transitions. Also, only two out of the four predicted lines are seen at 3 T. We suggest that the other two peaks are too weak to be detected. In the next section, we will present a series of PL measurements leading to the detection of all four Y_1^* transitions.

The enhancement of the donor related transitions associated with the magnetic field as seen on the spectrum sequence of Fig. 4.1 is a surprising feature. It is possible, however, to understand this effect by referring to our previously cited hypothesis on the mechanism for the quenching of the donor related BE features at zero field. It is conceivable that the spatial compression of the electronic wavefunctions by the magnetic field acts in such a way as to reduce the quenching effect of the exciton "robbing" centers. This reduction would again be more noticeable for the donor related features because of their extended wavefunctions. Alternatively, the magnetic field may remove an accidental degeneracy between a (D^0,X) state and a state of the competing center which enhances tunneling from (D^0,X) at zero field.

A plot of the splitting of the Y_1 lines as a function of magnetic field for B ∥ [001] in sample A is presented in Fig. 4.2. The shift of the quadruplet center of mass was also removed to make the splitting of the states as a function of field more transparent. A least-square fitting procedure was applied to the spectral data below 4 T to extract the positions of the overlapping peaks.

On the basis of the Zeeman behaviour, we concluded that the line

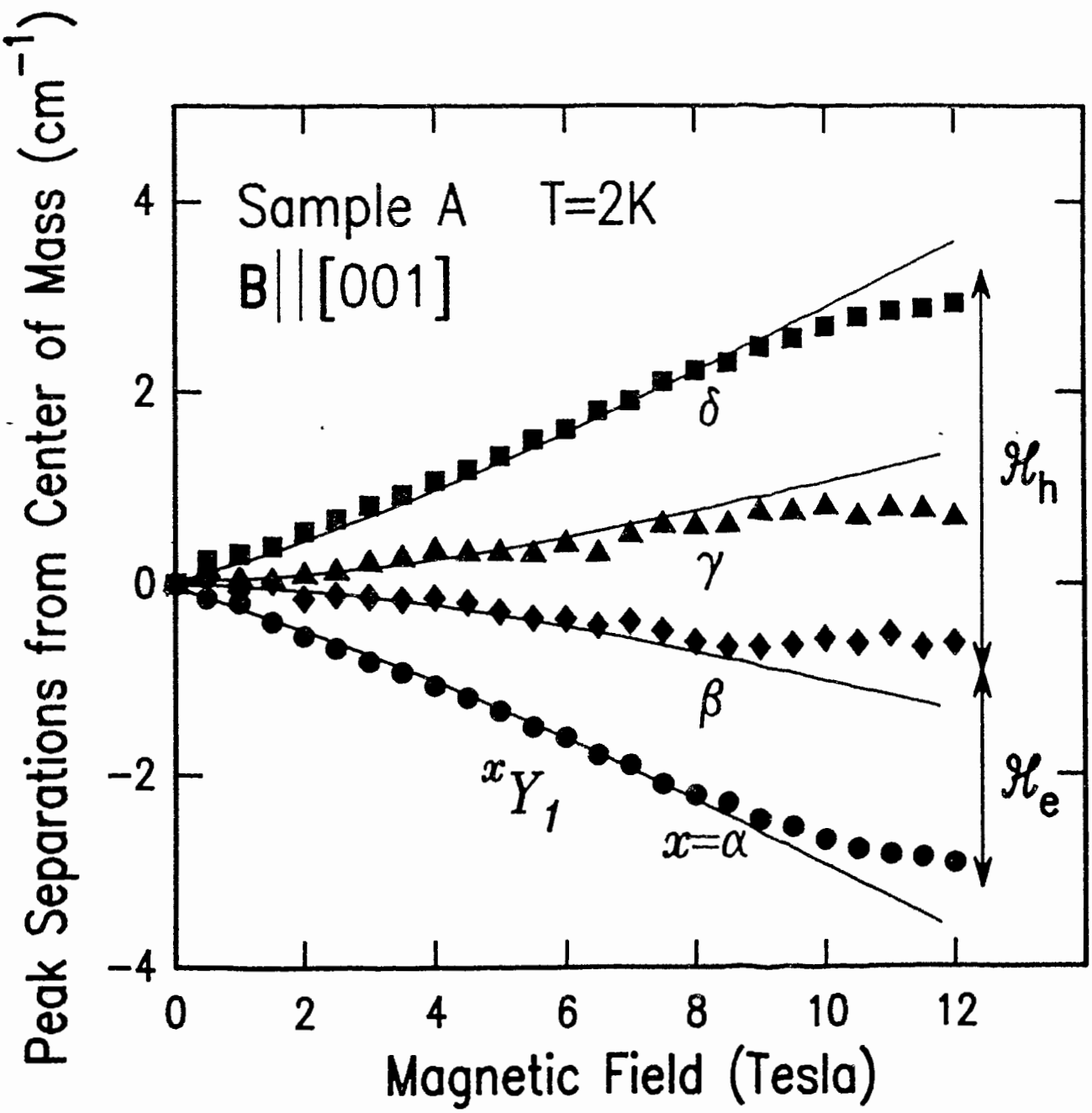

Figure 4.2

Zeeman splitting pattern of the principal BE transition Y_1, for B parallel to [001]. The peak positions of the lines are measured relative to their center of mass. The solid lines represent a fit to the data as presented later in the text. The Zeeman splittings due to the hole and those to the electron are indicated by the labels $\mathcal{H}_h$ and $\mathcal{H}_e$, respectively.

seen at 12210.0 cm^{-1} in VPE GaAs [80R] corresponds to a different defect than that responsible for Y_1 and Y_1^*. Indeed, according to the authors of reference 80R, line "F" was seen to split into five components with a larger splitting than that observed for Y_1 for any field orientation.

As previously proposed, the initial ground state of the transition is composed of a doubly degenerate coupled hole state ($m_j^{3h} = \pm 3/2$) and of a doubly degenerate electron state ($m_j^e = \pm 1/2$). The effect of the magnetic field is to lift this fourfold degeneracy. Experimentally, we observed the emergence of a pair of doublets: ${}^{\alpha}Y_1 - {}^{\beta}Y_1$ and ${}^{\delta}Y_1 - {}^{\gamma}Y_1$. The separation of the doublets is attributed to the $m_j^{3h} = \pm 3/2$ hole splitting and the separation within a doublet is due to the electron splitting as indicated by the labels $\mathcal{H}_h$ and $\mathcal{H}_e$ in Fig. 4.2. Since the electron was suggested to be decoupled from the holes, we used a Hamiltonian with separate contributions for the electron and holes of the form:

$$\mathcal{H} = \mathcal{H}_e + \mathcal{H}_h \qquad (4.2).$$

Also, because the Γ_6 conduction band in GaAs displays a nearly spherical and nearly parabolic dependence on **k**, equation 4.1 for electrons reduces to:

$$\mathcal{H}_e = \mu_B g_e \mathbf{H}\cdot\mathbf{S} \qquad (4.3),$$

where g_e, the electron g value, is considered as a scalar quantity. The lines displayed in Fig. 4.2 correspond to a theoretical fit based on equation 4.2 and will be presented later in this section. Experimentally, $\mathcal{H}_e$ is a linear function of magnetic field yielding a

electron g value of -0.405 ± 0.04 which is in excellent agreement with reported values [91B]. Furthermore, $\mathcal{H}_e$ is independent of crystal orientation in the magnetic field as predicted from equation 4.3.

On the other hand, $\mathcal{H}_h$ exhibits significant non-linearity and anisotropy. This is clearly visible in Fig. 4.3 where the Y_1 quadruplet detected in sample A is plotted as a function of crystal orientation with respect to a magnetic field of 5 T for rotations in two planes. The lines in this figure are only to guide the eye. The value of 5 T was chosen in order to maximize the observed splitting while still avoiding spectral interference from (D^0,X) features as is the case at higher fields (see Fig. 4.1). In both the cases of a rotation in (a) the (110) plane and (b) the (001) plane, we observed variations in the separation of the doublets but no or negligible variation within a doublet. This confirms our assignment of the inter-doublet separation to hole Zeeman interaction and intra-doublet separation to electron Zeeman splitting.

The orientational dependence of the hole energy can have two distinct origins. First, as mentioned in chapter 1, the valence band is anisotropic and the Zeeman interaction of a hole depends on the orientation of the field with the crystal axes. This effect has been reported for the Sn substitutional acceptor in GaAs by White *et al.* [72Wb] and is relatively small. These authors measured anisotropies of about 0.25 cm^{-1} and 0.5 cm^{-1} for the $m_j = \pm 3/2$ and for the $m_j = \pm 1/2$ hole splittings at 3.4 T, respectively. In Fig. 4.3, the Zeeman anisotropies are observed to be larger than these reported values and an additional effect must be considered. The additional variation in the Zeeman split Y_1 transition energies arises from the extra anisotropy in the hole

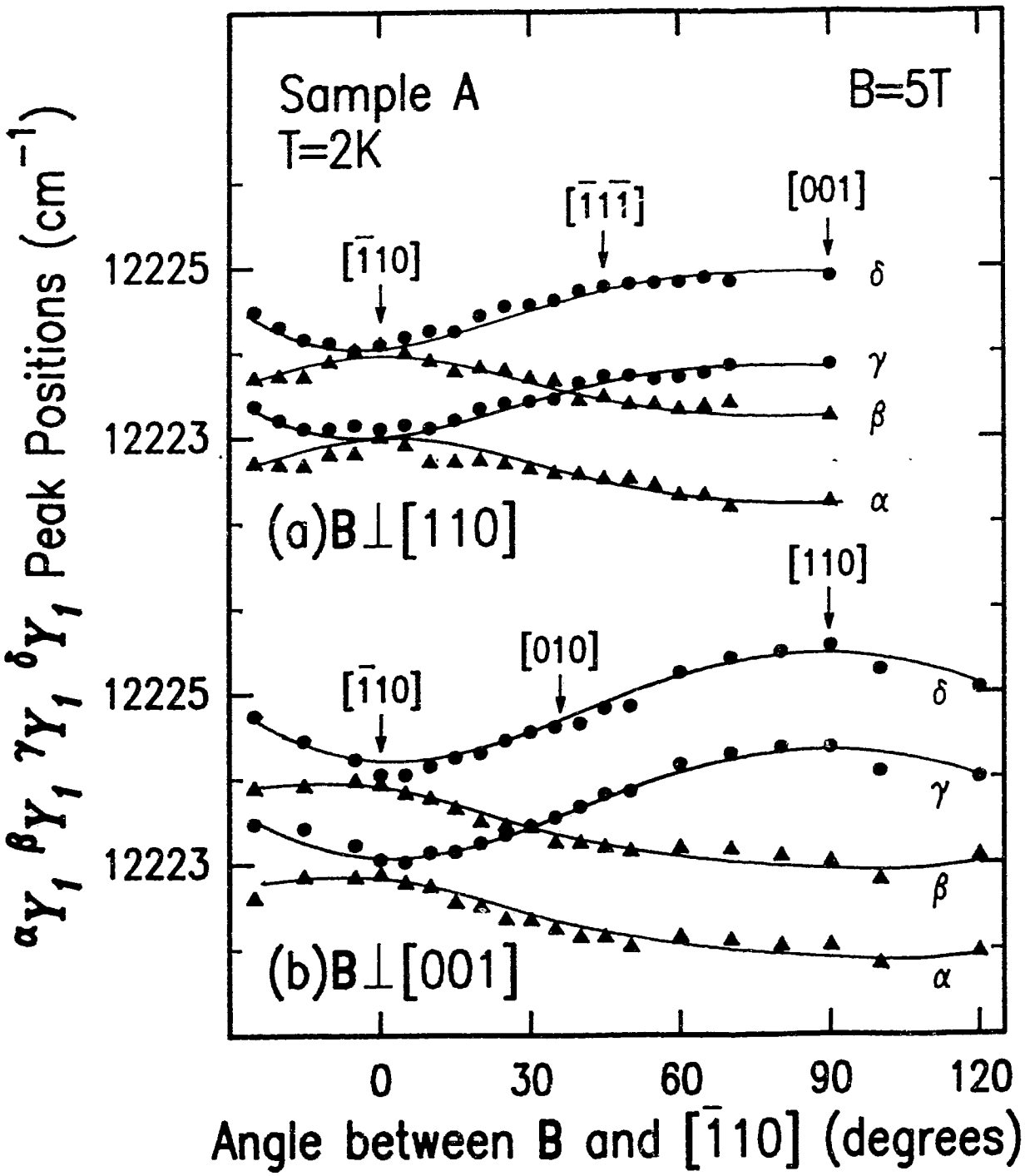

Figure 4.3

Spectral positions of the magnetic field split Y_1 quadruplet as a function of orientation of the sample in a field of 5 T. In (a) the field is rotated in the (110) plane while in (b) it is rotated in the (001) plane. Arrows indicate positions where the field is oriented along specific crystallographic directions as indicated. In this figure the lines are only to guide the eye.

wavefunctions induced by the defect axial field. This contribution is best illustrated by an example. Consider, for instance, three p orbitals fixed on a XYZ axis system, with Z as the quantization axis. In our case, the Z axis would be imposed by the defect axis. When Z is parallel to the field, the energy difference between the $|1,1\rangle$ and $|1,-1\rangle$ orbitals (in the $|1,m_l\rangle$ basis) is maximum. Rotating the z axis of the system away from the magnetic field causes a decrease in energy separation [70A]. For the Y defect, this kind of orientational anisotropy will be assumed to dominate over the contributions from the valence band.

The anisotropies observed in Fig. 4.3 therefore present strong indication of defect orientation in the crystal. The variation of the hole splitting as a function of orientation of the field in the plane (001), shown in Fig. 4.3(b), confirms the direction [110] as the most likely candidate for the defect orientation. First, we note that the inflexion points of the anisotropy pattern is aligned with the $[\bar{1}10]$-[110] reference points rather than with the [010]-[100] set. This provides further evidence for the rejection of the [001] scenario. The maximum hole splitting was reached with the magnetic field aligned with [110], indicating the axis of quantization. A rotation of the field in the (110) plane includes alignment of **B** with $[\bar{1}11]$ and $[\bar{1}1\bar{1}]$. In Fig. 4.3(a) it was verified that the inflexion points of the anisotropy pattern did not coincide with these reference points either. Anisotropy of the Y_1 quadruplet for magnetic fields perpendicular to $[\bar{1}10]$ (not shown) also verified that the other [111] directions did not correspond to the quantization axis. These results represent the strongest evidence presented so far in favor of the [110]-defect scenario.

Further support for this theory will be presented with the aid of a spin Hamiltonian.

The splittings of Y_1 as a function of magnetic field for fields parallel to $[\bar{1}10]$ and [110] were also collected but are not shown here. These results were similar to those shown in Fig. 4.1 and Fig. 4.2 but the hole splitting was larger in the case of $\mathbf{B} \parallel [110]$ and much less in the case of $\mathbf{B} \parallel [\bar{1}10]$, in agreement with the results for B=5 T in Fig. 4.3. In all cases the separation attributed to $\mathcal{H}_e$ was linear and that attributed to $\mathcal{H}_h$ was roughly linear (although with different proportionality constants for different orientation) for fields up to about 8 T after which the rate of the $\mathcal{H}_h$ splitting was somewhat reduced.

The $m_J^{3h} = \pm 3/2$ hole splitting plotted as a function of crystal orientation with respect to a magnetic field of 5 T in sample A is presented in Fig. 4.4. Each data point represents the average of the peak separations $\delta Y_1 - \beta Y_1$ and $\gamma Y_1 - \alpha Y_1$. The solid lines were obtained using the same fitting procedure as utilized in Fig. 4.2. The Hamiltonian used to model the J = 3/2 hole splitting is

$$\mathcal{H}_h = \mu_B (\mathbf{H} \cdot \mathbf{g}_h \cdot \mathbf{J}) + D \left[J_z^2 - \frac{J}{3}(J+1)\right] + E (J_x^2 - J_y^2) \qquad (4.4),$$

where $\mathbf{g}_h$ is the hole g tensor and J = 3/2. D and E are the axial and orthorhombic local crystal field parameters [70A, appendix], and J_x, J_y and J_z the projections of the hole angular momentum on the $[\bar{1}10]$, [001] and [110] crystallographic directions, respectively. The detailed derivation of relation 4.4 is presented in the appendix at the end of this thesis.

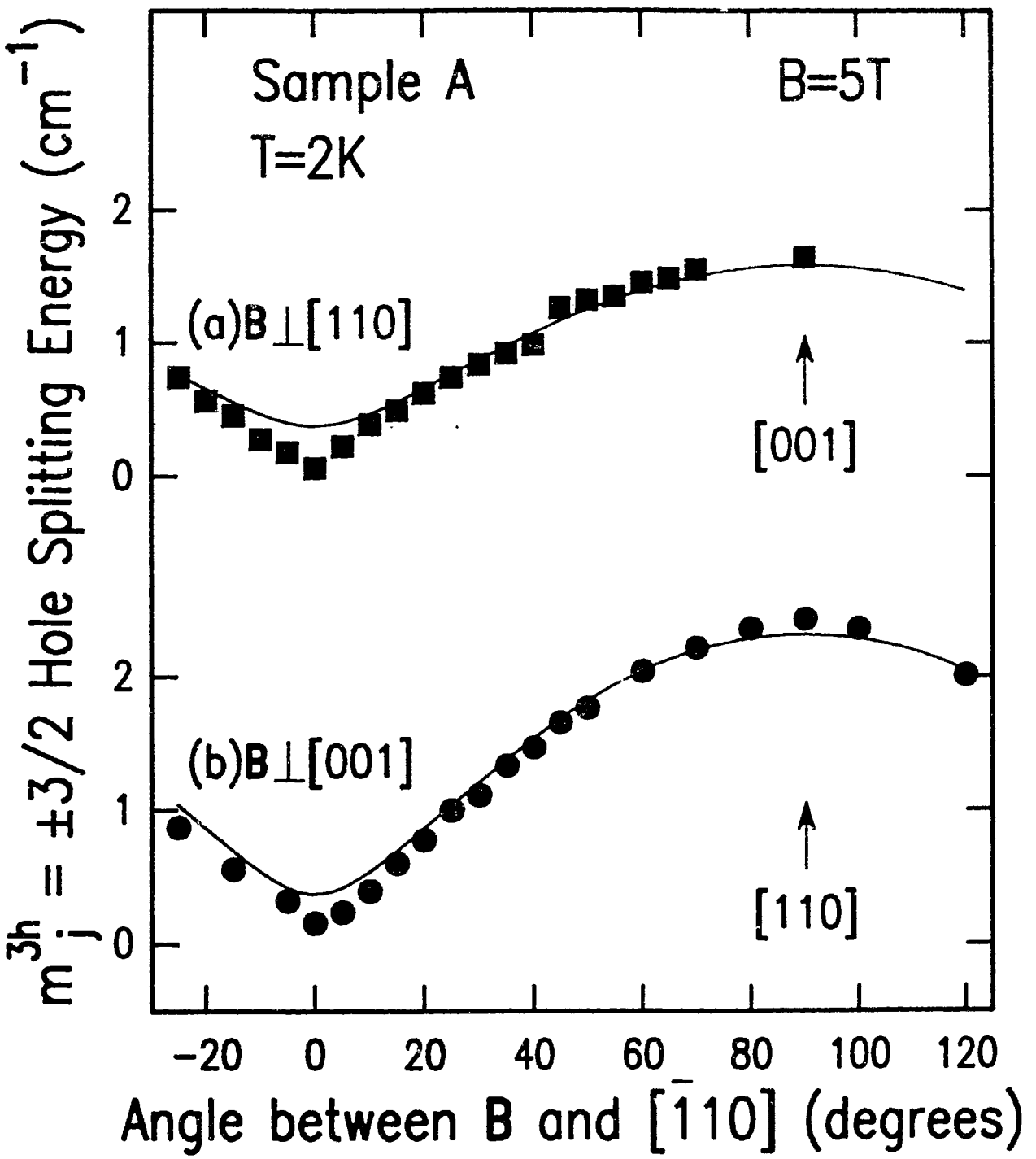

Figure 4.4

Anisotropies of the the $m_j^{3h} = \pm 3/2$ hole Zeeman splitting for rotations of a 5 Tesla magnetic field (a) in the (110) plane and (b) in the (001) plane. The data are derived from observed Zeeman anisotropy of the Y_1-quadruplet as displayed in Fig. 4.3. Solid lines represent the same fit as in Fig. 4.2. The maximum $m_j^{3h} = + 3/2$ to $m_j^{3h} = - 3/2$ separation at B ∥ [110] indicates the axis of quantization of the defect.

The first and second terms of the right hand side of equation 4.4 are invariant under rotation about the Z axis. The third term, on the other hand, represents the orthorhombicity of the center and does not have this axial symmetry. For a defect with perfect axial symmetry, E is equal to zero. In the case of the Y-defect however, we have to assume that E is finite because of the observed anisotropy of $\mathcal{H}_h$ for B in the (110) plane (Fig. 4.4(a)). Had Y been perfectly axial , the $m_j^{3h} = \pm 3/2$ hole splitting would then have been independent of field orientation as long as **B** is perpendicular to [110], the suggested defect axis. We propose that the anisotropy seen in this plane to be due to the orthorhombicity of the Y-defect.

As mentioned earlier, the anisotropy of the valence band is not taken into consideration in equation 4.4.

As is the case for centers whose symmetry is not too low, there exists a basis XYZ in terms of which the 3x3 matrix g_h is diagonal [70A]. This basis is chosen here by assuming "quasi-axiality" along [110]. Accordingly, we get [110] for Z, $[\bar{1}10]$ for X and [001] for Y. Of the three resulting diagonal matrix elements, we assume two (g_x and g_y) to be equal to conform with our hypothesis of near axiality. The two independent hole g-values are renamed $g_{\parallel}$ and $g_{\perp}$. $g_{\parallel}$ refers to the direction along the defect axis and $g_{\perp}$ to that perpendicular to it. In addition to these simplifications, the two crystal field parameters were not taken to be independent. In zero magnetic field, the separation between the $m_j^{3h} = \pm 1/2$ and $m_j^{3h} = \pm 3/2$ state is exactly given by $2(D^2+3E^2)^{1/2}$ [appendix,70A]. Using the experimentally determined Y_1-$Y_1^{\bullet}$ separation, E was therefore set equal to $\pm(3.0-D^2/3)^{1/2}$.

The model was fitted simultaneously to four sets of data using a

least square fitting procedure by allowing the three free parameters $g_{\parallel}, g_{\perp}$ and D to vary. The four data sets consisted of i) the magnitude of $m_j^{3h} = \pm 3/2$ hole splitting for B ∥ [001] as a function of field as seen in Fig. 4.2, ii) and iii) the anisotropy in the [110] and [001] planes of the $m_j^{3h} = \pm 3/2$ hole splitting at 5 T as seen in Fig. 4.4(a) and (b) and iv) the $m_j^{3h} = \pm 1/2$ hole splitting at 3.5 T for B ∥ [001]. This last experimental result is presented in the next section.

The best fit to the data was obtained for $D = 2.9 \pm 0.1$ cm^{-1}, $E = -0.44 \pm 0.1$ cm^{-1}, $g_{\parallel} = 0.34 \pm 0.04$ and $g_{\perp} = 1.1 \pm 0.2$. Attempts to fit the data by choosing the defect axis along directions other than [110] resulted in unacceptable errors or unphysical parameters, confirming [110] as the defect axis. The high D/E ratio indicates that the defect is nearly, but not perfectly axial in agreement with our assumptions. The obtained average hole g value $(g_{\parallel}+2g_{\perp})/3 = 0.85 \pm 0.1$ is comparable to that found for other acceptors in GaAs (0.60 for C and 0.78 for Sn [82L]) and that reported for the KP lines (0.5 for KP line 14 [88S]).

In this section, we inferred the Y-defect orientation from the splitting of the Y_1 principal BE transition in the presence of a magnetic field. The information presented indicates that the defect is incorporated preferentially along the [110] direction in agreement with our initial hypothesis drawn from zero field data. In the next section, we will introduce resonantly excited Zeeman PL results to test the model even further.

4.3 Transitions with resonant excitation

The fourfold structure of the Y_1 principal BE transition under magnetic field with non resonant excitation presented in section 4.2 was attributed to splitting in the initial BE state. The final state of Y_1, the ground state of the neutral double acceptor, was said to be non-degenerate in zero magnetic field, in agreement with the model put forward.

One or two of the remaining final state levels of the 1s-1s neutral acceptor were proposed in chapter 3 to be degenerate. The principal objective of the measurements presented in this section is to clarify this issue.

The effect of the magnetic field on the 1s replicas of Y_1 in sample A is illustrated in Fig. 4.5. These experiments were conducted with $\mathbf{B} \parallel [\bar{1}10]$ although measurements done with $\mathbf{B} \parallel [001]$ (not shown) yielded qualitatively similar results. As seen in the figures presented earlier in section 4.2, in the presence of a magnetic field, there are four distinct Y_1 lines which can be resonantly excited. The inset of Fig. 4.6 shows the spectra collected from the same sample at 3 T for resonant excitation of ${}^{\delta}Y_1$ and ${}^{\alpha}Y_1$. The spectra look very similar, the upper one being simply shifted with respect to the other by the ${}^{\delta}Y_1$-${}^{\alpha}Y_1$ separation. This indicates that one of the transitions, say ${}^{\delta}Y_4$, and the corresponding displaced transition, ${}^{\alpha}Y_4$, only differ in the initial state. Within the Y_1 quadruplet, no lower energy initial state is populated by pumping a higher energy state. This was verified for fields up to 8 T, where relaxation to lower initial states started to occur. Consequently, below 8 T, the mapping of the 1s replicas as a

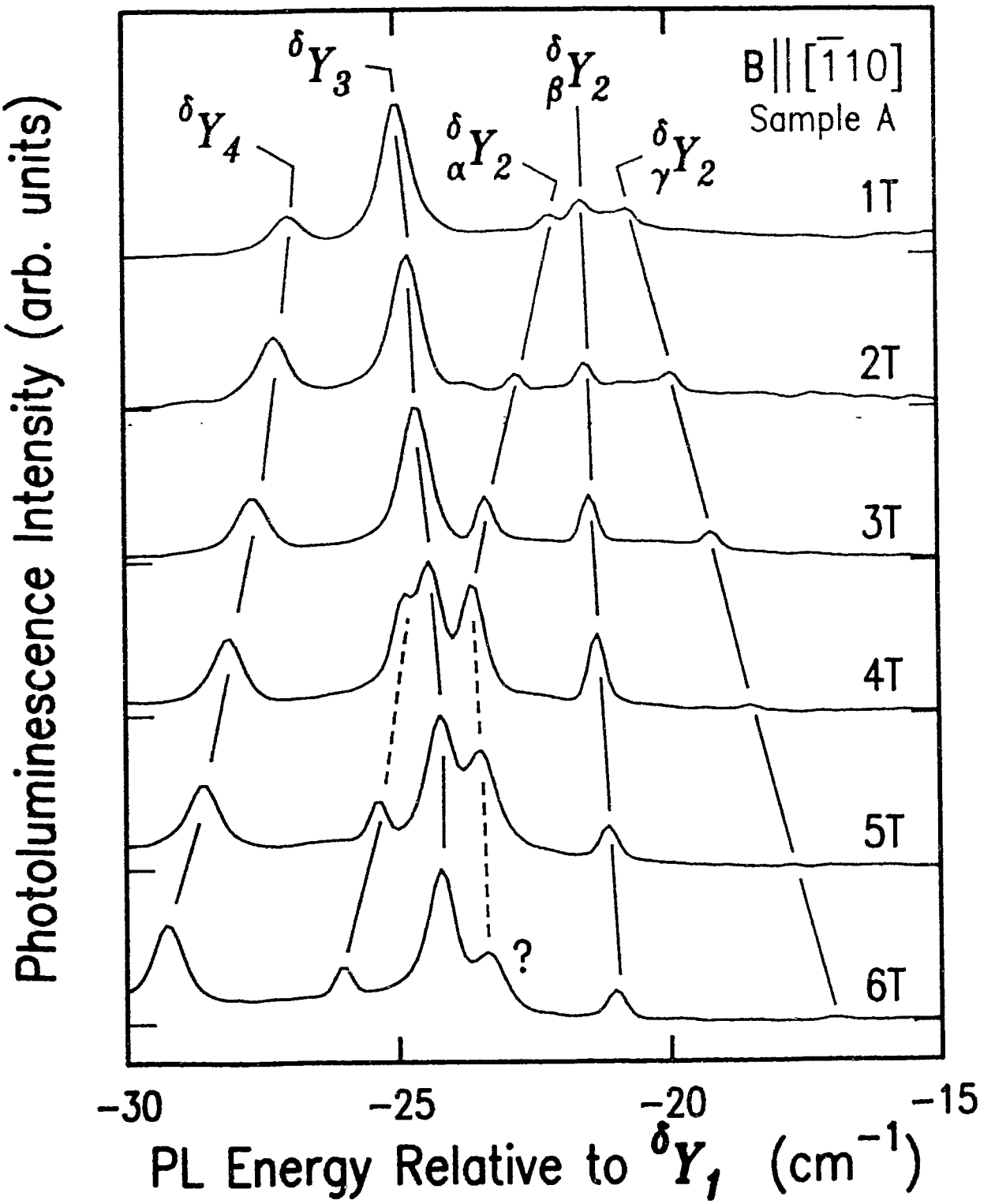

Figure 4.5

PL spectra resonantly excited at the $^{\delta}Y_1$ transitions for field going from 1 to 6 T in steps of 1 T. The spectra are referenced to $^{\delta}Y_1$, or laser excitation. $^{\delta}Y_4$ and $^{\delta}Y_3$ fan out while $^{\delta}Y_2$ splits into three components. An anomalous peak (?) is seen from 4 T to 6 T (see text).

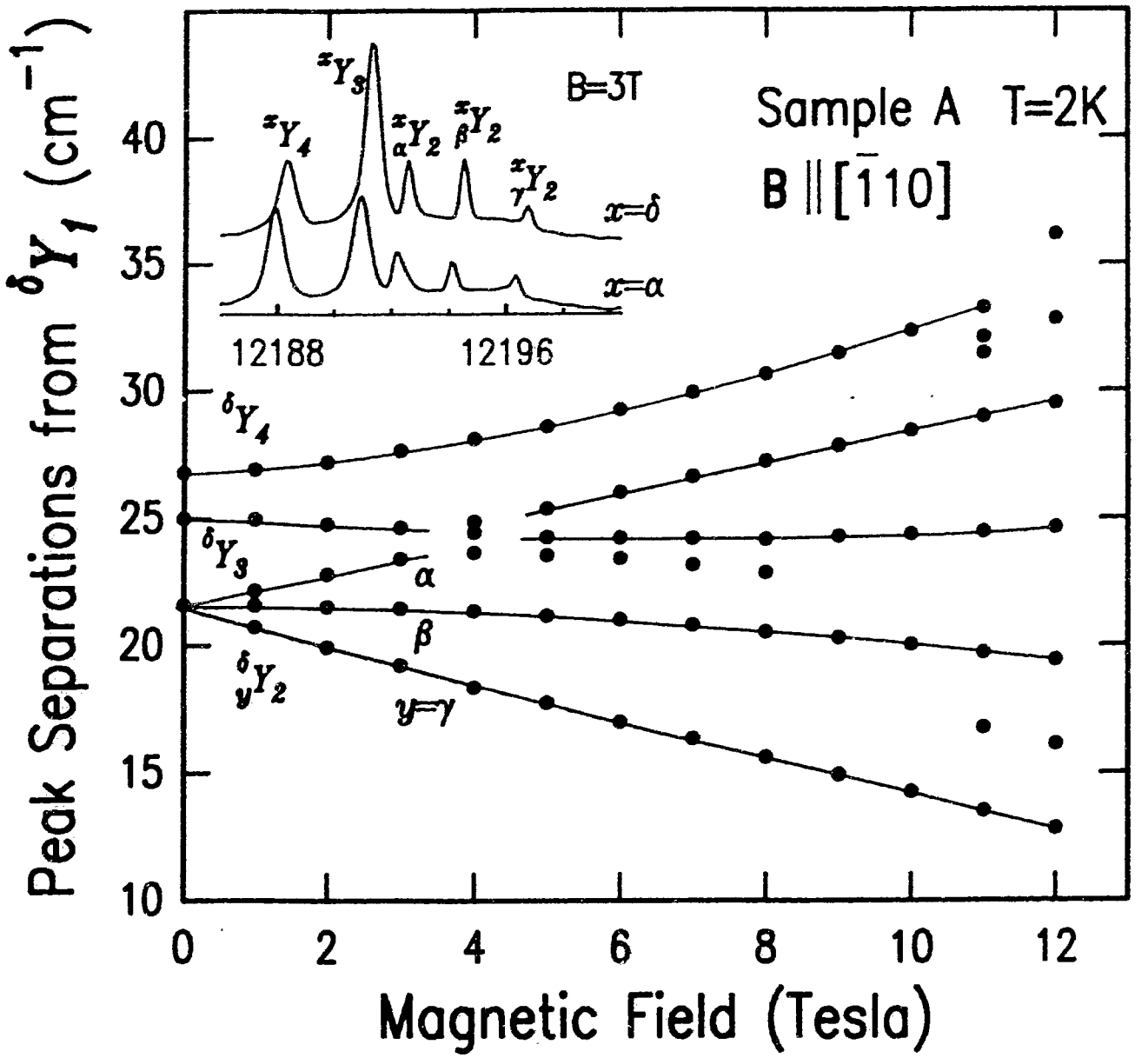

Figure 4.6

Zeeman splitting of the 1s two-hole replica in sample A for B ∥ [1̄10]. The peak positions relative to $^{\delta}Y_1$ measured in spectra such as those presented in Fig. 4.5, are reported for resonant excitation at $^{\delta}Y_1$. The data have been connected with lines to aid the eye. Similar Zeeman patterns are obtained by pumping other transitions of the Y_1-quadruplet as illustrated in the inset for excitation at $^{\delta}Y_1$ (top) and at $^{\alpha}Y_1$ (bottom). As plotted, the data constitutes a mapping of the BE final states.

function of magnetic field amounts to the mapping of the final states.

Fig. 4.5 shows the Y 1s replica obtained by resonantly exciting at the $^{\delta}Y_1$ transitions. The spectral energies of $^{\delta}Y_1$ for B ∥ [$\bar{1}$10] can be found in Table 4.1. The spectra are plotted with their energy scale relative to $^{\delta}Y_1$ in order to remove the strong shift. The same narrow bandpass filter used to obtain the spectra shown in Fig. 3.4 and 3.7 was also utilized here. The filter was tilt-tuned to higher energies but the 1s replicas fan out so that by 4 T, the bandwidth of the filter can no longer encompass all lines and $^{\delta}_{\gamma}Y_2$ is attenuated. Other spectra where the interference filter was tuned to even higher energy (not shown) were also collected and enabled the exact location of $^{\delta}_{\gamma}Y_2$ to be determined.

Until the "crossing" of $^{\delta}Y_3$ and $^{\delta}_{\alpha}Y_2$, an event occurring around 4 T, the splitting pattern of the Y 1s transitions is very simple. $^{\delta}Y_4$ and $^{\delta}Y_3$ are seen to shift away from each other while $^{\delta}Y_2$ splits into three components. In the course of their approaching trajectories, $^{\delta}Y_3$ and $^{\delta}_{\alpha}Y_2$ seem to anti-cross. In other words, the individual $^{\delta}Y_3$ and $^{\delta}_{\alpha}Y_2$ peaks do not come in contact but manage nevertheless to continue at higher field on a trajectory defined before approach. This behavior is evidenced in a clearer fashion in Fig. 4.6. The observation of an extra peak labelled "?" in the range 4 T to 8 T around $^{\delta}Y_3$ and $^{\delta}_{\alpha}Y_2$ remains mysterious.

The general pattern of the splitting is summarized in Fig. 4.6 by plotting replica-to-excitation separations versus magnetic field. The solid lines are there only to guide the eye. The displayed data includes the position of the peaks found in Fig. 4.5 as well as those at fields up to 12 T. As mentioned earlier, excitation in the other Y_1

split initial states (not shown) yielded similar results.

As inferred previously, the Zeeman pattern observed in Fig. 4.6 corresponds to that of the final states of the PL transitions. We use this information to confirm the defect orientation. In Fig. 3.12, we showed the possible splitting patterns for defect along the three main crystallographic directions as predicted by group theory. The pattern observed in Fig. 4.6 agrees only with scenarios [001]a and [110]a, further disproving the [111] scenario.

For the sake of completeness we also investigated the splitting of the Y 2s replicas under the influence of the magnetic field. Fig. 4.7 displays a sequence of spectra from sample A for increasing magnetic field applied parallel to $[\bar{1}10]$. The data shown is for resonant excitation at $^{\delta}Y_1$, except for the bottom spectrum which was obtained at 12 T by pumping $^{\alpha}Y_1$ instead. The spectra are shifted by an appropriate amount in order to align the $^{\delta}Y_1^{2s}$ transitions. The actual spectral energies of $^{\delta}Y_1^{2s}$ can be found in Table 4.1. The bottom spectrum was shifted by the same amount as the one directly above it.

Sample A exhibits a 0 T 2s replica spectrum very similar to that of sample B (Fig. 3.6) although superposed on a background of stronger $(D^0,A^0)/(e,A^0)$ bands as well as lacking the $(A_C^0,X)^{2s}$ transitions. In Fig. 3.6 (sample B), the 2s replicas of the (A_C^0,X) are clearly visible approximately 10 cm^{-1} below Y_1^{2s}. This is not the case for sample A at 0 T as seen in the top spectrum of Fig. 4.7. The series of spectra displayed in Fig. 4.7 reveals a Zeeman splitting of the 2s replicas that correlates well with that of their 1s counterparts. $^{\delta}Y_1^{2s}$ does not split while $^{\delta}Y_{3+4}^{2s}$ is seen to split in two parts, at least initially. At higher fields, an extra component seems to split off the high energy

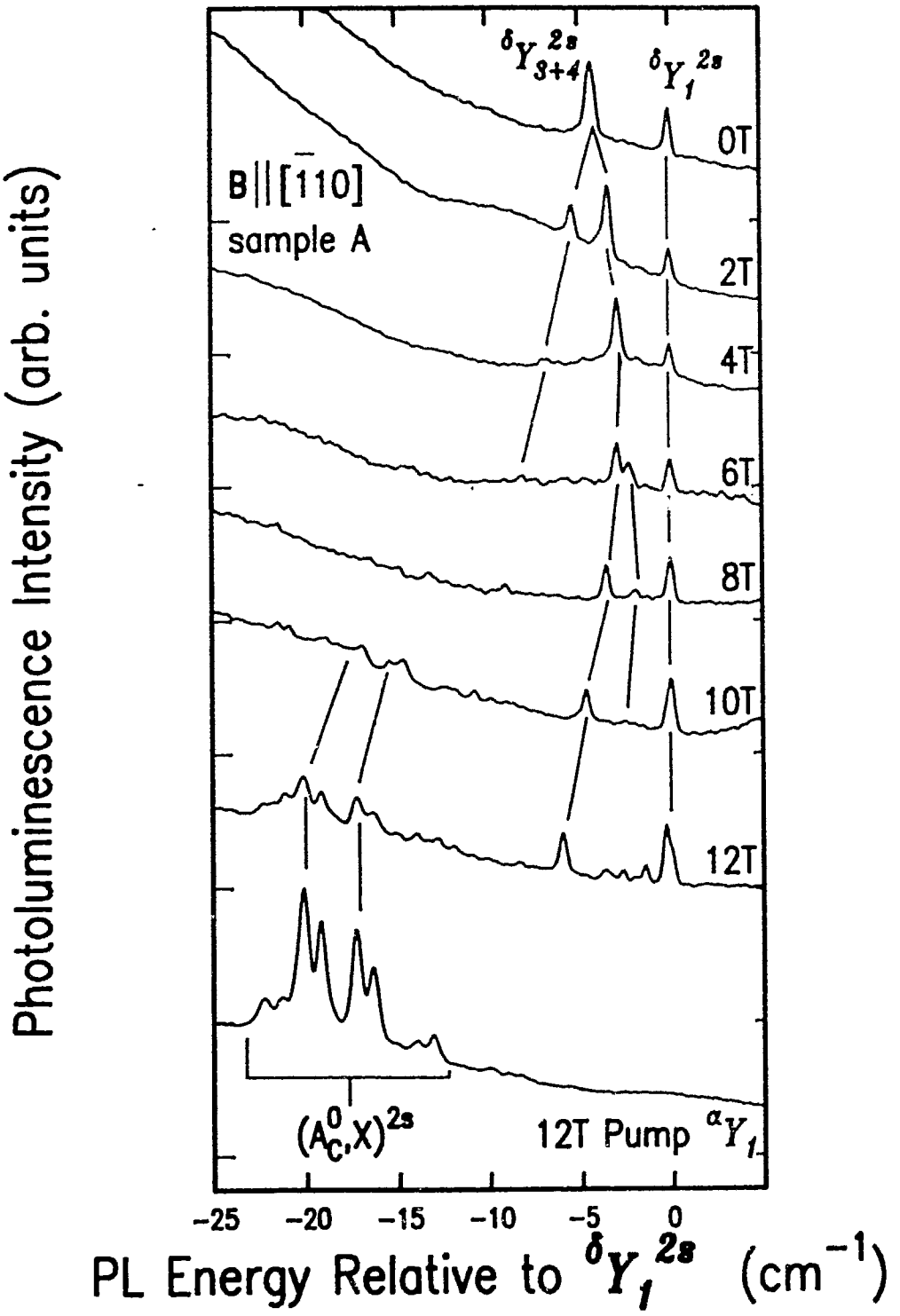

Figure 4.7

PL spectra resonantly excited at the $^{\delta}Y_1$ transitions for field going from 0 to 12 T in steps of 2 T and at $^{\alpha}Y_1$ for 12 T (bottom). The spectra are referenced to $^{\delta}Y_1$ or laser excitation. New features appearing at lower energy than the 2s two-hole transitions are attributed to $(A_C^0,X)^{2s}$ transitions. These lines are stronger when pumping $^{\alpha}Y_1$.

branch of $^{\delta}Y^{2s}_{3+4}$. Alternatively the behaviour of this extra line could be interpreted as the anti-crossing of one of the "invisible" 2s two-hole replica whose final state belong to the symmetric subset as discussed in section 3.3, with the high energy branch of $^{\delta}Y^{2s}_{3+4}$. The "symmetric" replica seems to increase in intensity as it approaches the high energy branch of $^{\delta}Y^{2s}_{3+4}$ and decrease again as it moves away from it in a fashion suggesting the presence of mixing of states.

As was the case for the 1s replicas, the 2s replicas excited via different split Y_1 transitions appear shifted with respect to each other by an amount equal to the difference in excitation energy. This confirms that, for low fields, no relaxation occurs in the initial states. We performed the same set of measurements as shown in Fig. 4.7 but for excitation set on $^{\alpha}Y_1$ (not shown) and observed similar but shifted 2s replicas. Fig. 4.8 is a plot of the separation of the 2s replica from $^{\alpha}Y^{2s}_1$ for excitation at $^{\alpha}Y_1$ (triangles) and from $^{\delta}Y^{2s}_1$ for excitation at $^{\delta}y$ (dots). As illustrated in this figure, the data for excitation on α and on δ agree very well if the peak positions are given with respect to the corresponding $^{x}Y^{2s}_1$ transitions. Extra splitting in the lower energy branch of Y^{2s}_{3+4} is visible for excitation into $^{\alpha}Y_1$. This extra splitting together with the one observed for the higher energy branch implies that Y^{2s}_{3+4} contains a minimum of four states at zero field. This is twice as many as in the 1s replicas (Y_3 and Y_4 being non-degenerate) suggesting the presence of at least two extra symmetric states in the 1s-2s manifold degenerate with Y^{2s}_3 and Y^{2s}_4 at 0 T that were not present in the 1s-1s manifold.

A striking feature observed in the sequence displayed in Fig. 4.7 is the sudden emergence at high fields of a group of lines at energies

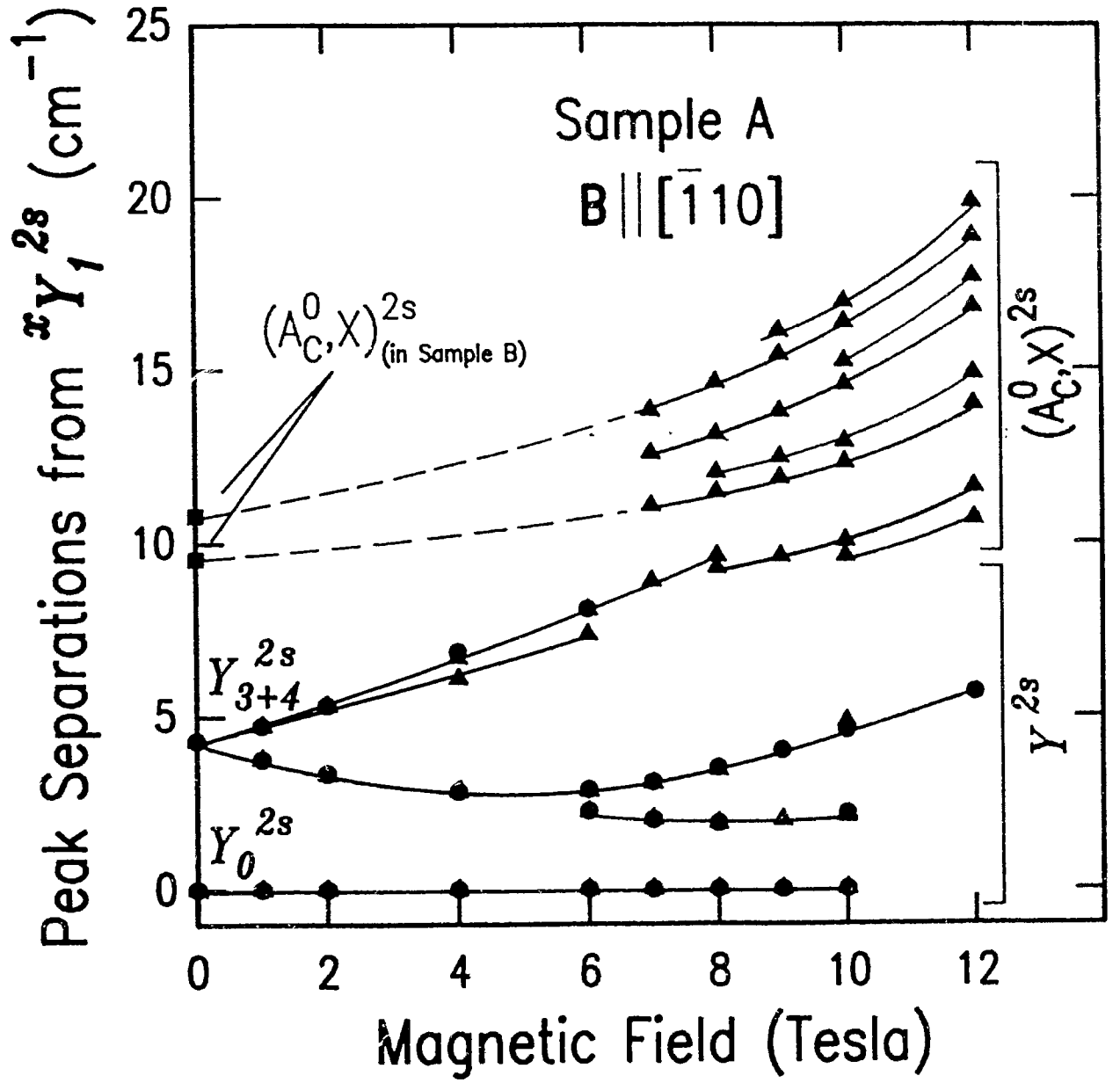

Figure 4.8

Zeeman splitting of the 2s two-hole replicas for B parallel to [$\bar{1}$10]. The peak positions relative to Y_1^{2s} are shown for resonant excitation of $^{\delta}Y_1$ (dots) and $^{\alpha}Y_1$ (triangles) in sample A. The behavior of the splitting is similar to that observed for the 1s manifold although more states are seen to split from Y_3^{2s} and Y_4^{2s}. These extra features are believed to be due to spin symmetric states. Lower energy peaks seen at high field are attributed to $(A_C^0,X)^{2s}$ signatures. Extrapolations (dashed lines) to lower field indeed correspond to zero-field position of the $(A_C^0,X)^{2s}$ transitions in sample B.

lower than the Y^{2s} set. This effect is even more pronounced for the spectra excited at ${}^{\alpha}Y_1$ (not shown except for 12 T); the new peaks are so strong in this case that by 12 T they completely dominate the PL. We note that these PL emissions, unlike the Y-related 2s replicas, do not shift when shifting the excitation energy. In the last two unshifted spectra of Fig. 4.7, the new lines are indeed aligned. These lines were attributed to 2s replicas of (A_C^0, X). We suggest that, as the field increase, some Zeeman split excited state of the principal (A_C^0, X) transition approaches the split Y_1 lines from the low energy side. At 12 T, resonant excitation at ${}^{\alpha}Y_1$ couples more efficiently to the acceptor BE and strong $(A_C^0, X)^{2s}$ replicas are observed. We further suggest that the $(A_C^0, X)^{2s}$ emission seen when pumping ${}^{\delta}Y_1$ is generated via relaxation in the initial BE state, ${}^{\delta}Y_1 \rightarrow {}^{\alpha}Y_1$. This type of high field relaxation was also observed in the 1s replicas. In Fig. 4.8, we have indicated where the $(A_C^0, X)^{2s}$ are located at 0 T by using data from sample B. An extrapolation of the $(A_C^0, X)^{2s}$ peaks at field leads to the zero field position of the $(A_C^0, X)^{2s}$.

Finally in this section we show a series of measurements that enables the detection of the four predicted $Y_1^{\bullet}$ split transitions. Fig. 4.9 displays a series of PL excitation (PLE) spectra of a special kind, constructed from a series of PL spectra (not shown) at 3.5 Tesla, for excitation going from 12215 cm^{-1} to 12227 cm^{-1} in steps of 0.2 cm^{-1}. In Fig. 4.9(a) we present a PL spectrum at the same field, but excited with above-gap light for reference. In (b), (c), (d), (e) and (f), the spectral intensity at fixed separation from the excitation energy is plotted as a function of excitation energy. The central portions (12220-12224 cm^{-1}) of the PLE spectra have been scaled by a factor of

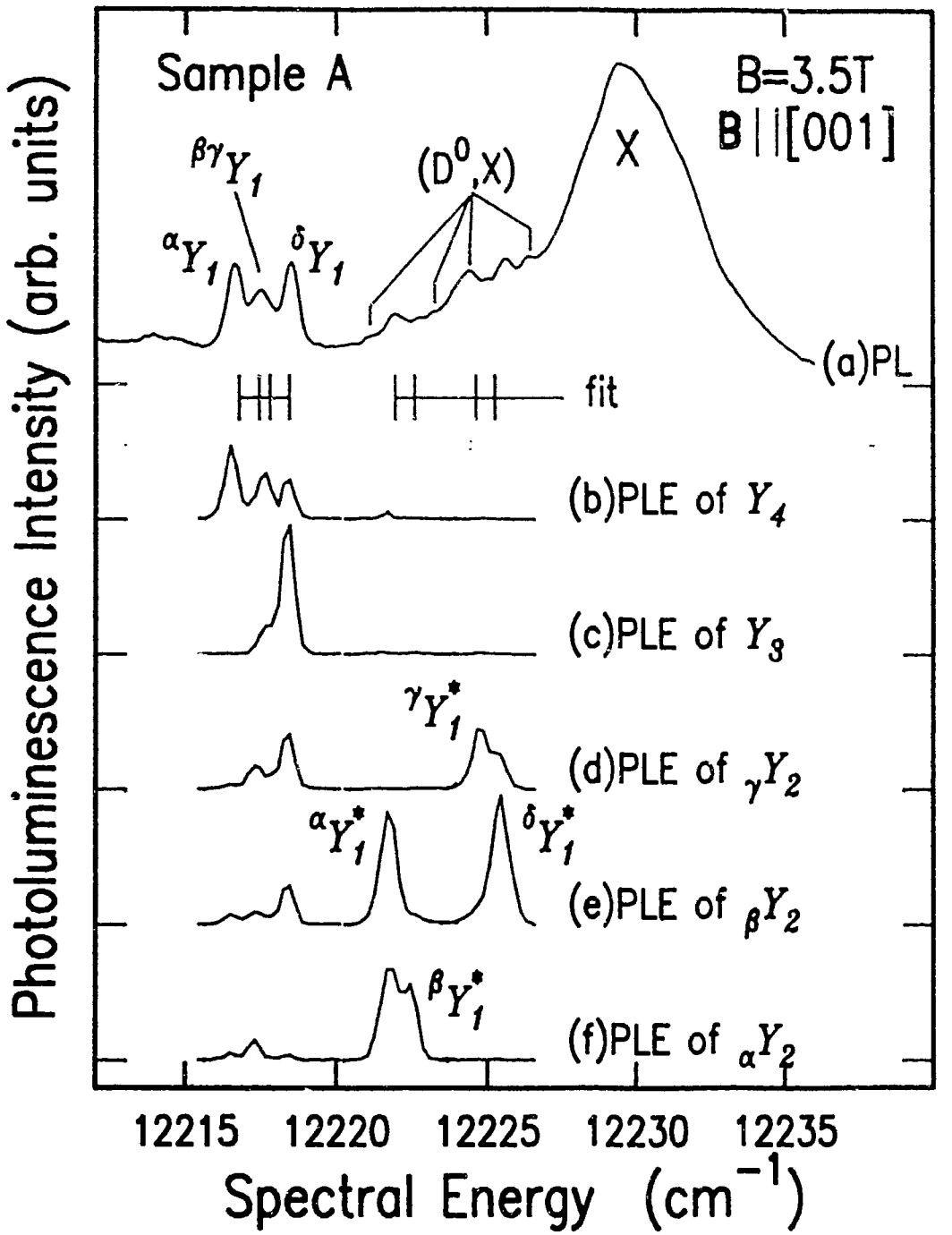

Figure 4.9

PL excitation spectra at 3.5 Tesla for (b) Y_4, (c) Y_3, (d) $_\gamma Y_2$, (e) $_\beta Y_2$ and (f) $_\alpha Y_2$ as compared to (a), a PL spectrum at the same field. The three bottom spectra reveal strong excitation channels for the Y_2 is replicas and enable a clear identification of the four split Y_1^* states. Predictions of the splitting of the Y_1 and Y_1^* quadruplets generated by the fit described in the text is shown between spectra (a) and (b).

2.5 for clarity.

These PLE spectra monitor more than one particular transition. For example in Fig. 4.9(d), ${}^{\beta}_{\gamma}Y_2$, ${}^{\delta}_{\gamma}Y_2$, ${}^{\gamma}_{\gamma}Y^*_2$ and ${}^{\delta}_{\gamma}Y^*_2$ are sequentially detected. In that sense, they are not ordinary PLE spectra, but constitute the best way to display the data, considering the fact that no relaxation occurs between the different initial states of the PL transitions at that field.

The correspondence between PLE and PL features in the Y_1 region is very clear. Intensities of the PLE features may vary but energies undoubtedly agree. On the other hand, as noted in Fig. 4.1 at this field, Y_1^* PL signatures are not very visible and most peaks seen in that region have been attributed to (D^0,X) transitions. Nevertheless, the agreement between the peaks visible in spectrum 4.9(d), (e), (f) and the tickmarks below spectrum 4.9(a) derived from the theoretical fit supports the four-component Y_1^* model. The Y_1^* split-states exhibit the same two doublets as for the Y_1 split-states, but further separated. The large separation into two pairs is attributed to the $m_j^{3h} = \pm 1/2$ coupled hole state splitting and the separation within each pair is again due to the electron splitting.

4.4 Summary

In this chapter the orientation of the Y-defect was determined. The observed anisotropies of the principal Y_1 BE transition, the magnitude of its Zeeman splitting as a function of field, as well as the splitting of Y_1^*, the other principal BE transition, were all

successfully accounted for by assuming a defect orientation along [110]. Other Zeeman results presented in this chapter served to confirm the model put forward by verifying the degeneracy of both Y_1^* and the neutral double acceptor levels.

With this knowledge on defect orientation, we can now finish the polarization calculations started in section 3.5. According to these theoretical predictions and the experimentally verified defect orientation, Y_1 is a σ-transition 100% polarized along $[\bar{1}10]$ and Y_1^* is a π-transition 60% polarized along [110]. Experimentally Y_1 was found to be 35% polarized along $[\bar{1}10]$ and Y_1^* 15% along [110]. Although not as strong as predicted, the observed polarization is in reasonable agreement with the theory. It is demonstrated in the appendix that the orthorhombicity of the defect causes a mixing of states that was not accounted for in our calculation of the polarization. This effect could explain the discrepancies between the predicted and observed values.

CHAPTER 5

SUMMARY AND DISCUSSION

5.1 Summary

In this work, we performed a detailed spectroscopic investigation of two PL lines, Y_1 and Y_1^*. This is the first observation of Y_1^*, whereas Y_1 had been reported in the literature but its origin was unknown. From the experimental results presented in chapters 3 and 4 we come to the following conclusions regarding Y_1 and Y_1^* and the center responsible for these PL emissions :

i) Y_1 and Y_1^* are *bound exciton transitions.*

The spectral energies and narrow FWHM of the Y_1 and Y_1^* PL transitions strongly suggest that these transitions are due to BE recombination transitions. Also, the measured lifetime of Y_1 lies in the range typical for BE. The strongest evidence for assigning Y_1 and Y_1^* to BE transitions, however, is the observation of a rich replica spectrum characteristic of acceptor bound excitons. The binding center for these BE transitions is referred to as the Y defect.

ii) The Y defect is *not an isoelectronic center.*

The observed *two-particle* replica (two-electron or two-hole) indicates that Y has electronic charges of its own. Y is therefore an acceptor or a donor but not an isoelectronic center.

iii) The Y defect is an *acceptor.*

Strong evidence showing that Y is an acceptor rather than a donor lies in the observed overall similarity between the two-hole spectrum of Y and that of the carbon acceptor BE, if we neglect the fine structure found within the 1s, 2s and 3s Y replica groups. The ionization energy of the neutral Y to its singly charged state is calculated from the two-hole spectrum to be $214 \pm 2\ cm^{-1}$ (26.5 ± 0.2 meV). This value is very close to the ionization energy of the carbon acceptor.

iv) The Y defect is a *double* acceptor.

In the absence of perturbations that are odd under time reversal, levels from system which have half integer total spin must have at least a two-fold degeneracy, the Kramers degeneracy [85Sb]. On the other hand, for systems with integer total spin, it is possible to have non-degenerate levels. We believe we have observed such non-degenerate states for the bare neutral state of Y (in its ground, second and third excited states), implying that it has an even number of charges and therefore cannot be a single acceptor. Furthermore, the structure found within the 1s, 2s and 3s neutral acceptor levels was explained by considering the $j \cdot j$ interaction between <u>two</u> $j=3/2$ holes in the local field of the defect. Therefore, Y is deduced to be a double acceptor.

v) The Y defect has *axial symmetry.*

The observed polarizations of Y_1 and Y_1^* in the absence of

external perturbations demonstrates that the symmetry of the initial and final states of the BE transitions is lower than that of the GaAs lattice. This implies that Y cannot be a single point defect. The structure of the 1s, 2s and 3s neutral acceptor levels requires the two-hole system (as mentioned in point iv) to exist in a reduced symmetry environment. According to group theory, reduction of symmetry along certain directions, i.e. axial symmetry, will produce the number of levels observed in the two-hole replica spectrum.

vi) The Y defect is *oriented along [110].*

The polarization of the lines Y_1 and Y_1^* suggests that the Y defects lies either along [110] or [$\bar{1}$10], although it does not eliminate the possibility of orientation along the <111> directions. We have presented a series of magnetic perturbation results and concluded that the anisotropies of the magnetic field split Y_1 quadruplet agrees with a defect orientation along [110]. Furthermore the simultaneous numerical fitting of these data with other Zeeman results confirmed this choice of orientation.

5.2 Discussion

Solely from the PL studies presented in this thesis, we come to a fairly precise picture of the defect responsible for the observed Y_1 and Y_1^* transitions. In Fig. 5.1 we present a schematic illustration of the Y defect in a GaAs sample. The crystallographic axes are indicated on

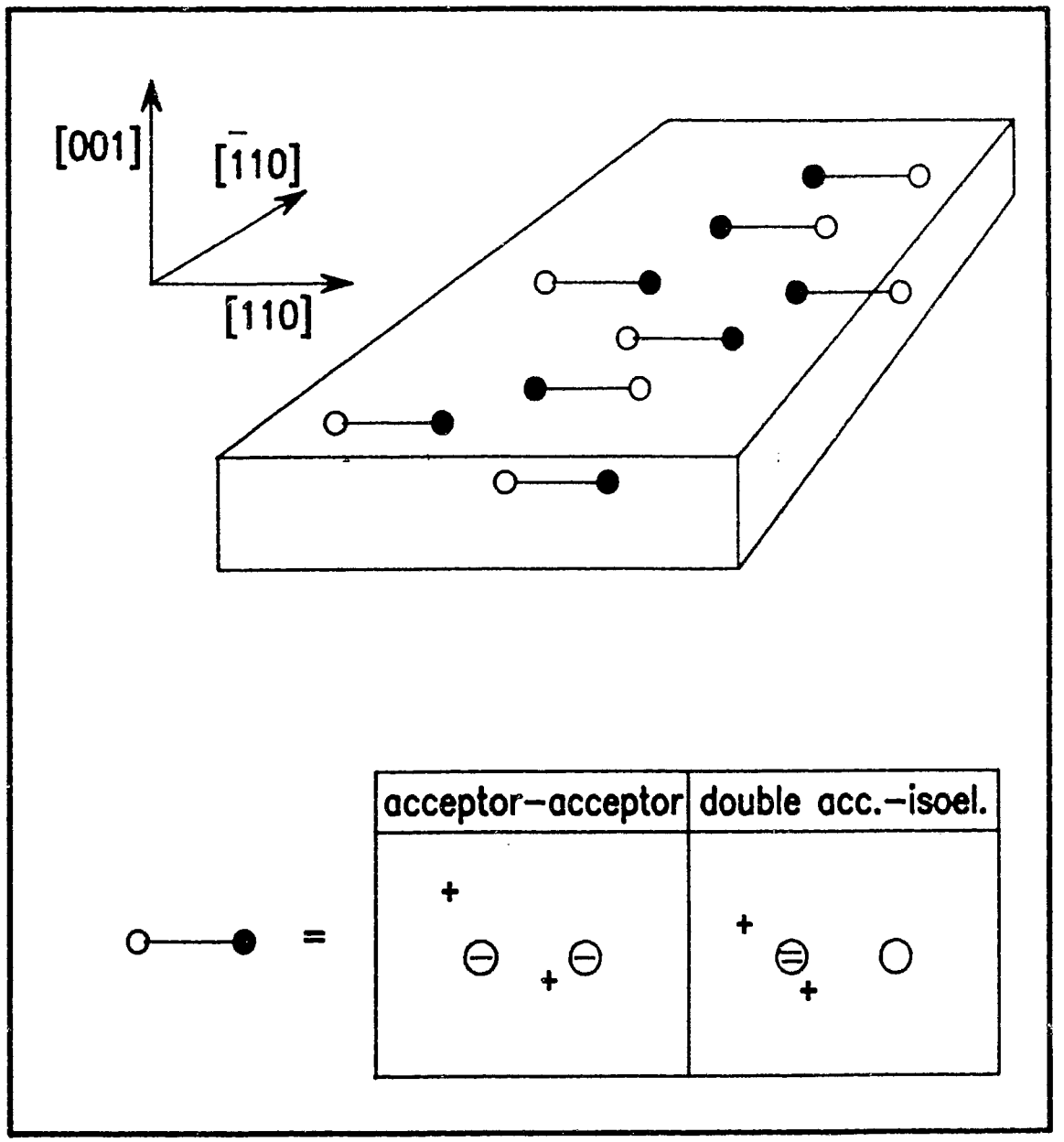

Figure 5.1

Schematic representation of Y defects in a GaAs epilayer. The possibly different components of the axial defect are represented by two spheres of different colors. The two possible models, namely a single acceptor/single acceptor pair and a double acceptor/isoelectronic center pair, are illustrated at the bottom of the picture.

the left of the figure. The individual defects are represented as a set of two point defects join together by a line. We used different colors for the two constituents because they need not be identical. The Y defect, being a double acceptor, could be composed of a single-acceptor-single-acceptor pair or a double-acceptor-isoelectronic pair.

At first sight, it seems difficult to understand why an axial defect like Y, would be incorporated along any particular direction in a crystal lattice. In an attempt to understand this phenomenon, we need to examine some aspects of MBE growth.

First, one must keep in mind that epitaxial growth is performed in a very anisotropic manner, one layer at a time onto the growth surface. Since arsenic is much more volatile than gallium, good quality epilayers are grown under an As overpressure. The gallium atoms impinging on the surface are characterized by a sticking coefficient near unity. Arsenic, on the other hand, is thought to be adsorbed and desorbed at rates determined by the temperature. It is therefore convenient to think of the growth surface as typically being terminated by As atoms (this situation is referred to as As stabilized) since Ga atoms get covered immediately after their arrival.

We also note that in the (001) plane, the two directions [110] and [$\bar{1}$10] are not equivalent. The dangling bonds of an As terminated (001) surface all lie in the (110) plane. This anisotropy manifests itself in the appearance of oriented (2 x 4) and C(2 x 8) reconstruction structures with the two-fold periodicity along [$\bar{1}$10] [76C]. These reconstructions have been studied with the aid of reflection high energy electron diffraction (RHEED) apparatus [76C,83N]. The inequivalence of

the two <110> directions has also been observed ... ...e formation of the so-called oval defects [82B] which are oriented along [$\bar{1}$10].

Studies of growth dynamics have revealed that the layer-by-layer growth of MBE actually proceeds by the spreading of randomly nucleated islands on the growth surface. By comparing the intensities of the various RHEED diffracted beams for incident beams along the two <110> directions, Neave and coworkers [83N] concluded that the step propagation was faster in the [$\bar{1}$10] direction than in [110]. It is therefore believed that the dimension of the steps normal to [110] are typically larger than those normal to [$\bar{1}$10]. Using this picture, we can now supply a speculative mechanism for the formation of the Y defect.

Suppose that the Y defect is composed of two constituents A and B, which may or may not be identical. We can imagine that the incorporation of one of the components, say A, perturbs the step in which it gets imbedded in such a way as to create an attractive potential for the incorporation of the second component, B. The relative abundance of steps normal to [110] and the fact that they grow at a slower pace than those normal to [$\bar{1}$10] may explain why the Y defect incorporates along the [110] direction. Given that the progression of the steps is slow enough the second component will have time to sample an area around the imbedded component and find the closest distance of approach directly along the step normal, this presumably being the position of lowest energy. According to this speculative model, the defect need not be strictly along [110]. Instead we expect a certain distribution around that direction. From our data, we note that this distribution must not be too extended since it is still possible to observe sharp lines in the presence of a magnetic field.

We suggested that some time interval is needed for the second species to detect the presence of the first. High growth rates should therefore decrease the defect concentration, as pairing may not have time to occur. This hypothesis is supported by the work of Szafranek *et al* [90Sb]. These authors studied the influence of the growth temperature, the As/Ga flux ratio and the growth rate on the incorporation of the so-called A acceptor. They also clearly established a correlation between the A acceptor and Y_1 (which they called P_0) as well as with the g-line. According to their investigation, the incorporation of these defects, including Y_1, increases monotonically with the As/Ga flux ratio for constant As pressure. In practice, they were able to grow GaAs layers with low concentration of defects by increasing the Ga flux and therefore also increasing the growth rate to ~ 5μm per hour. No clear trend of defect concentration with growth temperature could be established. These results are in agreement with the proposed binary growth mechanism for Y.

To conclude this discussion we would like to address the question of the chemical identity of the Y defect. Determining the exact chemical nature of the Y constituents using the photoluminescence method alone is a very difficult task. PL is a defect-specific analysis method in the sense that each defect will generally have a distinct PL signature. The assignment of an observed PL feature to a specific defect, however, may be extremely arduous. This identification is complicated by the lack of theoretical predictions of spectral positions, even for known defect configurations, and by the vast number of possible defects. The energy of a complex is dependent on the exact

arrangement of the atoms forming the defect in the lattice as well as the way in which the lattice is perturbed by the presence of the defect. The determination of the chemical nature of the centers responsible for the KP-lines has been plagued by similar problems. Despite the intense research activity on these lines, the chemical nature of the series remains a matter of speculation [88S, 90C].

One way of determining the chemical nature of PL peaks of unknown origin is to use intentional doping experiments in which the intensity of the PL feature is correlated with intentionally incorporated elemental impurities in an otherwise pure sample. This method can only work if the investigated defect is indeed composed of foreign atoms and not native defects. In the case of the Y defect, the intentional doping would have to be carried out during the growth of the sample since these defects are known to form during growth.

To complicate things, the incorporation of only one impurity may not be sufficient to increase the defect concentration; several components may be needed. On the other hand, the incorporation of a species different from the constituents may act as a catalyst for defect formation and be mistaken as a constituent. One type of intentional doping experiment that is a conclusive characterization method relies on the observation of isotope effects. After observing the enhancement of a PL feature from the addition of a certain species, one incorporates an isotope of that element and looks for energy shifts in the generated PL features. These shifts are due to differences in the way the crystal structure rearranges itself around different impurity isotopes. The observation of such an effect is definite proof that the added element is a constituent of the defect studied. It would in principle be

possible to apply these methods to the study of the Y defect. Undertaking such a task, however, is beyond the scope of this work.

APPENDIX

DERIVATION OF THE HOLE SPIN HAMILTONIAN

The objective of this appendix is to carry out the derivation of the j = 3/2 hole spin Hamiltonian used in section 4.3. In doing so, we will calculate a number of relations such as equations 4.4 and 4.5 which were used without justification in chapter 4. Reference 70A is the primary source used throughout this appendix.

In general, the hole hamiltonian is written in the convenient form:

$$\mathcal{H} = \mu_B(\mathbf{H}\cdot\mathbf{g}\cdot\mathbf{S}) + \sum A_{i,\alpha}\, S^i_\alpha \qquad (A.1),$$

where $\mu_B(\mathbf{H}\cdot\mathbf{g}\cdot\mathbf{S})$ is the Zeeman term introduced earlier in equation 4.1, S^i_α are the spin projection operators and $A_{i,\alpha}$ are the coefficients associated with these operators. The index i represent the degree of the spin operator while α refers to the different projections along the x,y and z axes. It is convenient to rearrange the second term of the right hand side of A.1 in groups of spin operators such that each group has a definite symmetry:

$$\sum A_{i,\alpha}\, S^i_\alpha = \sum B_{k,q}\, O_{k,q} \qquad (A.2),$$

where $O_{k,q}$ are the new spin operators and $B_{k,q}$ are the new coefficients associated with them. k is the degree of the operators and q is a label used to differentiate between the terms of degree k. The use of operators in this form allows us to restrict the number of terms in the sum A.2. Operators of degree higher than 2 × S, here 3, can be omitted since they have zero matrix elements. Also, spin operators of odd degree are excluded because they are not invariant under time reversal.

Therefore, for S = 3/2, only terms of second degree need to be considered. Using tabulated values for $O_{2,0}$ and $O_{2,2}$ [70A], we get

$$\sum B_{k,q} O_{k,q} = D \{S_z^2 - \frac{1}{3} S(S+1)\} + E (S_x^2 - S_y^2) \qquad (A.3),$$

where D and E were used as coefficients instead of $B_{2,0}$ and $B_{2,2}$. Using the relations

$$S_+ = S_x + iS_y \quad \text{and} \quad S_- = S_x - iS_y,$$

we can rewrite A.3 as

$$\sum B_{k,q} O_{k,q} = D \{S_z^2 - \frac{1}{3} S(S+1)\} + \frac{1}{2} E (S_+^2 + S_-^2) \qquad (A.4).$$

In the reference system determined by the defect, the operator $\{S_z^2 - \frac{1}{3} S(S+1)\}$ is diagonal while $(S_+^2 + S_-^2)$ has only off diagonal elements. For a defect with axial symmetry, the coefficient E is equal to zero. Deviations from this simplest case (perfect axiality) are referred to as *orthorhombicity*.

In the absence of a magnetic field, using A.4 reduces the Hamiltonian A.1 to

$$\mathcal{H} = \begin{bmatrix} D & 0 & \sqrt{3}E & 0 \\ 0 & -D & 0 & \sqrt{3}E \\ \sqrt{3}E & 0 & -D & 0 \\ 0 & \sqrt{3}E & 0 & D \end{bmatrix} \qquad \begin{matrix} \text{basis} \\ \begin{bmatrix} 3/2 \\ 1/2 \\ -1/2 \\ -3/2 \end{bmatrix} \end{matrix} \qquad (A.4)$$

in the basis of the projection of the angular momentum on the z axis as indicated. The eigenvectors and eigenvalues of the Hamiltonian are:

eigenvectors	eigenvalues	
$\left\|\tilde{\pm}\frac{3}{2}\right\rangle = \cos\alpha \left\|\pm\frac{3}{2}\right\rangle + \sin\alpha \left\|\mp\frac{1}{2}\right\rangle$	$\sqrt{D^2+3E^2}$	(A.5a)
$\left\|\tilde{\pm}\frac{1}{2}\right\rangle = \cos\alpha \left\|\mp\frac{1}{2}\right\rangle - \sin\alpha \left\|\pm\frac{3}{2}\right\rangle$	$-\sqrt{D^2+3E^2}$	(A.5b),

where $\tan 2\alpha = \sqrt{3}E/D$. From A.5a and A.5b, we see that the role of the orthorhombicity ($E \neq 0$) is to mix states of different angular momentum as the ratio E/D increases. When the ratio E/D approaches zero, the defect is nearly axial, α approaches zero and the eigenstates of A.4 are also eigenstates of J_z. From results A.5 we also see that in zero field, the separation between the two $\left|\tilde{\pm}\frac{1}{2}\right\rangle$ and $\left|\tilde{\pm}\frac{3}{2}\right\rangle$ levels is simply $2(D^2+3E^2)^{1/2}$.

When an external magnetic field is applied along the z axis for example, the Hamiltonian A.1 can be written as

$$\mathcal{H} = \begin{bmatrix} D+\frac{3}{2}G & 0 & \sqrt{3}E & 0 \\ 0 & -D+\frac{1}{2}G & 0 & \sqrt{3}E \\ \sqrt{3}E & 0 & -D-\frac{1}{2}G & 0 \\ 0 & \sqrt{3}E & 0 & D-\frac{3}{2}G \end{bmatrix} \quad \begin{matrix} \text{basis} \\ \begin{bmatrix} 3/2 \\ 1/2 \\ -1/2 \\ -3/2 \end{bmatrix} \end{matrix} \qquad (A.6),$$

where $G = \mu_B g_z H$. Hamiltonian A.6 can be solved analytically. In this work, however, the eigenvalues used in Figs. 4.2, 4.4 and 4.9 were obtained numerically by diagonalizing energy matrices similar to A.6 after replacing for all adjustable and non-adjustable parameters. This allowed the determination of the eigenvalues for arbitrary field strength and orientation.

REFERENCES

55K W. Kohn and J.M. Luttinger, Phys. Rev. **98**, 915 (1955).

58L M. Lampert, Phys. Rev. Lett. **1**, 450 (1958).

59T Y. Toyozawa, Prog. Theor. Phys. Suppl. **12**, 111 (1959).

60H J.R. Haynes, Phys. Rev. Lett. **4**, 361 (1960).

62R E.I. Rashba and G.E. Gurgenishvili, Sov. Phys. Solid State **4**, 759 (1962).

63H J.J. Hopfield, D.G. Thomas and M. Gershenzon, Phys. Rev. Lett. 10, 162 (1963).

64H J.J. Hopfield, Proc. Intern. Conf. Phys. Semicond., Paris 1964 (Dunod, Paris 1964) p.725.

66N D.F. Nelson, J.D. Cuthbert, P.J. Dean and D.G. Thomas, Phys. Rev. Lett. **17**, 1262 (1966).

67B R.B. Bhargava and M.I. Nathan, Phys. Rev. **161**, 695 (1967).

68S L.I. Schiff, *Quantum Mechanics* (McGraw Hill, New York, 1968) p.397.

69Sa G.E. Stillman, C.M. Wolfe and J.O. Dimmock, Solid State Commun. 7, 921 (1969).

69Sb J. Shah, R.C.C. Leite and R.E. Nahory, Phys. Rev. **184**, 811 (1969).

70A A. Abragam and B. Bleaney, *Electron Paramagnetic resonance of transition ions* (Clarendon, Oxford, 1970), pp 139-156.

71L R.C.C. Leite and A.E. DiGiovanni, Appl. Phys. Lett. **40**, 169 (1967).

71Sa G.E. Stillman, D.M. Larsen, C.M. Wolfe, R.C. Brandt, Solid State Commun. **9**, 2245 (1971).

71Sb T. Skettrup, M. Suffczynski and W. Gorzkowski, Phys. Rev. B **4**, 512 (1971).

72B R.J. Bell, *Introductory Fourier Transform Spectroscopy,* (Academic Press, New York, 1972).

72R S. Rodriguez, P. Fisher and F. Barra, Phys. Rev. B **5**, 2219 (1972).

72S D.D. Sell, Phys. Rev. B **6**, 3750 (1972).

72Wa A.M. White, P.J. Dean, L.L. Taylor, R.C. Clarke, D.J. Ashen and J.B. Mullin, J. Phys. C **5**, 1727 (1672).

72Wb A.M. White, I. Hinchliffe, P.J. Dean and P.D. Greene, Solid State Commun. **10**, 497 (1972).

73B A. Baldereschi, N.O. Lipari, Phys. Rev. B **8**, 2697 (1973).

73C C. Cohen-Tannoudji, B. Diu and F. Laloë, *Mécanique Quantique*, vol 2, (Hermann, Paris, 1973), p. 1015.

73H U. Heim and P. Wiesner, Phys. Rev. Lett. **30**, 1205 (1973).

73K E. Kartheuser and S. Rodriguez, Phys. Rev. B **8**, 1556 (1973).

73M A.G. Miles, in *Deep Impurities in Semiconductors* (Wiley, New York, 1973), p. 16.

73W A.M. White, P.J. Dean, D.J. Ashen, J.B. Mullin, M. Webb, B. Day and P.D. Greene, J. Phys. C **6**, L243 (1973).

74H U. Heim and P.Hiesinger, Phys. Stat. Sol. (b) **66**, 461 (1974).

74M T.N. Morgan, in *Proceedings of the Twelfth International Conference on the Physics of Semiconductors,* edited by M.H. Pilkuhn (Teubner, Stuttgart, 1974), p. 391.

74W A.M. White, P.J. Dean and B. Day, J. Phys. C **7**, 1400 (1974).

75A P.J. Ashen, P.J. Dean, D.T.J. Hurle, J.B. Mullin and A.M. White, J. Phys. Chem. Solids **36**, 1041 (1975).

75B F. Bassani and Pastori Parravicini, *Electronic States and Optical Transitions in Solids* (Pergamon, Oxford, 1975).

75R E.I. Rashba, Sov. Phys. Semicond. **8**, 807 (1974).

75S M. Schmidt, T.N. Morgan and W. Schairer, Phys. Rev. B **11**, 5002 (1975).

75W P. Wiesner and U. Heim, Phys. Rev. B **11**, 3071 (1975).

75Y A. Yariv, *Quantum Electronics*, (Wiley, New York, 1975), p. 256.

76C A.Y Cho, J. Appl. Phys. **47**, 2841 (1976).

76H R.E. Honig, *Surface and thin film analysis of semiconductor materials,* in *Thin Solid Films* **31**, 89-122 (1976).

76S W. Schairer, D. Bimberg, W. Kottler, K. Cho and M. Schmidt, Phys Rev. B **13**, 3452 (1976).

78L N.O. Lipari and A. Baldereschi, Solid State Commun. **25**, 665 (1978).

78N R.A. Noack, W. Rühle and T.N. Morgan, Phys. Rev. B **18**, 6944 (1978).

79A T.R. AuCoin, R.L. Ross, M.J. Wade and R.O. Savage, Solid State Technol., 57 (1979).

79D P.J. Dean and D.C. Herbert, in *Topics in Current Physics* **14**, edited by K. Cho (Springer, Berlin 1979).

79J N.M. Johnson, D.J. Bartelink, R.B. Gold and J.F. Gibbons, J. Appl. Phys. **50**, 5034 (1979).

79O G.C. Osbourn and D.L Smith, Phys. Rev. B **20**, 1556 (1979).

79T D.C. Tsui and R.A. Logan, Appl. Phys. Lett. **35**, 99 (1979).

80K H. Künzel and K. Ploog, Appl. Phys. Lett. **37**, 416 (1980).

80R D.C. Reynolds, C.W. Litton, R.J. Almassy, G.L. McCoy and S.B. Nam, J. Appl. Phys. **51**, 4842 (1980).

81L M. Lannoo and J. Bourgoin, *Point Defects in Semiconductors I, Theoretical Aspects*, Springer Series in Solid State Sciences, Vol. 35 (Springer, Berlin, 1981).]

81R A.K. Ramdas and S. Rodriguez, Reports on Progress in Physics **44**, 1297 (1981).

82Da C.C. Dean and M. Pepper, J. Phys. c **15**, L1287 (1982).

82Db W. Demtröder, *Laser Spectroscopy* (Springer, Berlin, 1982), p.16.

82B M. Bafleur, A. Munoz-Yague and A. Rocher, J. Cryst. Growth **59**, 531 (1982).

82L See *Landolt-Börnstein, Numerical Data and Functional Relationships in Science and Technology, New Series*, Vol. 17, edited by O. Madelung, M. Schultz and H. Weiss (Springer, Berlin 1982), p. 228.

83C J.P. Contour, G. Neu, M. Leroux, C Chaix, B. Levesque and P. Etienne, J. Vac. Sci. Technol. B **1**, 811 (1983).

83K D.W. Kisker, H. Tews and W. Rehm, J. Appl. Phys. **54**, 1332 (1983).

83N J.H. Neave, B.A. Joyce, P.J. Dobson and N. Norton, Appl. Phys. A **31**, 1 (1983).

84M H. Mathieu, J. Camassel and F. Ben Chekroun, Phys. Rev. B **29**, 3438 (1984).

85C A.Y. Cho, in *The Technology and Physics of Molecular Beam Epitaxy*, edited by E.H.C. Parker, (Plenum Press, New York, 1985), p.1. (and references therein)

85D G.J. Davies and D. Williams, in *The Technology and Physics of Molecular Beam Epitaxy*, edited by E.H.C. Parker, (Plenum Press, New York, 1985), p.15.

85R D.C. Renolds, K.K. Bajaj and C.W. Litton, Phys. Rev. B 32, 8242 (1985).

85Sa M.S. Skolnick, T.D. Harris, C.W. Tu, T.M. Brennan and M.D. Sturge, Appl. Phys. Lett. **46**, 427 (1985).

85Sb J.J. Sakurai, *Modern Quantum Mechanics* (Benjamin Cummings, Menlo Park, 1985), p.281.

86Sa T. Steiner, M.L.W. Thewalt, E.S. Koteles and J.P. Salerno, Phys. Rev. B **34**, 1006 (1986).

86Sb T. Steiner, Ph.D. Thesis, January 1986.

87Sa M. Shur, *GaAs Devices and Circuits,* (Plenum Press, New York, 1987), p.105.

87Sb P.E. Simmonds and R Sooryakumar, Phys. Stat. Sol. (b) **142**, K137 (1987).

88B J.C. Bourgoin, H.J. von Bardeleben and D. Stiévenard, J. Appl. Phys. **64**, R65 (1988).

88Ca S. Charbonneau, W.G. McMullan and M.L.W. Thewalt, Phys. Rev. B 38, 3587 (1988).

88Cb S. Charbonneau, Ph.D. Thesis, September 1988.

88K M. Kaminska, Revue Phys. Appl. **23**, 793 (1988).

88S M.S. Skolnick, D.P. Halliday and C.W. Tu, Phys. Rev. B **38**, 4165 (1988).

89S B.J. Skromme, R. Bhat, H.M. Cox and E. Colas, IEEE Jour. Quant. Elec. **25**, 1035 (1989).

90B D.J.S. Beckett, Ph.D. Thesis, December 1990.

90C S. Charbonneau and M.L.W. Thewalt, Phys. Rev. B **41**, 8221 (1990).

90L A. Lorke, J.P. Kotthaus and K. Ploog, Phys. Rev. Lett. **64**, 2559 (1990).

90Sa M. Said and M.A. Kanehisa, Phys. Stat. Sol. (b) **157**, 311 (1990).

90Sb I. Szafranek, M.A. Plano, M.J. McCollum, S.A. Stockman, S.L. Jackson, K.Y. Cheng, and G.E. Stillman, J. Apply. Phys. **68**, 741 (1990).

90Sc T. Steiner, Yu Zhang and M.L.W. Thewalt, Appl. Phys. Lett. **40**, 169 (1990).

90T M.L.W. Thewalt, M.K. Nissen, D.J.S. Beckett and K.R. Lundgren, Mat. Res. Symp. Proc. **163**, 221 (1990).

90Z S. Zemon and G Lambert, Mat. Res. Soc. Symp. Proc. **163**, 109 (1990).

91B D.J.S. Beckett, A. Villemaire, M.K. Nissen and M.L.W. Thewalt, to be published.